Université catholique de Louvain

Institute of Condensed Matter and Nanosciences

Bio- and Soft Matter (UCL/IMCN/BSMA)

Nanoimprinted Ferroelectric Polymer Layers for Organic Memory Devices and Multiferroism

Ronggang Cai

Thesis presented in partial fulfillment of the degree of

Doctor in Materials Science Engineering

Jury members:

Prof. Jacques Devaux (UCL, BE), president

Prof. Alain M. Jonas (UCL, BE), supervisor

Prof. Bernard Nysten (UCL, BE), member

Prof. Luc Piraux (UCL, BE), member

Prof. Yves Geerts (ULB, BE), member

Dr. Albert van Breemen (Holst Centre, NL), member

Louvain-la-Neuve, September 2016

Acknowledgements

I must, first and foremost, express my thanks to Prof. Alain Jonas for providing me the opportunities to perform my master and Phd researches in his group and for giving me the freedom to pursue my ideas and research interests. This Phd thesis would not have been possible without his continuous guidance, advice and encouragement. In addition, the enthusiasm he has for the research and the optimistic attitude have always been a great inspiration for me. I also got a lot of supports from him for my private life. I will never forget his understanding and supports whenever I had any urgent personal issues, a lot to name. Dear Alain, working with you for more than 6 years would be precious treasure in my life and thank you for everthing during these years. It is my great pleasure to continue to work with you after finishing this thesis.

I would like to thank Prof. Bernard Nysten for his help with PFM and other AFM-based measurements. Everytime when I went to his office and said “I have a problem with PFM.”, he was always kind and tried to find a solution with me. I want to thank Prof. Luc Piraux, Prof. Gerwin Gelinck, Dr. Albert van Breemen, Prof. Yves Geerts, and Prof. Zhijun Hu for providing supports at different stages of this thesis. I also want to thank all the jury members for your invaluable comments and suggestions on improving the quality of this thesis

It is really a great pleasure to work with my (ex-)colleagues in the lab. They were always there to provide help whenever I met any problems on technical, administrative, and even private issues. Their scientific and non-scientific supports, suggestions, and comments are great contributions to the success of my Phd thesis. I also want to express my sincere thanks to winfab (ex-)staffs. Without their help, my devices would not have been ready. Since there have been so many nice people on my way during my Phd study in UCL, I will not take the risk to list all the names, in order not to miss anyone.

我要感谢所有在新鲁汶认识的中国小伙伴们，在单调的科研实验之余，我们一起玩，聚聚餐聊聊天打打牌，来充实在异国他乡的枯燥生活。虽然大部分人已经离开新鲁汶，但时不时回想起来，脑袋里还是满满快乐的回忆。不论大家身居何地，身在何职，祝愿所有人一切顺利，想啥来啥。

最后，我要特别感谢我的家人。我的父母，我总是能从你们那得到精神上的支持。我的老婆，我们从出国开始就互相扶持互相帮助，有了你，我们的国外生活学习才如此的丰富多彩。我的女儿，你是上天给爸爸妈妈最好的礼物，想想你都是莫大的满足感，希望你健康快乐的成长，爸爸妈妈永远爱你。

Scientific Output

1. **Cai, R.**, Antohe, V. A., Piraux, L., Nysten, B., Jonas, A. M., " Room temperature magnetic control of ferroelectric polarization in a nanopatterned organic multiferroic layer," manuscript submitted.

2. **Cai, R.**, Jonas, A. M., "Local Maps of the Polarization and Depolarization in Organic Ferroelectric Field-Effect Transistors," Sci. Rep., 6, 22116 (2016).

3. **Cai, R.**, Kassa, H. G., Haouari, R., Marrani, A., Geerts, Y. H., Ruzie, C., van Breemen, A. J. J. M., Gelinck, G. H., Nysten, B., Hu, Z., Jonas, A. M., "Organic ferroelectric/semiconducting nanowire hybrid layer for memory storage," Nanoscale, 8, 5968-5976 (2016). (**2016 Hot Article in Nanoscale**)

4. **Cai, R.**, Kassa, H. G., Marrani, A., van Breemen, A. J. J. M., Gelinck, G. H., Nysten, B., Hu, Z., Jonas, A. M., "Field-effect memory transistors based on arrays of nanowires of a ferroelectric polymer", Proc. SPIE 9569, Printed Memory and Circuits, 95690G (2015). (**Best paper award**)

5. **Cai, R.**, Kassa, H. G., Marrani, A., van Breemen, A. J. J. M., Gelinck, G. H., Nysten, B., Hu, Z., Jonas, A. M., "An organic ferroelectric field effect transistor with poly(vinylidene fluoride-co-trifluoroethylene) nanostripes as gate dielectric," Appl. Phys. Lett., 105, 113113 (2014).

6. Nougaret, L., Kassa, H. G., **Cai, R.**, Patois, T., Nysten, B., van Breemen, A. J. J. M., Gelinck, G. H., de Leeuw, D. M., Marrani, A., Hu, Z., Jonas, A. M., "Nanoscale Design of Multifunctional Organic Layers for Low-Power High-Density Memory Devices," ACS Nano, 8, 3498-3505 (2014).

7. Kassa, H. G., Nougaret, L., **Cai, R.**, Marrani, A., Nysten, B., Hu, Z., Jonas, A. M., "The Ferro- to Paraelectric Curie Transition of a Strongly Confined Ferroelectric Polymer," Macromolecules, 47, 4711-4717 (2014).

8. Kassa, H. G., **Cai, R.**, Marrani, A., Nysten, B., Hu, Z., Jonas, A. M., "Structure and Ferroelectric Properties of Nanoimprinted Poly(vinylidene fluoride-ran-trifluoroethylene)," Macromolecules, 46, 8569-8579 (2013).

9. van Breemen, A. J. J. M., van der Putten, J. B. P. H., **Cai, R.**, Reimann, K., Marsman, A. W., Willard, N., de Leeuw, D. M., Gelinck, G. H., "Photocrosslinking of ferroelectric polymers and its application in three-dimensional memory arrays," Appl. Phys. Lett., 98, 183302 (2011).

Table of Contents

List of Abbreviations and Symbols

RFID	Radio-frequency identification
P(VDF-TrFE)	Poly(vinylidene fluoride-co-trifluoroethylene)
PVDF	Poly(vinylidene fluoride)
PTAA	Poly(triarylamine)
P3HT	Poly(3-hexylthiophene-2,5-diyl)
C8-BTBT	2,7-dioctyl[1]benzothieno[1]benzothiophene
BBL	Poly(benzimidazobenzophenanthroline)
PEDOT:PSS	Poly(3,4-ethylenedioxythiophene):poly(styrene sulfonic acid)
Ppy:PSS	Polypyrrole-poly(styrene sulfonic acid)
Si	Silicon
SiO_2	Silicon dioxide
$BaTiO_3$	Barium titanate
PZT	Lead zirconate titanate
SPM	Scanning probe microscopy
STM	Scanning tunneling microscopy
AFM	Atomic force microscopy
PFM	Piezoresponse force microscopy
MFM	Magnetic force microscopy
KPFM	Kelvin probe force microscopy
FeFET	Ferroelectric field-effect transistor
MSF	Metal-semiconductor-ferroelectric junction
DSC	Differential scanning calorimetry
NIL	Nanoimprint lithography
LED	Light emitting diode

NLS	Nucleation-limited-switching
KAI	Kolmogorov-Avrami-Ishibashi
HOMO	Highest occupied orbital
LUMO	Lowest unoccupied orbital
LB	Langmuir–Blodgett
OSC	Organic semiconductor
S/D/G	Source/Drain/Gate
ME	Magnetoelectric
Au	Gold
Cr	Chromium
Ni	Nickel
Ag	Silver
Pt	Platinum
Ir	Iridium
Co	Cobalt
Fe	Iron
$\boldsymbol{D}$	Displacement
$\boldsymbol{P}$ **or** $\boldsymbol{P_i}$	Polarization
P_s	Saturation polarization
P_r	Remnant polarization
$\boldsymbol{p}$	Electric dipolar moment
$\boldsymbol{E}$ **or** $\boldsymbol{E_i}$	Electric field
E_c	Coercive field
ε_{di}	Permittivity of the dielectric material
ε_0	Permittivity of vacuum
ε_F	Permittivity of P(VDF-TrFE)
ε_S	Permittivity of PTAA

k	Dielectric constant
Q	Charge
$\boldsymbol{d}$	Distance vector
$\boldsymbol{d_{ijk}}$	Piezoelectric coefficients
$\boldsymbol{d^{c}_{ijk}}$	Converse piezoelectric coefficients
$\boldsymbol{\sigma_{jk}}$	Mechanical stress
$\boldsymbol{\epsilon_{jk}}$	Mechanical strain
T	Temperature
T_c	Curie temperature
T_m	Melting temperature
Φ	Free energy
χ	Magnetic susceptibility
$\boldsymbol{H}$	Magnetic field
$\boldsymbol{M}$	Magnetization
M_s	Saturation magnetization
λ	Magnetostriction
λ_s	Saturation magnetostriction
t	Switching time
A_s	Surface area
ω	Frequency
ω_0	Resonance frequency
A	PFM amplitude
A_{max}	PFM amplitude at ω_0
φ	PFM phase
C_F	Capacitance of P(VDF-TrFE)
C_S	Capacitance of PTAA
w	Broadening of the polarized regions

w_e	Width of the electrodes
t_F	Layer thickness of P(VDF-TrFE)
t_S	Layer thickness of PTAA
W	Channel width
L	Channel length
V_{tip}	Tip voltage
V_{dc}	dc voltage
V_{ac}	ac voltage
V_g *or* V_{gs}	Gate voltage
V_d *or* V_{ds}	Drain voltage
$V_{s\&d}$	Voltage applied on source-drain electrodes
V_{dp}	Depolarization voltage
V_{th}	Threshold voltage
V_{pol} *or* $V_{tip,pol}$	Poling voltage
I	Current
I_d *or* I_{ds}	Source-drain current
I_{pol}	Polarization-induced current
I_{on} *or* I_{off}	On or Off current

Chapter 1

Motivation and Objectives

Organic electronics has proven to be a promising technology for large-area electronic applications, such as foldable displays[1, 2], electronic papers[2, 3], identification transponders[4], smart labels[5], and electronic skins[6]. These applications can hardly be achieved by inorganic silicon-based electronic devices, since they require being low-cost, light-weight, flexible, and large-area processable. Take radio-frequency identification (RFID) tags as an example; a simple RFID tag consists of a microchip, which is an integrated circuit and communicates with a reader via radio communication to send and receive information stored in its memory. The information is transferred wirelessly via magnetic or electromagnetic coupling between the reader and tag.[7] RFID tags made in silicon technology are already commercially available and are used, *e.g.*, to tag pallets of goods or to make access cards to buildings. However, silicon RFID tags are not yet suitable to tag individual goods that may be thrown away after use, because they are still not cheap enough for this application and are prone to mechanical failure if the goods are handled harshly during transport.[8] A route to solve both problems could be to fabricate the entire tag with flexible organic materials that are processed with low-cost solution-based techniques.

To go a step further, most of above mentioned applications of organic electronics including RFID tags, require memory functionality, preferably a non-volatile memory that retains its information when the power is turned off, and that can be programmed, erased, and read-out electrically. A memory element is an electronic device that can store information (binary 1 and 0), and should be fabricated based on functional materials with certain physical properties which could provide two distinguishable stable states that can be associated as bits 1 and 0. Among all the possible materials, organic electronic devices

based on ferroelectric polymers, *e.g.*, polyvinylidene fluoride (PVDF) and its copolymers with trifluoroethylene (P(VDF-TrFE)), have been proven to be ideal candidates for organic memory applications.[9-11] In general, memories based on organic ferroelectric polymers should meet several basic requirements: (i) in order to write and store the information (bits 1 and 0), at least two polarization states should be easily obtained by sending a stimulus to the ferroelectric polymer, *e.g.*, by applying a poling electric field, and these two polarization states should be retained after removing the poling field. This requirement actually refers to the switching (polarization and depolarization) mechanism and the polarization stability of the ferroelectric polymer. (ii) the reading of the information should be achieved by getting two distinguishable read-out states, *e.g.*, two current values by applying a small electric stimulus corresponding to two polarization states. Preferably, the applied small electric stimulus should not alter the polarization states of the ferroelectric polymer, giving non-destructive data read-out capability of a non-volatile memory. (iii) a proper design of the device structure is needed for easy operation of the memory devices, including the information storage, writing, and reading functionalities.

Comparing all the types of currently used ferroelectric memory devices such as ferroelectric capacitors, ferroelectric diodes, and ferroelectric field-effect transistors (FeFETs) (the general working principles of these three memory devices are presented in Section 2.2 of Chapter 2), FeFETs are considered to be one of the best choices as memory element, due to their easy processing, excellent memory performances, and non-destructive data read-out. Over the last decade, intensive efforts have been contributed to the optimization of the processing conditions and memory performances, and to the understanding of the working mechanism of memory FeFETs.[10, 12-21] However, at the beginning of this thesis, a complete explanation on working mechanisms was still lacking and the factors governing the polarization and depolarization of the ferroelectric polymer were still not fully investigated in FeFET devices, due to the complexity of their configuration resulting from the coupling of different functional

materials, and due to the lack of a proper technique for property characterization at the local (hundreds of nanometers) scale. In addition, except for the basic working principle, there are several parameters evaluating the performance of the memory devices such as the operating voltage (the poling voltage), the on/off current ratio, and the retention time. Within the framework of scientific and technological development and innovation, there are always possibilities and room to optimize these parameters and improve the memory performance, *e.g.*, by decreasing the operating voltage and increasing the on/off current ratio. Moreover, in addition to the three types of commonly used ferroelectric memory devices mentioned above, people are also seeking for new opportunities and structural designs based on ferroelectric materials. It is expected that more advanced devices and improved memory performance could be obtained from new structural designs and from the use and coupling of different functional materials.

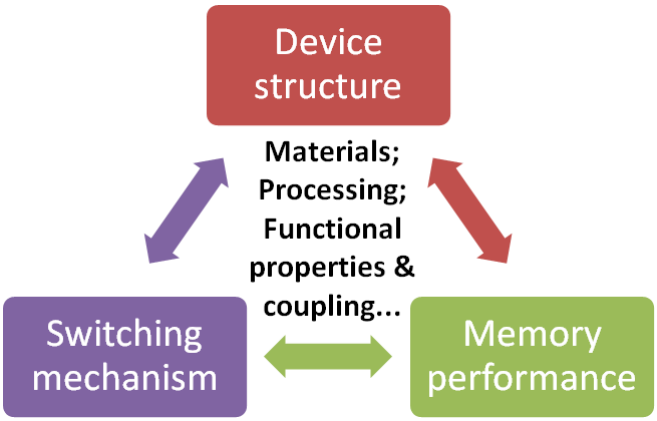

Figure 1.1: Gereral scheme of the relationship of ferroelectric memory device structure, ferroelectric switching mechanism, and memory performance.

Acturally, the basic requirements of ferroelectric memories mentioned above are not independent. As shown in Fig. 1.1, the memory device structure, the switching mechanism, and the memory

performance are all related to each other, depending on the employed materials, on the processing conditions, and on the coupling of different functional properties. Therefore, the main objective of this thesis is to explore the relationships between these parameters and thereby to reach a deeper understanding of coupling effects in ferroelectric memory devices. This objective is coupled to the effective fabrication of model devices, which are employed to help understanding these effects, and which may also be considered as one step towards new future devices.

While working on these objectives, we have also developed useful by-products, such as a better control and local characterization of material properties, a strong miniaturization of device size, the creation of nanopatterned structures and hybrid layers leading to multifunctional systems with coupled properties, and the design of new device configurations. Thanks to the development of nanotechnological tools and techniques, *e.g.*, nanoimprint lithography (NIL) and atomic force microscopy-based techniques, now we are able to manipulate materials and "see" material properties at the nanometer scale. As a consequence, many things which were unachievable before become now possible. For example, NIL can shape soft materials into nanoarrays or nanowires and simultaneously improve the functional properties of (semi)crystalline polymers, and atomic force microscopy-based techniques (*e.g.*, piezoresponse force microscopy, PFM) can be used to study electrical properties locally. NIL and PFM techniques are the basis of all the work presented in this thesis.

In this context, several sub-objectives are focused in this thesis in order to reach the main objective:

1. In Chapter 3, study the working mechanism of organic FeFET devices, including mapping the polarization and depolarization of ferroelectric P(VDF-TrFE) locally by using PFM, and exploring the factors governing ferroelectric polarization and memory performance;

2. In Chapter 4, improve the ferroelectric properties of P(VDF-TrFE), *e.g.*, decrease its coercive field, by crystallizing it in nanotrenches of a NIL mold, which results in well aligned arrays of P(VDF-TrFE) nanowires. Then try to reduce the operating voltage of memory FeFETs by integrating these nanowires in FeFET devices;

3. In Chapter 5, design novel transistor-like memory devices consisting of a hybrid layer with alternating ferroelectric and semiconducting nanowires produced by NIL, study the electrostatic coupling between the ferroelectric and semiconducting polymer nanowires and the polarization of the ferroelectric polymer in this hybrid layer, and demonstrate the memory functionality of this new device;

4. In Chapter 6, fabricate muliferroic layers by electrochemically depositing a ferromagnetic material into the nanopores of a P(VDF-TrFE) template produced by NIL, and study the magnetoelectric coupling between the ferroelectric and ferromagnetic phases, which could be potentially used for memory applications. The multiferroic system developed in this chapter is still on the stage of basic research. The reason why we developed this system is double: first, we wanted to study another type of coupling between two materials, and show whether the tools we used for the first part of the thesis were still efficient; second, on the long term, we want to control/switch and detect the polarization of P(VDF-TrFE) (these correspond to the writing and reading of the information in a memory device) by independent channels, *e.g.*, switching the polarization by a magnetic field and detecting it by an electric field. By this way, we could obtain even more stable polarization states compared to the ones obtained in traditional ferroelectric memories (*e.g.*, FeFETs), in which both the switching and detection of the polarization states are done by applying electric fields; in this case, there is always a risk to change the polarization state of the ferroelectric material during the read-out process. By working with two independent channels in the multiferroic system, this risk could be effectively avoided.

Before going through this work, Chapter 2 briefly reviews background knowledge related to the relevant functional materials (with a main focus on ferroelectric P(VDF-TrFE)), as well as on memory devices based on ferroelectric P(VDF-TrFE); in addition, two techniques, NIL and PFM, are introduced. Finally, Chapter 7 summarizes the main results and discussions resulting from our work and presents some perspectives for future work.

Chapter 2

Background and Methodology

In this chapter, the theoretical background and the practical methodology related to the work conducted in this thesis are presented. The materials/polymers used in this thesis, which display functional properties such as ferroelectricity, semiconductivity and ferromagnetism, are first discussed in Section 2.1, with the main focus being on ferroelectric P(VDF-TrFE) copolymers, followed by a brief review of their applications for organic ferroelectric memory devices in Section 2.2. Then, nanoimprint lithography (NIL), the tool employed here to shape the ferroelectric polymer, is presented in Section 2.3. In this section, the reasons why NIL is integrated in the fabrication of memory devices are also discussed. Then scanning probe microscopy (SPM), which is the main technique used to characterize the memory devices, is described in Section 2.4. Two SPM techniques, atomic force microscopy (AFM) and piezoresponse force microscopy (PFM), are used to characterize the topography and the ferro/piezoelectric response of the samples, respectively. The other tools and techniques used to characterize the devices are briefly introduced in Section 2.5.

2.1 Materials

2.1.1 Ferroelectric Polymers

Ferroelectricity was discovered in 1921 in Rochelle salt by Valasek. It was described as follows: "Rochelle salt shows an electric hysteresis in *P* (polarization) analogous to the magnetic hysteresis in the case of iron. The loops obtained are displaced from the origin by an amount which gives a measure of the permanent polarization in the natural state."[22] After that, the discoveries of ferroelectric barium titanate ($BaTiO_3$) and lead zirconate titanate ($Pb(Zr,Ti)O_3$, PZT) family of ceramics, both with common ABO_3 perovskite structure, promoted quite a lot of research efforts aiming at understanding and applying commercially these inorganic ferroelectric materials. Now, perovskite ceramics are widely used in electronic devices, *e.g.*, in transducers, thermistors, sensors and memory capacitors.[23, 24] The typical crystal structure of a ABO_3 type perovskite material is shown in Fig. 2.1.1. In this structure, the application of an electric field or a mechanical force can induce the displacement of the central B cation, which is the reason for the formation of the dipole moment and spontaneous polarization.

On the other hand, organic ferroelectrics also exist, but are only limited to several polymers and few low molar mass compounds.[25-27] Different from inorganic ferroelectrics where atoms pack into simple ordered crystal lattices, organic ferroelectrics have a more complex structure.[26, 28] In general, ferroelectric polymers are macromolecules with a low degree of symmetry, in the solid-state structure of which crystalline and amorphous regions coexist. Typical examples are polyvinylidene fluoride (PVDF) and its copolymer with trifluoroethylene (P(VDF-TrFE)), in which the ferroelectricity originates from the strong dipole moment of the CH_2-CF_2 repeating unit. Compared to other organic ferroelectrics such as odd-nylons,[29] thiourea,[30] liquid crystalline polysiloxanes,[31] and co-crystals of nonpolar organic molecules,[32] PVDF and its copolymer P(VDF-TrFE) are the most intensively studied organic ferroelectric materials, due to their good chemical and mechanical resistance, large dipole moment

and polarization, excellent polarization stability, relatively short switching time, low processing temperature and easy solution-based processing conditions. Therefore, P(VDF-TrFE) will be employed as the ferroelectric polymer in this thesis, and a detailed introduction to this polymer and a brief view of recent advances will be presented in a subsection.

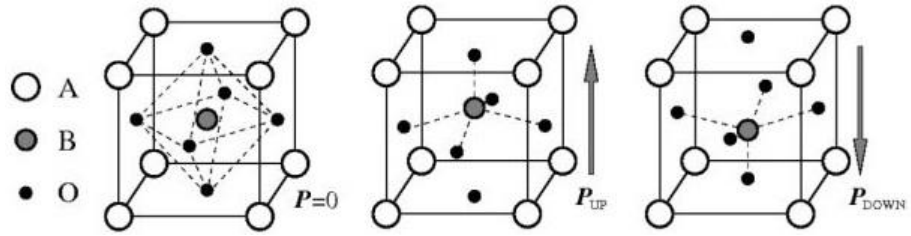

Figure 2.1.1: Crystal structures of ferroelectric perovskite oxides ABO_3 in the original (left) and polarized states (middle and right) with upward and downward polarization. The central atom B is typically a cation, *e.g.* Ti^{4+} or Zr^{4+}, which can be displaced by the application of an electric field or a mechanical stress, resulting in the formation of the electric dipole moment and spontaneous polarization. Adapted from[33]

2.1.1.1 Ferroelectricity

Ferroelectricity refers to a spontaneous electric polarization of a material that can be reversed by applying an external electric field. This polarization can be mathematically defined by the constitutive equation:

$$\boldsymbol{D} = \varepsilon_{di}\boldsymbol{E} + \boldsymbol{P} \qquad \text{(Equation 2.1.1)},$$

with $\boldsymbol{P}$ the polarization, $\boldsymbol{D}$ the dielectric displacement and $\boldsymbol{E}$ the electric field. ε_{di} is the permittivity of the dielectric material, which takes into account the induced polarization arising from the application of the electric field. This parameter is usually referred to the relative permittivity or dielectric constant k by:

$$k = \varepsilon_{di}/\varepsilon_0 \qquad \text{(Equation 2.1.2)},$$

with ε_0 the permittivity of vacuum. If we consider a non-ferroelectric material or replace the dielectric material by the vacuum, meaning that there is no spontaneous polarization, the equation becomes:

$$\boldsymbol{D} = \varepsilon_{di}\boldsymbol{E} \text{ or } \boldsymbol{D} = \varepsilon_0\boldsymbol{E} \qquad \text{(Equation 2.1.3).}$$

The polarization $\boldsymbol{P}$ originally arises from the internal permanent electric dipoles and the direction of these dipoles can be aligned up or down depending on the direction of the applied external electric field. If two charges $+Q$ and $-Q$ are separated by a distance $\boldsymbol{d}$ in a dipole, an electric dipolar moment $\boldsymbol{p}$ forms as:

$$\boldsymbol{p} = Q\boldsymbol{d}, \qquad \text{(Equation 2.1.4),}$$

with $\boldsymbol{d}$ the distance vector connecting the two charges (oriented from $-Q$ to $+Q$). Then the polarization $\boldsymbol{P}$ can be defined as the total electric dipolar moment per unit volume:

$$\boldsymbol{P} = \sum \boldsymbol{p}/V \qquad \text{(Equation 2.1.5),}$$

with V the total volume. The definition of the polarization $\boldsymbol{P}$ clearly shows that it is determined by the magnitude of the dipolar moments, their orientations and their density. It should be noted that the polarization $\boldsymbol{P}$ is hysteretic, which means that it depends on the history of application of the field, and not only on the instantaneous applied field itself. A typical hysteresis curve of D versus E (displacement versus external electric field in one dimension) is shown in Fig. 2.1.2, where P_s is the saturation polarization when all the dipoles are aligned by the external field, P_r is the remnant polarization defined as the remaining polarization after removing the external electric field (E = 0), and E_c is the coercive field which is the field needed to reduce the polarization to zero (P = 0). It is worth noting that ferroelectricity is an ideal physical property for memories, due to the presence of two stable polarization states in ferroelectric materials which can be easily detected as electric signals and therefore be associated to bits 1 and 0.

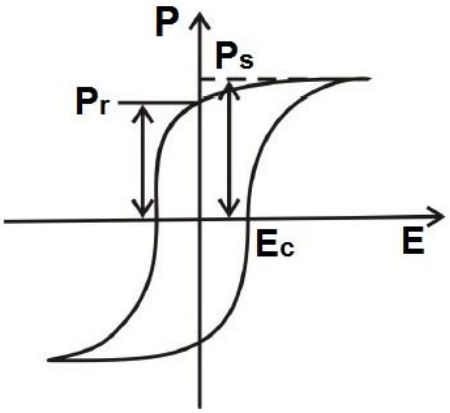

Figure 2.1.2: Typical ferroelectric hysteresis loop where P_s, P_r, and E_c are indicated.

On the other hand, all ferroelectric materials are piezoelectric, even though the reverse is not true. Piezoelectricity only exists in certain materials where an applied mechanical stress can change the polarization of the material (direct piezoelectric effect) and *vice versa* (converse piezoelectric effect).[34] These materials do not have inversion symmetry, and the applied mechanical stress can modify the separation between the positive and negative charge sites in each unit cell, or the orientation of the electric dipoles, leading to a net polarization appearing at the material surface.[35] The piezoelectric effect is a linear electromechanical interaction between the mechanical and the electric states in piezoelectric materials, meaning that the change in polarization $\Delta \boldsymbol{P_i}$ varies directly with the applied mechanical stress $\boldsymbol{\sigma_{jk}}$ and can be mathematically expressed as:

$$\Delta \boldsymbol{P_i} = \boldsymbol{d_{ijk}\sigma_{jk}} \qquad \text{(Equation 2.1.6)}$$

where $\boldsymbol{P_i}$ is the polarization vector, and $\boldsymbol{d_{ijk}}$ is a third-rank stress tensor containing the piezoelectric coefficients. On the other hand, the converse piezoelectric effect expresses the linear relationship between the strain $\boldsymbol{\epsilon_{jk}}$ and the applied electric field $\boldsymbol{E_i}$:

$$\boldsymbol{\epsilon_{jk}} = \boldsymbol{d^c_{ijk}}\, \boldsymbol{E_i} \qquad \text{(Equation 2.1.7)}$$

where $\boldsymbol{d_{ijk}^{c}}$ are the converse piezoelectric coefficients.

In most cases, the piezoelectric tensor can be simplified due to crystalline symmetry and by making reasonable assumptions. For example, in a film of a ferroelectric polymers like P(VDF-TrFE), the most important component of the tensor is $\boldsymbol{d_{33}}$ which couples directly with the vertical electric field normal to the P(VDF-TrFE) film (the direction indexed as '3' being along the normal to the film). The typical value of $\boldsymbol{d_{33}}$ for P(VDF-TrFE) is *ca.* -35 pm/V, where the negative sign means that P(VDF-TrFE) contracts in the direction of the applied electric field. Most recently, the origin of this negative piezoelectric effect was re-investigated, and it was shown that the piezoelectric effect is dominated by the change in lattice constant of P(VDF-TrFE) crystals with an additional contribution which quantitatively describes the strain for all values of the electric field. The origin of this additional contribution is the electromechanical coupling between the intermixed crystalline lamellae and amorphous regions of the semicrystalline P(VDF-TrFE).[36]

The piezoelectric effect in ferroelectric materials is important, especially for composite multiferroic layers which will be presented in Chapter 6, wherein the magnetoelectric coupling results from the piezoelectricity and magnetostriction of the ferroelectric and ferromagnetic materials, respectively.

Moreover, ferroelectric materials have a critical temperature (called the Curie temperature, T_c), above which the materials change from ferroelectric to paraelectric phase and loose their ferro- and piezo-electric character. This phase transition results from the packing of the molecular chains changing from a more ordered to a more disordered state.

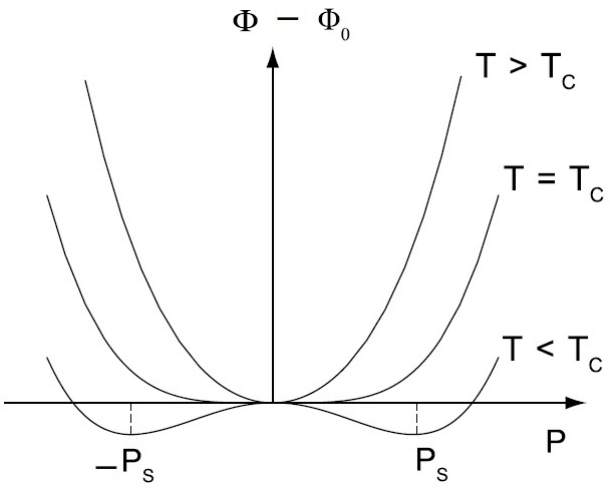

Figure 2.1.3: Thermodynamic approach for a general ferroelectric material with a second-order transition. The graph presents the dependence of free energy Φ on polarization *P* at three different temperatures (T_c is the critical Curie temperature). Adapted from[37]

In addition, from a thermodynamic point of view, for a general ferroelectric material, the origin for the formation of a ferroelectric polarized state is that it corresponds to a stable thermodynamic equilibrium state.[37] As shown in Fig. 2.1.3, the ferroelectric phase, when sandwiched between two electrodes, has minimized energy levels for two polarizations below T_c. Above T_c, a single lowest energy state only exists at $P = 0$, in which case the material becomes paraelectric.

2.1.1.2 P(VDF-TrFE)

The ferroelectricity of the semicrystalline PVDF originates from the dipole moments of the CH_2-CF_2 dipoles resulting from the different electronegativities of F, C, and H atoms. However, it requires more to be ferroelectric, *i.e.*, the conformation and packing of the polymer chains should be organized in a proper way in the crystalline regions. Depending on the chain conformations which involve a succession of

trans (T) and *gauche* (G) torsion angles along the backbone of the chain, and the way of the chain packing, PVDF has at least four different polymorphs: α, β, γ, and δ phases.[25, 28] α-phase PVDF has a TGTG' conformation consisting of alternating *trans* (T) and *gauche* (G) carbon bonds packed in an antiparallel way (Fig. 2.1.4, top). Due to this configuration, the α-phase PVDF has a centro-symmetric packing making it the most stable phase in which the dipole moments of each chain cancel each other out; therefore, the α-phase is non-polar and paraelectric. In contrast, β-phase PVDF is ferroelectric and has an all-*trans* (TTTT) conformation, as shown in Fig. 2.1.4 (middle), which results in the alignment of the dipole moments and in a large net spontaneous polarization. In general, ferroelectric β-phase films are produced from α-phase PVDF by biaxial mechanical stretching, which is not very practical for specific applications.[38] In addition, the fraction of the β-phase in PVDF films is limited (max. *ca.* 50%), even at optimized deposition conditions.[39] γ-phase PVDF (Fig. 2.1.4, bottom) is intermediate between the α and β phases, and the chains are packed in a polar way; therefore, it is ferroelectric but experimentally less accessible, because its formation typically requires a very fine temperature control and high pressures.[40, 41] δ-phase PVDF is a polar version of the α-phase (see reference 42 for the detailed molecular packing and crystal structure of δ-phase PVDF); ferroelectric, neat thin films of this phase were recently prepared and re-investigated by Li *et al.*[42] Its relatively easy preparation process leads to thin films of good quality; hence δ-phase PVDF was proposed to be a good candidate for applications based on ferroelectricity.

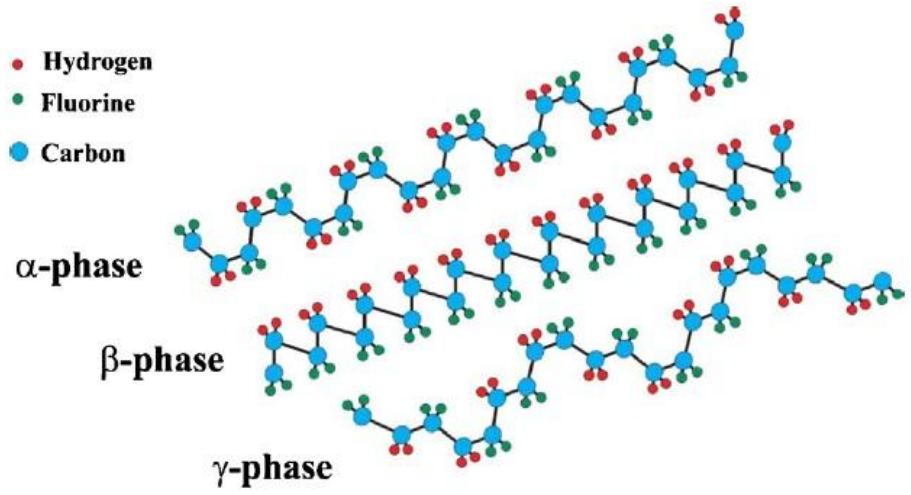

Figure 2.1.4: Schematic representation of the chain conformation for the α, β, and γ phases of PVDF. Adapted from[43]

As mentioned above, there are limitations for practical applications of ferroelectric PVDF including its relatively low crystallinity and β -phase content. In addition, the stable non-ferroelectric α-phase is generally formed when processed from the solution or the melt. Several methods have been reported to increase the β-phase fraction of PVDF, *e.g.*, by adding small amounts of an ionic liquid[44] or by blending with polymethylmethacrylate (PMMA)[45, 46]. In addition to these methods, another specific way is to copolymerize VDF with trifluoroethylene (TrFE), forming a random P(VDF-TrFE) copolymer, which favors the formation of the all-*trans* polar β -phase directly from the melt or solution.[26, 47, 48] By introducing a certain amount of TrFE units in PVDF (typically 30 mol%), some smaller hydrogen atoms are randomly replaced by larger fluorine atoms, inducing severe instability in the TGTG' conformation (α-phase). To relax this instability, the all-*trans* conformation is favored in P(VDF-TrFE); this conformaiton is similar to that in the β-phase of PVDF which is polar and ferroelectric. In addition to the easy formation of the ferroelectric phase, the crystallinity of the polymer can be enhanced from ca. 50% up to 90%. Therefore, a

ferroelectric phase with high crystallinity can be obtained directly from a P(VDF-TrFE) solution or melt. Moreover, due to the addition of TrFE units, P(VDF-TrFE) has a lower Curie transition temperature T_c than PVDF, and T_c is smaller than the melting temperature T_m for P(VDF-TrFE) (while T_c is larger than T_m for PVDF). Although a decreased T_c results in a smaller thermal stability of the ferroelectric properties, it also provides several advantages: first, to enhance the crystallinity, an annealing process is typically needed in the paraelectric phase above the Curie temperature. However, the annealing should not be performed above the melting temperature; otherwise, a generally unfavorable crystal orientation ensues. In contrast, when annealing in the paraelectric phase between the Curie and the melting points, a more favorable crystal setting emerges, which can thus be easily done for P(VDF-TrFE).[49] Second, the paraelectric phase is a liquid-crystalline state and is soft with a lower hardness.[50] This is particularly interesting for nanoimprint lithography (NIL), a main technique used in this thesis to shape P(VDF-TrFE). Indeed, NIL can be directly performed in the paraelectric phase of P(VDF-TrFE), and the polymer chains can be pushed into the openings of NIL molds at reasonable pressures, due to the reduced hardness of P(VDF-TrFE).

The phase diagram of P(VDF-TrFE) is shown in Fig. 2.1.5, in which one can see more clearly the dependence of T_c and T_m on the content in TrFE or VDF units. The main polymorph phases depending on the composition of P(VDF-TrFE) are also indicated in the phase diagram. It is clear that, below about 80% VDF, the Curie transition temperature is below the melting point, and copolymers in the range of 60% and 80% VDF afford the most comprehensive range of ferroelectric and related properties. To note, the P(VDF-TrFE) used in this thesis has a composition of 30 mol% TrFE with an average molar mass of *ca.* 300 000 g/mol, and the Curie and melting temperatures of this grade of P(VDF-TrFE) are 94.5 ℃ and 146.5 ℃, respectively, as measured by differential scanning calorimetry (DSC). This specific grade of P(VDF-TrFE) is chosen because it has a large temperature NIL operating window (NIL is performed in-between the Curie and

melting points, which provides softness without degradation of ferroelectric properties after cooling).

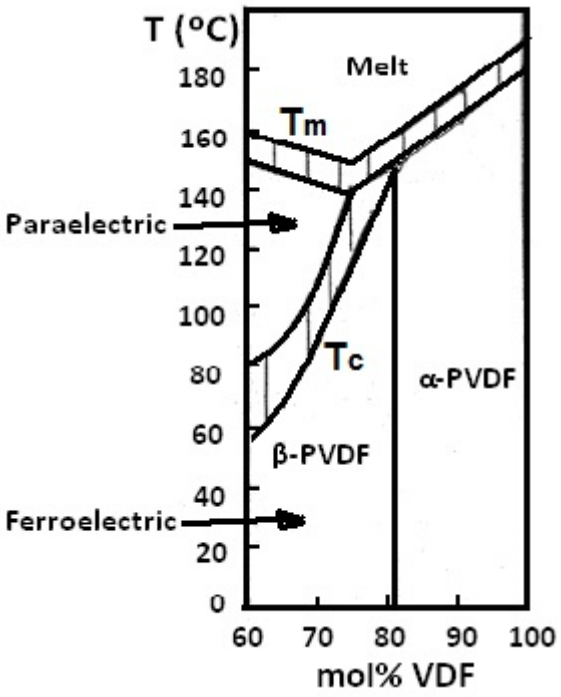

Figure 2.1.5: Phase diagram of P(VDF-TrFE) copolymers. Adapted from[51]

Apart from the basic chain conformation, the ferroelectric properties of P(VDF-TrFE) are determined by many parameters, *e.g.*, the microstructure of the polymer and the operation conditions, which have been intensively studied. The microstructure was characterized by techniques such as X-ray diffraction,[52-55] infrared and Raman spectroscopy,[55-57] and atomic force microscopy (AFM).[57, 58] The results show that in the crystals of the β phase P(VDF-TrFE), the molecular chains adopt a quasi-hexagonal packing, as shown in Fig. 2.1.6, where the c-axis is along the carbon backbone direction and the b-axis is along the direction of the dipole moments and spontaneous polarization. Then, these molecular chains are folded many times to form crystalline lamellae, which are generally observed in AFM

images (typical AFM images of nanoimprinted P(VDF-TrFE) will be shown in the section "Nanoimprint Lithography" of this chapter). The β phase crystals are interconnected by molecular chains in the amorphous regions, forming semicrystalline P(VDF-TrFE).

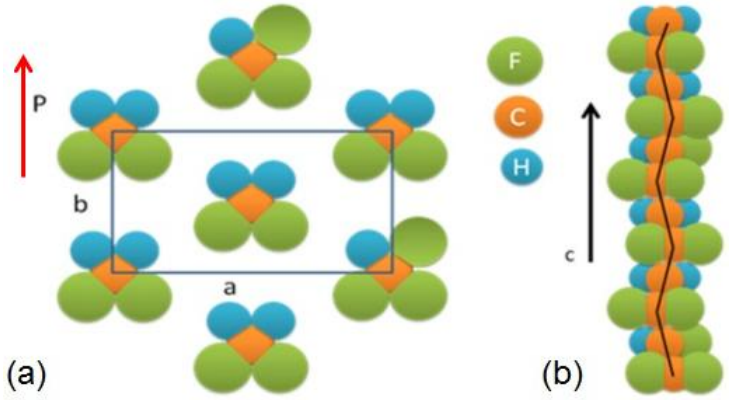

Figure 2.1.6: Schematic drawing of the crystal structure of the β phase P(VDF-TrFE), (a) in the ab plane (the c axis is practically normal to the ab plane), and (b) along the c axis of the all-*trans* (TTTT) planar conformation from the top view. Adapted from[59]

The ferroelectric hysteresis loops at different operation conditions (*e.g.*, bias amplitude and frequency, temperature) and the polarization stability information (*e.g.*, endurance and retention properties) of P(VDF-TrFE) films after different treatments, are measured most often in capacitor structures, and will therefore be discussed in the "Ferroelectric Capacitors" section of this chapter. In addition, it became recently possible to characterize the local ferroelectric properties of P(VDF-TrFE) films by means of piezoresponse force microscopy (PFM), in which a conductive tip is used to detect the local eletromechanical coupling of P(VDF-TrFE). This methodology is especially useful for nanostructured P(VDF-TrFE), or P(VDF-TrFE) integrated in complex device structures like ferroelectric field-effect transistors, since one can perform experiments at the nanometer scale and obtain a spatially-resolved information on the ferroelectric behaviour of P(VDF-TrFE).[57, 58, 60-62] Therefore, in this thesis, PFM

was employed as the main technique to characterize the ferroelectric properties of P(VDF-TrFE).

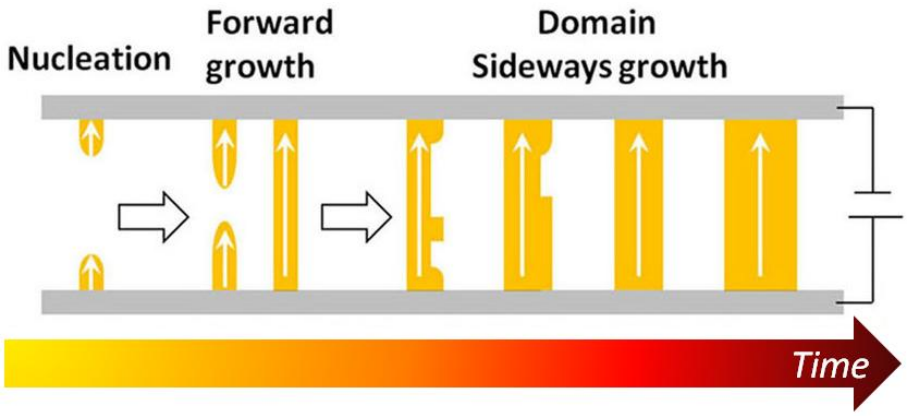

Figure 2.1.7: Schematic description of a universal polarization switching process which involves nucleation, forward domain growth and sideways domain growth through kink nucleation, spanning many time scales. Adapted from[63]

Another important characteristics of ferroelectric P(VDF-TrFE) is its polarization switching behaviour. As illustrated in Fig. 2.1.7, the universal polarization switching process of ferroelectric materials microscopically involves nucleation, forward domain growth and subsequent sideways growth. The time needed for nucleation and forward domain growth is typically in the range of nanosecond, while for sideways domain growth it ranges from several nanoseconds to seconds or even longer depending on various intrinsic and extrinsic factors.[64, 65] Furthermore, defects and structural disorder introduced during synthesis and film preparation can significantly influence the switching dynamics in P(VDF-TrFE) films, by acting as nucleation centers and pinning sites for domain wall motion.[63] In general, the switching mechanism of P(VDF-TrFE) is governed by the rotation of the molecular chains in the polycrystalline P(VDF-TrFE) films and several models have been proposed to explain the switching mechanism of P(VDF-TrFE). To list a few important ones, the so-called nucleation-limited-switching (NLS) model developed by

Tagantsev *et al.*, in which the switching of each region is independently determined by its own nucleation rate and domain dimension and the switching of the whole film is controlled by the statistics of domain nucleation in each region,[66] was found to be a reasonable description of the ferroelectric switching for P(VDF-TrFE), in line with experimental results.[67] Hu *et al.* suggested that the polarization switching in P(VDF-TrFE) film could be well described by the classic Kolmogorov-Avrami-Ishibashi (KAI) model, which describes the switching by domain nucleation together with unrestricted domain expansion and domain wall motion throughout the film.[63] Recently, our group was involved in the publication of a two-step polarization switching mechanism, in which both crystalline and amorphous components take part in the polarization switching.[62] This mechanism describes the polarization switching by fast domain wall flow motion in the crystals, pinned by the amorphous components at the crystal boundaries. When increasing the amplitude or duration of the voltage pulse, the pinning is overcomed by the external driving force and the domain propagates across amorphous regions through bridging chains located at the interfaces between lamellae and surrounding amorphous components. This process can be described by a model of creep motion. This two-step polarization switching mechanism can explain very well the recently observed fractal domain patterns[68, 69] and the crossover behaviour of frequency-dependent coercivity found in P(VDF-TrFE) thin films.[63] This mechanism can also explain why stable polarization states can exist in nanostructured P(VDF-TrFE) of very small dimensions, despite the possible unstability of very small ferroelectric domains; indeed, depolarization would be avoided because creep motion is extremely slow at zero poling bias, thanks to the pinning of the polarization by the amorphous regions. This possibility is tremendously interesting for practical applications such as memory devices, because high density memory arrays can be realized, as actually demonstrated in early reports.[58, 70] Decreasing the dimensions of ferroelectric P(VDF-TrFE) components to scale down the memory size and increase the memory density is also one approach of this thesis.

2.1.2 Semiconducting Polymers

Materials can be grouped into insulators, semiconductors, and conductors based on their electric conduction which is described by band structure theory as illustrated in Fig. 2.1.8. Insulators are materials in which the higher lying valence band is completely filled, while the lower lying conduction band is empty, *i.e.*, contains no electrons; as a result the electrons in an insulator cannot physically move in response to an applied electric field. Typically, insulators have wide band gaps (*e.g.*, > 9 eV), which describe the energy difference between two bands. Metals, on the other hand, have overlapped valence and conduction bands and thus contain a partially filled conduction band, whose conduction electrons move easily in response to an external electric field. Semiconductors are insulators in which the band gap between valence and conduction bands is sufficiently small that at temperatures of interest, a fraction of the electrons in the valence band can be energetically excited to the conduction band (leaving behind holes, unoccupied states in the valence band); therefore, both the conduction electrons and the holes can move in response to an applied electric field. The excitation of electrons can be controlled, resulting in the tuning of charge transport in semiconductors, which is the basis of modern functional electronics.

Semiconductors are an essential part of electronics. Their importance can be seen from the fact that semiconductor industry in Year 2015 was a $335 billion market in the world.[71] Although inorganic semiconductor-based electronic devices are already cost-effective, people are still seeking for cheaper products with good performance. In this respect, organic semiconductors display a niche potential for cheap electronic device fabrications, due to their advantages such as being easily processed, flexible, low cost and light weight. In addition, organic chemistry can help tailor the materials to achieve desired properties by modifying functional groups and/or by chemical doping.

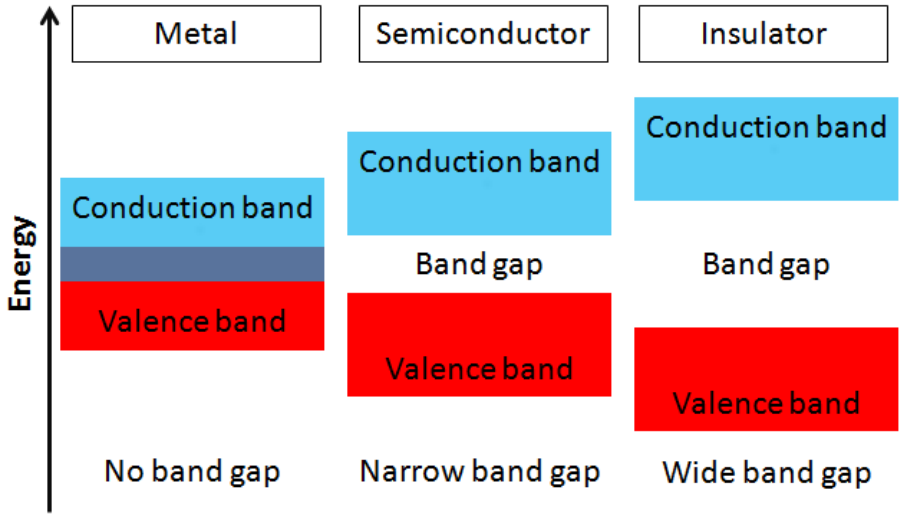

Figure 2.1.8: Band structure of insulators, semiconductors, and conductors.

The structure of all organic semiconductors has a common feature of π-conjugated bonds, meaning that the polymer/molecule consists of alternating single and double bonds, as typically present in conductive polyacetylene that was synthesized in 1977 (Fig. 2.1.9).[72, 73] The discovery of conductive polyacetylene promoted the fast development of organic semiconductors for which A. Heeger, A. G. MacDiarmid and H. Shirakawa were awarded the Nobel Prize in Chemistry in 2000.[74] The π-conjugated bonds structure gives rise to the possibility of electron transport over delocalized π-orbitals. However, all electrons are paired in π-orbitals of undisturbed conjugated backbones, with as a result no charge being free to move although electrons are partially delocalized. So, to be electrically (semi)conductive, it is not sufficient to have a conjugated structure. The polymer/molecule has also to be chemically doped to introduce mobile charges, *e.g.*, by oxidizing or reducing the polymer through (electro)chemical reactions, or by incorporating cyclic conjugated moieties (*e.g.*, aromatic cycles) into the backbone. After these processes, mobile positive or negative charges (holes or electrons) are present, which determines the conduction origin and the type of the organic semiconductor: p-type or

n-type. p-type and n-type mean that charges moving through the semiconductor are positive holes and negative electrons, respectively. There are also some polymers called ambipolar organic semiconductors which are able to conduct both electrons and holes.

Organic semiconductors must satisfy general criteria to achieve acceptable performance[75]: (i) the band gap, defined by the energy difference of the highest occupied orbital (HOMO) and the lowest unoccupied orbital (LUMO), has to be at a level where electrons and/or holes can be accumulated by accessible electric fields; (ii) because the most efficient charge transport occurs along the direction of intermolecular π-π stacking, the structure of the polymer has to supply sufficient overlap of π-orbitals and the molecules have to be preferentially oriented with their backbone parallel to the interface where mobiles charges are accumulated; (iii) the material should be as pure as possible to avoid charge trapping by impurities. For semiconductor devices, the performance also depends on device parameters, for example, the quality of the semiconductor/dielectric interface.

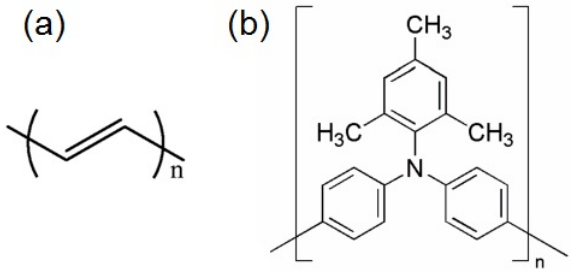

Figure 2.1.9: Chemical structures of (a) polyacetylene and (b) PTAA.

In this thesis, the polymer semiconductor PTAA (poly(triarylamine)) is used as the main one to fabricate FeFETs. Its structure is shown in Fig. 2.1.9 (b). PTAA is a p-type semiconductor and the reasons why it was chosen despite its relatively low carrier mobility are that PTAA is an amorphous polymer which can achieve very smooth films by spin coating, so that an interface of high quality

can be realized for transistors in a top-gate/bottom-contact configuration, and that PTAA is stable in air so that its processing does not need to control environment (inert atmosphere).[76, 77]

2.1.3 Ferromagnetic Materials[78-82]

Ferromagnetism is a well-known phenomenon displayed by ferromagnetic materials (*e.g.*, transition metals such as Fe, Co, Ni and their alloys) that present spontaneous magnetization. According to the Pauli exclusion principle, two identical electrons cannot have the same quantum state simultaneously, which means two electrons residing in the same orbital and having the same magnetic quantum number must have opposite half-integer spins, 1/2 and -1/2. However, in some materials like ferromagnetic materials in which the outer 3d shell is not fully occupied by electrons, two electrons occupying the same orbital would be very close to each other and result in a large exchange interaction due to repulsive Coulomb forces. This is not energetically favourable. Therefore, these two electrons prefer to have same spin state and occupy two different orbitals, in which case the exchange energy (the energy due to the repulsion between the two electrons) is minimised. This results in the parallel alignment of the electron spins and a net non-zero spontaneous magnetization (an electron has a magnetic dipole moment associated to its spin).

Ferromagnetism is only present below a critical temperature, T_c, called the Curie temperature as for ferroelectrics, above which the ferromagnetic material becomes paramagnetic because thermal energy is large enough to overcome the cooperative ordering of the magnetic moments. This can be described by the Curie-Weiss law, stating that the magnetic susceptibility χ, indicating how the magnetization M of the material responds to an applied magnetic field H, varies with temperature T and becomes infinite when temperature tends to T_c. This gives the following equation: $\boldsymbol{\chi = \frac{M}{H} = \frac{C}{T-T_c}}$, where C is a material-dependent constant. Below T_c, the thermal excitation energy is low and the magnetic moments of the atoms are aligned leading to

spontaneous magnetization. The saturation magnetization of the ferromagnetic material decreases with increasing temperature as the thermal excitation disorients the magnetic moments, and reaches zero at the Curie temperature.

However, on a macroscopic scale, the ferromagnetic material does not have only one domain with all magnetic moments aligned in the same direction, but consists of many magnetic domains (within each of which magnetic moments are still aligned in the same direction) with different magnetization directions. The formation of these domains is mainly driven by the minimization of the magnetostatic energy (suppressing the demagnetization stray field, blue arrows), as shown in Fig. 2.1.10, together with other sources of magnetic energy such as the magnetocrystalline energy and the magnetostrictive energy. Boundaries between different domains are called domain walls where the direction of magnetization changes gradually.

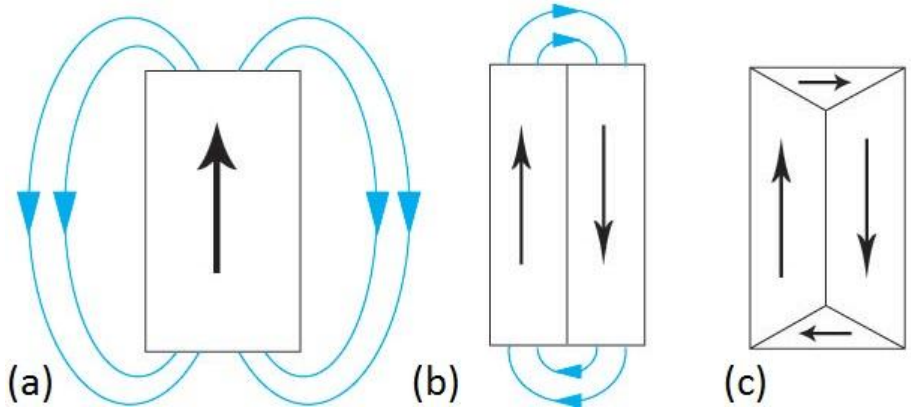

Figure 2.1.10: Schematic drawing on how the formation of domains can reduce the external demagnetizing field (blue arrows) and therefore minimize the magnetostatic energy. Adapted from[82]

In analogy to ferroelectricity, the ferromagnetic material also presents magnetic hysteresis in response to the external magnetic field, as shown in Fig. 2.1.11 (a). When an external magnetic field *H* is

applied to the ferromagnetic material in its demagnetized state, the domain walls move and the energetically favoured domains grow at the cost of other domains. When H is high enough, all the magnetic moments align in the direction of the applied field and the saturation magnetization M_s is reached. When H is decreased to zero, a remnent magnetization M_r is achieved. In order to switch the net magnetization to zero, an opposite magnetic field, called coercive field H_c, needs to be applied. A completed hysteresis loop is formed when the same reversed process is finished.

In general, magnetic anisotropy exists in ferromagnetic materials such as magnetocrystalline anisotropy and shape anisotropy. Magnetocrystalline anisotropy originates from the atomic lattice structure where the magnetization is easier or harder along different directions. Shape anisotropy originates from the dimensional difference of the ferromagnetic materials, *i.e.*, for long wires, the easy axis is along the wire direction and for thin plates, the easy axis is in-plane. In general, different hysteresis loops are obtained in different directions, *i.e.*, the loop is more squared in the easy axis direction and more tilted along the hard axis direction.

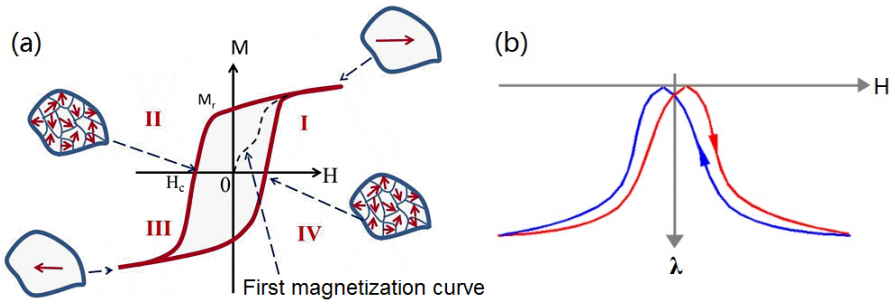

Figure 2.1.11: (a) Typical magnetization hysteresis loop and magnetic domain morphology of ferromagnetic materials. (b) Typical magnetostriction hysteresis loop of ferromagnetic materials whose magnetostriction is negative. Adapted from[83]

Another important phenomenon existing in ferromagnetic materials is the magnetostriction effect which describes the deformation of the ferromagnetic material when the magnetization

changes due to the applied magnetic field. The magnetostriction λ is defined as the fractional change of the length L of the material: $\boldsymbol{\lambda = \frac{\Delta L}{L}}$, which reaches a saturation λ_s when the ferromagnetic material is completely magnetized. A typical magnetostriction curve is shown in Fig. 2.1.11 (b), for which λ is negative, meaning that the ferroelectric material contracts in the presence of a magnetic field. Nickel (Ni) is such a material with a λ_s of about -10^{-5}; it will be used in the multiferroic layers made in this thesis.

Summing up, three types of functional materials, ferroelectric polymers, semiconducting polymers, and ferromagnetic materials were presented in this section and will be used in this thesis. First, ferroelectric devices using a combination of ferroelectric P(VDF-TrFE) and semiconducting PTAA will be fabricated and the electrostatic coupling between these two materials will be studied in different device configurations (Chapters 3-5). Then, multiferroic layers employing ferroelectric P(VDF-TrFE) and ferromagnetic Ni will be fabricated in order to investigate the strain-mediated magnetoelectric coupling in these layers (Chapter 6).

2.2 Organic Ferroelectric Memories

The ability to store information is essential for many applications of electronic devices, *e.g.*, radio frequency identification tags where the information is stored and communicated by means of a radio signal. With the increasing demanding of light-weight, flexible, and low-cost applications, organic electronic and memory devices are considered to be able to provide a complementary solution to inorganic electronics. To realize the memory functionality, a memory device needs to make use of a physical property which can provide at least two stable states for bit storage. In addition, this physical property needs to be integrated in an electronic device, in which the two stable states can be easily written and read out by applying an electrical field. The read-out of the memory states is preferably non-destructive, which means that the stable states and stored information are not altered by

the applied read-out voltage, resulting in non-volatile memories. Moreover, the memory device components need to be easily integrated in the logic circuits of the functional electronic devices, which requires proper design of the memory device configurations, preferably similar to the ones which are widely used in currently existing electronic devices. Apart from these basic requirements, a decent memory device in general has features of low operation voltage, short switching time, high on/off ratio, long retention time, and good endurance without failure due to fatigue occurring after a large number of switching cycles.

Based on these considerations, ferroelectricity appears to be an excellent such physical property, which exhibits two stable polarization states in a characteristic hysteresis in response to an external electric field. As mentioned in previous sections, the ferroelectric P(VDF-TrFE) is the most promising ferroelectric polymer for memory applications. The last decade has witnessed increasing interest and intensive studies on ferroelectric memory devices employing P(VDF-TrFE) as memory storage component. In the literature, there are mainly three device configurations that are proposed: ferroelectric capacitors, ferroelectric diodes, and ferroelectric field-effect transistors. In the subsequent sections, a brief overview of these basic memory elements is presented. The working principle of each element and their advantages and disadvantages are also briefly discussed.

2.2.1 Ferroelectric Capacitors

A ferroelectric capacitor is the simplest memory element, having a ferroelectric layer sandwiched between two electrodes. Information is stored by aligning the ferroelectric polarization direction either up or down by applying a sufficiently large electric field, as schematically shown in Fig. 2.2.1. To read the information, a switching voltage is applied to obtain a low or a high charge displacement current response depending on whether the polarization is aligned or not with the

direction of the applied field. Ferroelectric capacitors therefore have a destructive read-out since the information read-out can affect the polarization state and the stored information. A reset voltage is needed afterwards if the polarization direction was changed during the read operation, which is considered to be a main drawback of the ferroelectric capacitor memory.

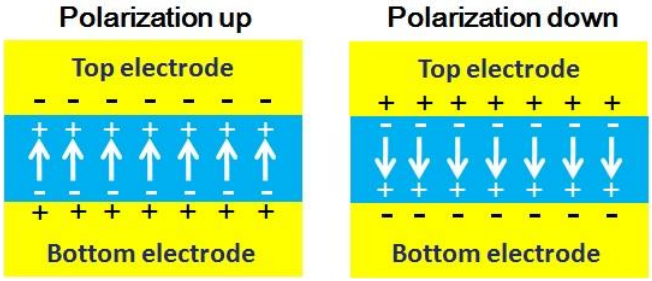

Figure 2.2.1: Schematic view of two stable polarization states (up and down) of a ferroelectric layer sandwiched between two electrodes. These two polarization states can be used to store information by associating them with bits 1 and 0. Arrows indicate the direction of the polarization. The polarization charges and the screening charges provided by the electrodes are also shown in the graph.

Several issues need to be addressed in order to make ferroelectric capacitors as good memory devices. The first one would be the operation voltage, which could be high considering the relatively high coercive field of P(VDF-TrFE) thin films (50-80 MV/m).[9, 20, 84] One way to achieve lower operation voltages is to decrease the film thickness, which, however, could result in an extremely retarded ferroelectric response as compared to the bulk material[85, 86] or even shortcuts between two electrodes due to pinholes and defects in the film. Efforts have been made in order to decrease the film thickness, while retaining a similar ferroelectric response compared to the bulk material. One attempt to fabricate ultrathin layers was to use the Langmuir–Blodgett (LB) deposition technique, leading to layers down to a few monolayers which can still exhibit a ferroelectric response similar to thin films and bulk materials. However, the polarization

switching times of LB layers are generally longer by orders of magnitude compared to thin films obtained from solution spin-coating, which prevents them from being used for practical memory applications.[87-89]

The situation started to change when one report was published in 2004 where the conductive polymer PEDOT:PSS (poly(3,4-ethylenedioxythiophene):poly(styrene sulfonic acid)) was added as an interfacial layer between the bottom electrode and P(VDF-TrFE), while inert gold was used as top electrode. By doing so, the P(VDF-TrFE) film could be reduced to 65 nm thickness while keeping the same ferroelectric response compared to thicker P(VDF-TrFE) films (*e.g.*, 210 nm). This results in a dramatic decrease of the operation voltage, down to less than 10 V.[9] In 2007, another report showed that the P(VDF-TrFE) layer thickness could be reduced to 50 nm with a ferroelectric response similar to bulk materials, by using another conductive polymer Ppy:PSS (polypyrrole-poly(styrene sulfonic acid)) sandwiched at the bottom and top interfaces between the metal electrodes and the P(VDF-TrFE) layer.[84] The reason why the P(VDF-TrFE) layer can be decreased to sub-100 nm with retained ferroelectric response using conductive polymers as interfacial layers lies in the fact that any chemical reaction or strong physisorption between the electrode and P(VDF-TrFE) is prevented. Aluminum was used as the electrode before these two reports[87, 88, 90, 91] and it interacts strongly with P(VDF-TrFE) forming nonferroelectric layers which reduce the ferroelectric response.[92, 93] Based on this observation, when using metal as electrode, inert metals like gold are preferred, resulting in an improved ferroelectric response of P(VDF-TrFE) thin-film capacitors.[94] In order to have ultra-thin films with retained ferroelectric response, another approach is to improve the film quality by selecting the proper solvents for P(VDF-TrFE) and controlling the spin-coating conditions (*e.g.*, humidity and temperature). It has been shown that films deposited at low humidity and at high temperature have improved quality.[95]

Another way to decrease the operation voltage of ferroelectric capacitors is to decrease the coercive field of P(VDF-TrFE). This can be done by crystallizing P(VDF-TrFE) in a confined state, *e.g.*, in nanocavities of a nanoimprint mold, which results in preferential crystal orientation, thus enhanced coupling with the applied electric field.[57, 58, 96-98] These confined P(VDF-TrFE) nano-arrays are also suitable for high density memory applications (in theory, as high as 75 Gbits per inch^2). However, they face a technological problem, which is that depositing the top electrode is challenging since insulation is needed in the openings between the nanoimprinted P(VDF-TrFE) features. Insulation of microscale-imprinted P(VDF-TrFE) was reported recently, but remains an issue for nanoscale-imprinted P(VDF-TrFE).[99] In addition, the information read-out could also be a problem since the charge displacement response (current during switching, I) scales with the remnant polarization P_r, capacitor surface area A_s, and switching time t ($I = (P_r A_s)/t$), the reading of which could be difficult for nanoimprinted P(VDF-TrFE) with a very small surface area.

Another issue which needs to be considered for ferroelectric capacitors is their endurance. One report studied this in details and showed that a ferroelectric capacitor could loose its ferroelectric response after a given number of cycles of switching (*e.g.*, 10^4), a phenomenon called polarization fatigue. This is due to the delamination of the electrode and the phase degradation of the P(VDF-TrFE), induced by the high internal electric fields that occur when the polarization is switched. By carefully selecting the operation conditions, these problems could be avoided or significantly reduced, and fatigue-free ferroelectric capacitors have thus been reported.[100]

It is worth noting that the accumulated knowledge on ferroelectric capacitors and the improvements of P(VDF-TrFE) film quality and ferroelectric properties can be (partially) transferred to other ferroelectric memory devices which will be discussed in the following sections.

2.2.2 Ferroelectric Diodes

Ferroelectric diodes have the same simple device structure as ferroelectric capacitors with the active layer sandwiched between two electrodes, except that the ferroelectric layer is replaced by a blend layer consisting of a random tiling of ferroelectric and semiconducting regions. This difference however results in completely different working principles of ferroelectric diodes. The first organic ferroelectric diode memory device was demonstrated by Asadi *et al.* in 2008,[11] of which the device structure and initially-proposed working mechanism are shown in Fig. 2.2.2. In this case, a blend layer consisting of p-type semiconducting P3HT (poly-3-hexyl thiophene) and ferroelectric P(VDF-TrFE) was used. The authors have proposed that the upwards polarization of P(VDF-TrFE) induces band bending in the semiconductor and enhances the charge injection at the electrode/semiconductor interface. This results in a lower resistance and a higher current flowing through the semiconductor component sandwiched between the two electrodes. Therefore, the working principle of ferroelectric diodes could be described like this: the writing and storage of the information is realized by applying a sufficiently large electric field to pole the P(VDF-TrFE), the polarization field of which modulates the injection barrier at the semiconductor contact. The read-out of the stored information is done by applying a small reading voltage and detecting the current response through the semiconducting component, whose value depends on the polarization state of the nearby P(VDF-TrFE) regions. This small reading voltage does not change the polarization state of P(VDF-TrFE) and results in the nondestructive read-out of the information.

After that, efforts concentrated on a deeper understanding of the working mechanism[101, 102] and on the optimization of device fabrication process and memory performances[103, 104]. Notably, our group reported a methodology to design low-power high-density ferroelectric diode memories on the nanoscale by employing nanoimprint lithography to shape P(VDF-TrFE) into highly ordered nanodots arrays. In addition to this well controlled morphology, the

coercive field of P(VDF-TrFE) was also reduced, resulting in low operation voltages.[105]

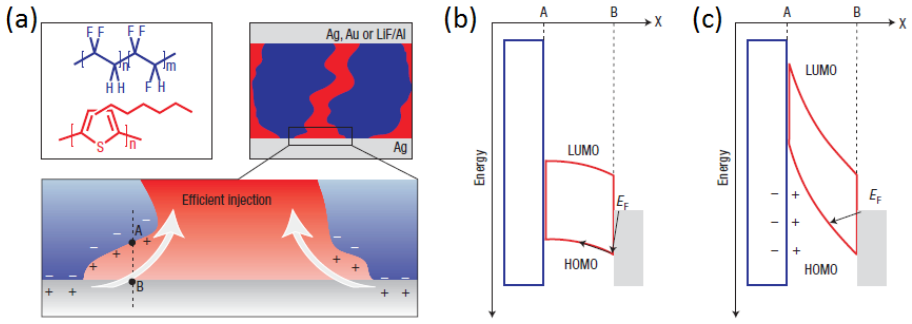

Figure 2.2.2: (a) Schematic cross-section of a diode based on a blend layer of semiconducting P3HT and ferroelectric P(VDF-TrFE) polymers. (b) Band diagram of an unpoled diode along the cross section AB. (c) Band diagram of a poled diode along the cross section AB. Poling of the ferroelectric material yields opposite compensating charges at the ferroelectric/semiconductor interface and induces band bending in the semiconductor, leading to enhanced charge injection. Adapted from[11]

Except for the non-destructive read-out, the ferroelectric diode also benefits from the structure being simple, and from the crosstalk problem being avoided by itself. Like ferroelectric capacitors, ferroelectric diodes can be fabricated in a crossbar structure with the active layer sandwiched between top rows and bottom columns of electrodes, which makes them easily fabricated. However, arrays with a row-column structure exhibit crosstalk in traditional memory devices based on resistive switches, in which case a rectifying diode has to be added in each discrete memory element to circumvent the crosstalk, unless the active layer is patterned.[106, 107] Arrays consisting of ferroelectric diodes can avoid this problem, because they intrinsically integrate a diode element in the memory structure, so that the information stored in each individual ferroelectric diode can be programmed and read out nondestructively.[108] Based on this, the concept of MEMOLED was later on demonstrated, using a light-emitting polymer as semiconducting component. MEMOLED's

can be used in passive matrix light emitting diode (LED) displays, which can solve issues such as high power consumption and crosstalk as normally exist in passive matrix LED displays.[109-111] With all these advantages, ferroelectric diode memories are considered to be one type of the most promising organic memory devices.

2.2.3 Ferroelectric Field-Effect Transistors

Another type of promising organic memory device is the ferroelectric field-effect transistor (FeFET), whose typical structure is shown at the bottom-left of Fig. 2.2.3, involving source, drain and gate electrodes, a semiconducting layer (*e.g.*, p-type PTAA), and a ferroelectric layer (P(VDF-TrFE)). Fig. 2.2.3 shows the typical transfer curve of a FeFET which exhibits a clear current hysteresis. The two stable polarization states of P(VDF-TrFE) corresponding to two current values at 0 gate bias are also shown in Fig. 2.2.3. In FeFET memories, the information (bits 1 and 0) is stored as the two stable states of a P(VDF-TrFE) film (respectively, an upwards polarization state and a depolarized state, as shown in the right part of Fig. 2.2.3), obtained by applying a sufficiently high gate voltage of proper sign (*e.g.*, -20 V and 20 V) on the gate electrode while grounding source and drain electrodes. The read-out of the stored information is realized by applying a small source-drain voltage (*e.g.*, -5 V) and detecting the source-drain current through the semiconducting layer; this current is modulated by the polarization state of the P(VDF-TrFE) layer. Depending on the polarization state, a higher or a lower current value is obtained at 0 gate bias which can be associated with bit 1 or 0. This small source-drain voltage does not change the polarization state, thus the information read-out is non-destructive.

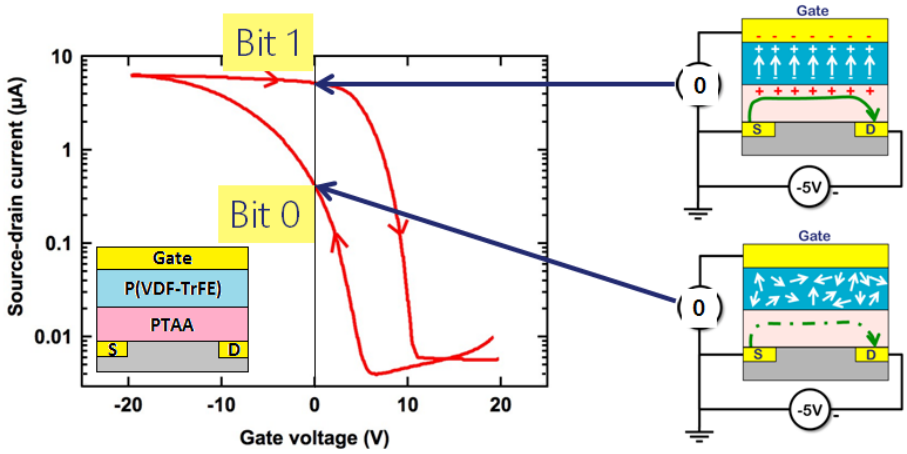

Figure2.2.3: Typical transfer curve of a top-gate bottom-contact organic FeFET consisting of three electrode terminals (source, drain, and gate), one ferroelectric/dielectric layer (P(VDF-TrFE)), and one organic semiconducting layer (PTAA). The polarization states of P(VDF-TrFE) corresponding to different current values at 0 gate bias are shown in the right of the figure.

Since the demonstration of the high-performance of an all-organic FeFET memory by Naber *et al.* in 2005,[10] the interest on this type of memories has promoted intensive studies on device working principles, performance optimization, and device integration, resulting in the fast increase of the number of research publications and practical applications.[10, 12-16, 18-21, 112-115] However, the complete understanding of the working mechanism of FeFET devices, especially the local polarization and depolarization of the P(VDF-TrFE) layer in FeFETs, still remains elusive, due to the complexity of the device structure. Therefore, there are still possible hidden parameters governing the operation of FeFET memories. In addition, there are always possibilities to improve the memory performance and to design new device configurations driven by scientific and technological innovations. Motivated by those, the majority of the practical work in this thesis will contribute to these issues. As a consequence, we do not discuss details about organic

FeFETs here, which will be presented together with the practical work in the following chapters for better understanding.

2.2.4 Multiferroics

Recently, research on multiferroics became a hot topic due to their potentially considerable scientific and practical importance.[116] Since the first demonstration of a four-state resistive memory element in a tunnel junction with multiferroic barriers in 2007,[117] it is believed that multiferroics might hold the future for ultimate memory devices.[118] As shown in Fig. 2.2.4, multiferroics are materials exhibiting the coexistence of different ferroic orders, such as ferroelasticity and ferroelectricity, ferromagnetism and ferroelectricity, or ferroelasticity and ferromagnetism, resulting in piezoelectric, magnetoelectric and magnetic shape memory effects, respectively.[37] Among these materials, magnetoelectric (ME) composites are the most interesting ones, because they display a generally larger coupling effect between the magnetic and electric ferroic orders compared to intrinsic magnetoelectric materials such as perovskites containing magnetic atoms, which is of great interest for both fundamental research and technological applications.[116] In these composites, the magnetism can be manipulated by an electric field, through the mediation of strains and stresses originating from piezoelectricity, which provides an additional degree of freedom to control the magnetic properties of a material, and vice versa. In short, the application of a magnetic field induces a deformation of the magnetic component by magnetostriction, which results in a change of electric polarization due to piezoelectricity. Conversely, the application of an electric field results in the deformation of the piezoelectric material by the converse piezoelectric effect, and in a variation of magnetization of the ferromagnetic material by the converse magnetostrictive effect. This coupling also provides multi-magnetic or electric polarization states which form the basis of these materials being used as components for memory devices.

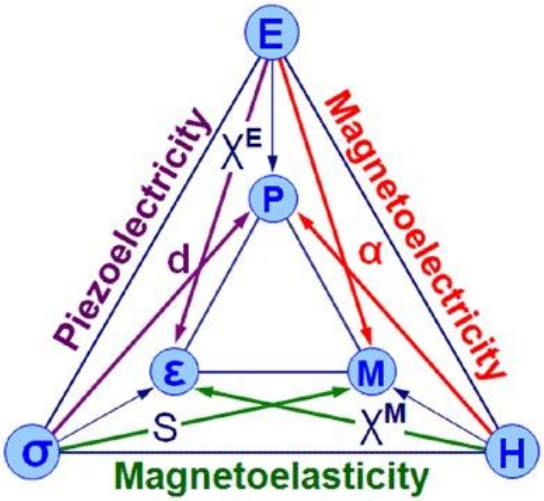

Figure 2.2.4: Schematic representation of different ferroic properties and their multiferroic couplings. Adapted from[119]

When reviewing the literature, however, almost all researches on multiferroics are based on inorganic materials,[117, 120-136] and there is not thorough study of local ME effects in multiferroics based on organic materials, which would be useful to fit the increasing demand of organic electronic applications. Therefore, in the last part of this thesis, we propose a first exploration of organic-based multiferroics, including a new method of sample preparation and the local characterization of ME coupling.

2.3 Nanoimprint Lithography

Nanoimprint lithography (NIL), also referred to as hot embossing or nano-embossing, is a nano-lithography method to pattern soft materials by using a rigid master mold with desired nanometer-range features.[137-139] NIL replicates by mechanical deformation a relief pattern (possibly down to sub-10 nm ultrahigh resolution) of the rigid mold in a heated thermoplastic or in a thermosetting polymer, unlike conventional photo- and electron beam lithography for which the

chemical structure of the resist is modified by photo- or electron irradiation. Its main advantages include high throughput, high-resolution, and cost-effectiveness.[137-143] It can be used at large scales, which is particularly interesting for practical applications, *e.g.*, when fabricating nanoimprinted organic electronic devices. In addition, conventional photo- and electron beam lithography techniques expose the resist to radiations and corrosive etchants during the pattern transfer process, which could be critical for sensitive organic functional materials. This is exactly the case for P(VDF-TrFE) used in this thesis, which might loose its ferroelectric properties if directly processed with conventional lithography techniques. NIL can avoid this problem by patterning directly the P(VDF-TrFE) by embossing.

NIL molds are commonly made of rigid materials such as silicon, silicon dioxide, and nickel, with a high strength and durability, and should be compatible with the fabrication process. NIL molds are prepared by another lithography techniques, *e.g.*, photolithography for microscale features, electron beam or interference lithography for nano-features. The molds are coated by an anti-sticking agent, in our case a perfluoroalkylsilane.

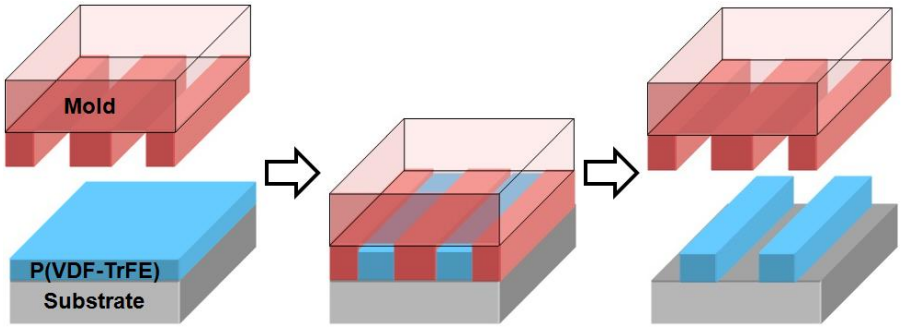

Figure 2.3.1: Schematic description of the NIL process, taking P(VDF-TrFE) as an example for the soft resist.

The general working principle of NIL is shown in Fig. 2.3.1, taking P(VDF-TrFE) as an example for the resist which is indeed used

in this thesis. First, a thin P(VDF-TrFE) layer of desired thickness is spin-coated on a substrate from a proper solution, and a hard mold with nano-protrusions is placed on top of the P(VDF-TrFE) film. Then the mold is pressed into the film at a certain temperature and pressure (135 ℃ and 60 bar for P(VDF-TrFE)). The selected imprinting temperature is in-between the Curie point and the melting point of P(VDF-TrFE) in order to imprint in the soft liquid crystalline paraelectric phase. This condition is kept for 10 min in order to allow P(VDF-TrFE) to flow and reorganize in the nanotrenches. After that, the system is cooled to a lower temperature (60 ℃) and the P(VDF-TrFE) is solidified during cooling. After removing the mold, the nano-features of the protruding mold are transferred to the soft P(VDF-TrFE) polymer. Fig. 2.3.2 shows atomic force microscopy (AFM) images of a typical nanoimprinted P(VDF-TrFE) sample. Well defined nano-line features are clearly seen, proving the excellent feasibility of NIL.

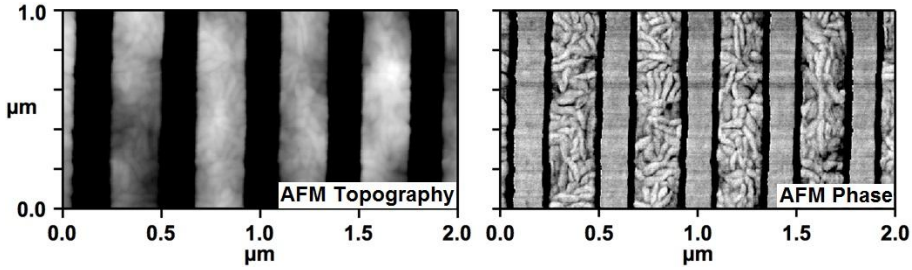

Figure 2.3.2: AFM topography (left) and phase (right) images of a nanoimprinted P(VDF-TrFE) sample, showing well defined nano-line features. In this case, the width and the height of the line structure are both *ca.* 200 nm.

In order to obtain high quality nanoimprinted features on soft resists/polymers (*e.g.*, P(VDF-TrFE)), a series of parameters need to be well controlled. These parameters include the confinement of the imprint, the configuration and the geometry of the mold, the adhesion at the polymer/mold and polymer/substrate interfaces. In this thesis, we made nanoimprint on P(VDF-TrFE) thin films, and all the above

mentioned parameters were adapted in order to have nanopatterned P(VDF-TrFE) on large scales for device fabrication. These experiments and conclusions are presented in Appendix A1.

In addition to the production of unique well-controlled nanostructures, NIL can also improve the functional properties of (semi-)crystalline polymer materials because a preferential crystal orientation can be achieved during the crystallization process in the cooling stage of the nanoimprinting process. Our group then others have reported that NIL can be used to control the microstructure and crystal setting of semi-crystalline P(VDF-TrFE), due to graphoepitaxy, resulting in improved ferroelectric properties, *e.g.*, decreased coercive fields.[57, 58, 96-98] This gives access to highly ordered ferroelectric polymer arrays with potential applications in low-voltage high-density non-volatile memory devices. NIL has also been used for producing nanowires and improving the functional properties of liquid crystalline light emitting and semiconducting polymers, resulting in improved device performance.[144] All these reports prove the versatility and wide applicability of NIL and its potential use with functional polymers.

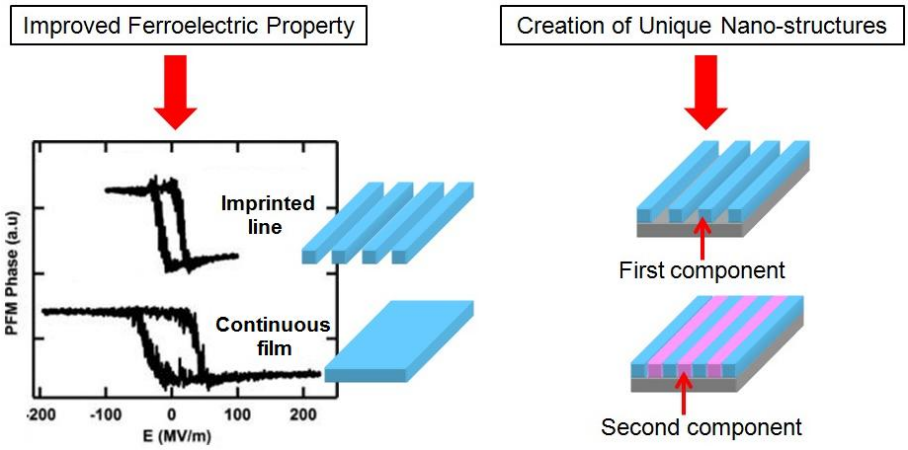

Figure 2.3.3: Two beneficial effects of using NIL to shape P(VDF-TrFE). One is that nanoimprinted P(VDF-TrFE) has decreased coercive field (left, improved ferroelectric property). The other one is that NIL creates unique P(VDF-TrFE) nanostructures, *e.g.*, well aligned nanowires, which in turn allows us to fabricate well-controlled hybrid multifunctional layers by filling

a second functional component in the trenches of nanoimprinted P(VDF-TrFE).

In this thesis, we make use of NIL to shape ferroelectric P(VDF-TrFE), which is integrated in the fabrication of ferroelectric memory devices and multiferroic layers. It should be again emphasized that there are two beneficial effects using this method in our case, as summarized in Fig. 2.3.3. The first one is that the nanoimprinted P(VDF-TrFE) has decreased coercive field due to the preferential crystal orientation, as mentioned above, at least when crystallization occurs in nano-cavities. This means that less voltage is required to switch the polarization of P(VDF-TrFE), which is an essential operation of ferroelectric memory devices. Therefore, nanoimprinted P(VDF-TrFE) has the potential to be used in memory devices of lower operating voltage, which is explored further in Chapters 4 and 5. However, it is worth noting that the coercive field should not be unlimitedly decreased in order to retain the stable polarization states of P(VDF-TrFE); otherwise, the polarization could be easily altered by small voltages and become unstable. The other beneficial effect is related to the creation of unique P(VDF-TrFE) nanostructures by NIL, separated by an open gap of controlled size, in which case a second functional component (*e.g.,* semiconducting polymers and ferromagnetic metals) can be added in these openings. This leads to the production of well controlled multifunctional hybrid layers, allowing us to study the coupling of two functional properties at the nanometer scale and to design new device configurations using these multifunctional hybrid layers. This approach is attempted in Chapters 5 and 6 where we have made ferroelectric/semiconducting nanowire hybrid layers and nanopatterned ferroelectric/ferromagnetic multiferroic layers.

2.4 Scanning Probe Microscopy

Scanning probe microscopy (SPM) is a family of tools that are used to obtain images of nanoscale surfaces and structures using a physical probe to scan the surface of a sample. SPM was created in 1981, with the invention of the scanning tunneling microscopy (STM) [145, 146] by G. Binnig and H. Rohrer who won the 1986 Nobel Prize in Physics for this invention[147]. STM measures the tunneling current through the vacuum between a biased tip and the surface of the sample, which depends on the tip position, the applied voltage, and the local density of states of the sample. Then information is acquired by monitoring the current as the tip position scans across the surface, from which images can be extracted. Since then, it becomes possible to see individual atoms distinctly, and to arrange the atoms the way we want. However, STM can only be used to study conductive samples, and the experiment is generally performed in vacuum. To overcome these limitations, atomic force microscopy (AFM) was invented by G. Binnig in 1986,[148] in which, the information is acquired by detecting the tip deflection resulting from the tip-sample interaction. Based on different tip-sample interactions, a series of modified AFM techniques were developed, such as piezoresponse force microscopy (PFM) detecting the electromechanical interaction, Kelvin probe force microscopy (KPFM) detecting the electrical interaction, and magnetic force microscopy (MFM) detecting the magnetic interaction, to name a few. In this thesis, AFM and PFM are used to characterize the topography and the ferroelectric properties of the samples, respectively.

2.4.1 Atomic Force Microscopy

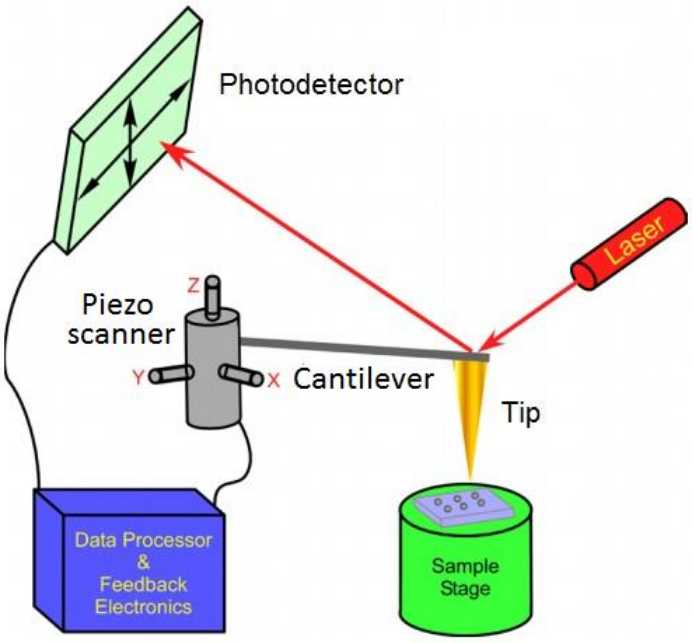

Figure 2.4.1: Schematic drawing of an AFM equipment. Adapted from[149]

As mentioned above, AFM is one application type of SPM and it has demonstrated atomic resolution. As shown in Fig. 2.4.1, an AFM equipment contains four main components: the probe (cantilever + tip), the piezo scanner, the deflection-detecting system (laser beam + photodetector), and the data processor and feedback electronics. The basic operation of AFM starts by bringing a sharp probe into close proximity with the sample surface, resulting in a deflection of the cantilever which can be detected by the detection system. Probe and sample are then moved relative to each other in a raster pattern controlled by the piezo scanner and the electronics, and an image representing a certain property of the sample is formed (measured in a serial fashion at discreet locations (pixels)) by analyzing the cantilever deflection during the probe motion.

As shown in the force-distance curve (Fig. 2.4.2), when the tip is brought close to the sample surface, tip-surface interactions occur, in which the van der Waals attractive force typically dominates at the beginning, resulting in an overall attractive interaction between the tip and the surface. This attractive force increases until the electron clouds of atoms in the tip and the sample begin to interact and electrostatically repel each other. This repulsive force weakens the overall attraction until a net force of zero is reached. Starting from this point, the tip is considered to be in "contact" with the sample surface. Depending on these interactions and the force-distance curve shown in Fig. 2.4.2, AFM has three basic operation modes: contact mode, non-contact mode, and tapping mode (intermittent mode).

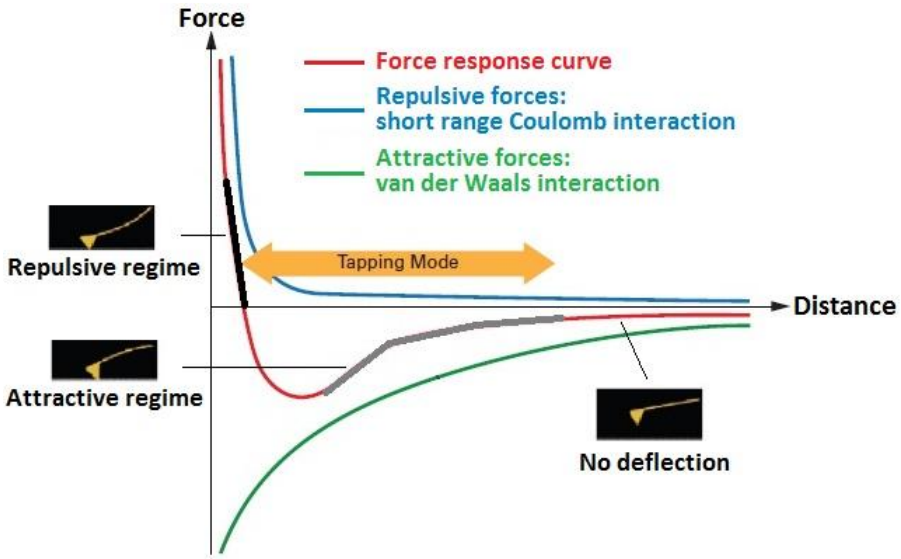

Figure 2.4.2: Force-distance curve between the tip and the sample surface. Adapted from[150]

In contact mode, operation is in the repulsive regime and the tip makes physical contact with the sample surface. The cantilever deflects to accommodate topography below the probe while a user-defined deflection (*i.e.*, a constant contact force) is maintained by moving the probe or the sample using the Z-piezoelectric actuator. This Z-piezo movement at each pixel location generates a height profile image of the surface. However, a limitation of contact mode is

that the constant contact with the surface can damage both the sample (especially soft samples) and the probe due to the lateral friction force during the scanning. Although there are limitations, contact mode is a pre-requirement for some modified AFM techniques (*e.g.*, PFM) where the probe must be brought into physical contact with the sample surface in order to measure specific properties of functional materials (*e.g.*, the electromechanical coupling of ferroelectric materials).

In non-contact mode, the probe does not contact the sample surface, but oscillates above the surface. The surface topography can be measured by monitoring the changes in the oscillating phase or amplitude due to the attractive van der Waals forces. Non-contact mode AFM does not suffer from tip and/or sample degradations that are sometimes observed with contact AFM, which makes non-contact AFM preferable to contact AFM for measuring soft samples, *e.g.*, biological samples and organic thin films. However, non-contact AFM has generally a lower resolution and the probe oscillation is sensitive to contaminations on the sample surface.

In tapping mode, the cantilever is oscillated close to its resonance frequency as the probe is scanned across the surface. The amplitude set point of the oscillation is typically 10-100 nm, and the probe lightly "taps" the surface during scanning, contacting the surface at the bottom of its swing. As the probe interacts with topographic features, the oscillation amplitude changes and the feedback loop moves the tip or the sample up or down to maintain the amplitude set point. Since tapping mode combines the advantages of high resolution with contact mode and non-destructive characterization with non-contact mode, it is implemented in this thesis to characterize the topography and the microstructure of the sample. A typical example of topographic AFM image has been shown in Fig. 2.3.2 of Section 2.3.

2.4.2 Piezoresponse Force Microscopy

Piezoresponse force microscopy (PFM) is a specific application of AFM where a conductive tip is used to detect the electromechanical

coupling of ferroelectric/piezoelectric materials by applying an ac voltage.[151, 152]

PFM Principles

Piezoelectricity is defined as a phenomenon where the application of the pressure or stress on ferroelectric/piezoelectric materials leads to the buildup of electrical surface charges or polarization. The inverse of this phenomenon is called the converse piezoelectric effect, meaning that the application of an electrical field results in a deformation of the material. PFM makes use of the principle of this converse piezoelectric effect and measures the mechanical response of ferroelectric/piezoelectric materials when a periodic electrical field is applied to the material.

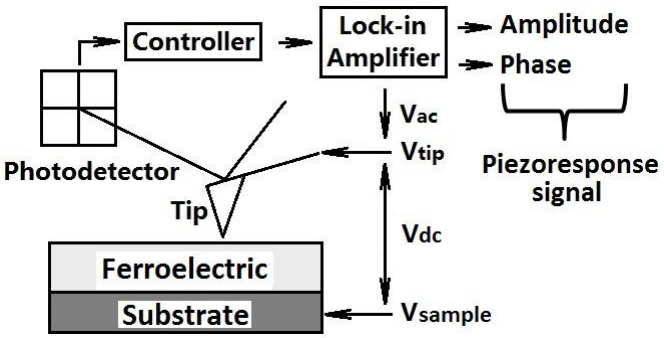

Figure 2.4.3: Schematic drawing of a typical PFM setup where the ac voltage is applied to the tip.

A typical PFM setup is shown in Fig. 2.4.3 where a periodic ac voltage is applied to the tip which is in contact with the sample surface. Then the tip voltage V_{tip} is:

$$V_{tip} = V_{dc} + V_{ac}\,cos(\omega t) \qquad \text{(Equation 2.4.1)}$$

with V_{dc} the dc voltage applied to the tip (polarization switching voltage), V_{ac} the ac voltage (probing voltage), and ω the angular

frequency of the ac voltage (driving frequency). When the ferroelectric/piezoelectric material contracts or expands in response to the external electrical field due to the converse piezoelectric effect, the AFM cantilever, which is in contact with the sample, deflects simultaneously (Fig. 2.4.4). The deflection is monitored by means of a deflection-detecting system (laser beam + photodetector) as described in Section 2.4.1, with the first harmonic component of the deflection signal detected by a lock-in amplifier (Fig. 2.4.3). Then this information is translated into a piezoresponse signal, *i.e.*, PFM amplitude response A and PFM phase response φ which, using the harmonic oscillator model,[153] can be quantified as:

$$A(\omega) = \frac{A_{max}\omega_0^2/Q}{\sqrt{(\omega_0^2 - \omega^2) + (\frac{\omega_o \omega}{Q})^2}} \qquad \text{(Equation 2.4.2)}$$

$$\tan\varphi(\omega) = \frac{\omega_o \omega}{Q(\omega_0^2 - \omega^2)} \qquad \text{(Equation 2.4.3)}$$

where A_{max} is the amplitude at the resonance angular frequency ω_o, and Q is a quality factor that describes the energy loss in the system. Of note, these two equations are general to all AFM setups and are not limited only to PFM. These two equations also indicate mathematically that the piezoresponse signal could be enhanced when working at a frequency close to the contact resonance. The PFM amplitude provides information about the local electromechanical coupling (converse piezoelectric coefficient) and the PFM phase provides information about the polarization direction (dipole orientation) below the tip.

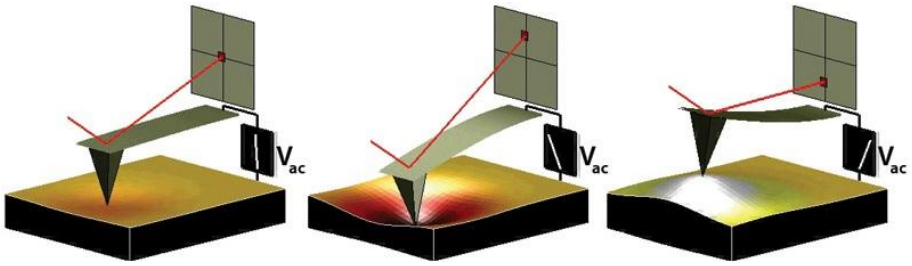

Figure 2.4.4: Schematic description of PFM operation. (Left) No voltage is applied, resulting in no electromechanical coupling. (Middle and right) The contraction and expansion of the ferroelectric material in response to the external electrical field result in a cantilever deflection which can be measured and interpreted in terms of the piezoelectric properties of the sample. Adapted from[154]

PFM Operation Mode

There are two basic modes in PFM: imaging mode and spectroscopy mode. Depending on the purpose of the investigation on ferroelectric/piezoelectric materials, the proper mode should be selected.

In PFM imaging mode, the conductive tip is scanned over a defined area, while the topography, PFM amplitude, and PFM phase images in both vertical and lateral directions (called vertical PFM and lateral PFM) can be obtained simultaneously by applying an ac voltage on the tip, which excites the electromechanical coupling in the ferroelectric material. Apart from getting images, this mode can also be used to pole the ferroelectric material over the scanned area by applying a sufficient dc voltage (larger than the coercive field of the ferroelectric material). Fig. 2.4.5 shows a typical example of PFM amplitude image and phase image obtained with a 100 nm-thick continuous P(VDF-TrFE) thin film sample. A strong contrast appears in both images between poled and unpoled regions, indicating that the dipoles are aligned along the direction of the poling field. The direction of dipole moments or polarization of P(VDF-TrFE) in different regions is shown in Figure 2.4.5 (c). In this thesis, PFM

imaging mode was employed to study the local polarization and depolarization as well as the switching mechanism of P(VDF-TrFE) continuous layers and nanowires in complex electronic devices, *e.g.*, in ferroelectric field-effect transistors (Chapters 3-5).

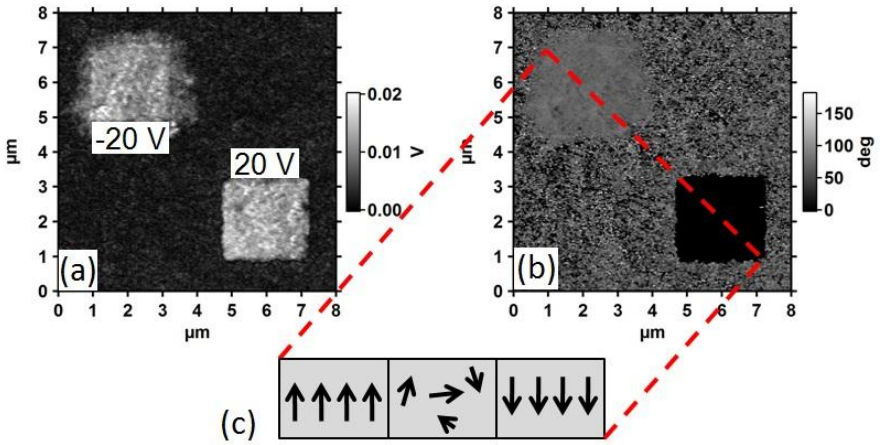

Figure 2.4.5: Typical PFM (a) amplitude and (b) phase images of a 100 nm-thick P(VDF-TrFE) film deposited on a conductive doped Si substrate. Two small regions (2 µm x 2 µm) were poled by applying a 20 V or -20 V dc voltage on the PFM tip before taking the images (8 µm x 8 µm). The direction of dipole moments or polarization in different regions is shown in panel (c).

In PFM spectroscopy mode, the tip is fixed at a specific position on the sample and the experiments are performed by sweeping the dc voltage in a cyclic manner. In general, hysteresis loops are obtained from these experiments for ferroelectric materials due to the dependence of the local piezoelectric vibration on applied voltage.[155] Measurements of local hysteresis loops in PFM spectroscopy mode are of great importance because they enable to quantify ferroelectric response and polarization switching on a selected small area of only a few tens of nanometers. Fig. 2.4.6 shows a typical example of PFM spectroscopy graph (phase and amplitude as a function of applied dc voltage) obtained with a 200 nm-thick continuous P(VDF-TrFE) thin film on an Au substrate. Clear PFM phase hysteresis loop and

butterfly-shaped amplitude curve are observed, indicating the ferroelectric nature of P(VDF-TrFE). Of note, the curves are off-centred, most probably due to the difference of work function of the bottom and top electrodes, and/or the existence of other electrostatic couplings in the PFM equipment. In this thesis, the PFM spectroscopy mode was employed to characterize the local ferroelectric response of P(VDF-TrFE) in multiferroic layers (Chapter 6).

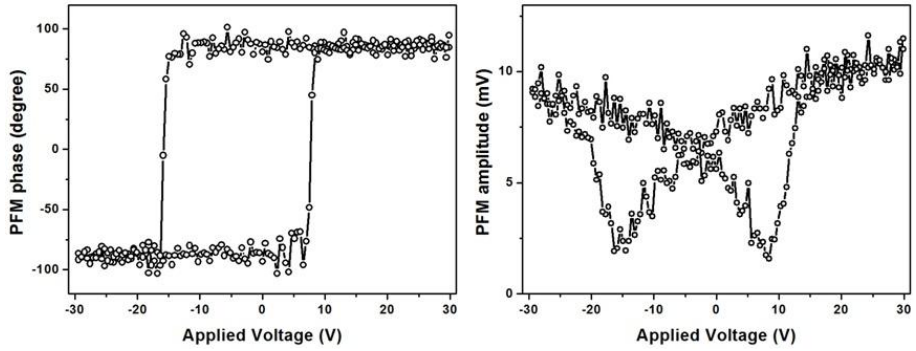

Figure 2.4.6: PFM phase (left) and PFM amplitude (right) as a function of the applied bias on a 340 nm thick P(VDF-TrFE) film using Au as bottom electrode and PFM tip (Pt/Ir coated) as top electrode.

Optimization of PFM operation conditions

In practice, the operation of PFM experiments is more complex than in theory because it is also governed by many parameters which need to be optimized for specific materials, devices, and equipments. Taking P(VDF-TrFE) as an example, it has been shown in our group and by others[156] that the magnitude of the ac driving bias should be in the range of 0.5-2.5 V and that the driving frequency should be close to the contact resonance in order to amplify the piezoresponse signal (Eq. 2.4.2 and Eq. 2.4.3). However, working at close-to-contact resonance frequency could be challenging in some cases because the contact resonance frequency is not stable especially during scanning a rough surface, and it can also be altered by external noise (*e.g.*, a

magnetic field). In this case, working at frequencies far away from the contact resonance and increasing slightly the driving bias would be a better choice. In order to fully eliminate this problem, two more advanced methods were proposed: the band excitation method[157] and the dual-frequency resonance-tracking method[158]. We will not discuss these two advanced methods here, since the PFM setups we used in this thesis are not equipped with them. In addition, the tip scanning speed and the poling time also influence the PFM contrast and polarization switching.[159] Apart from the above mentioned parameters, there are even more factors governing the PFM acquisition results, such as the nature of the conductive tip, the type of bottom electrode, and the selection of PFM operation mode. In Appendix A2, we have tried to explore the influence of some of these parameters on the piezoresponse signal acquisition and the ferroelectric property quantification.

2.5 Other techniques

In addition to using NIL and PFM as two main techniques, some other techniques were also employed in this thesis. For sample preparations, standard photolithography technique was used to align the source and drain electrodes in transistors. An e-gun evaporator was used to deposit metal layers or electrodes. Electrochemical deposition was used to grow metals (nickel and platinum) in the openings of nanoimprinted P(VDF-TrFE) templates from proper electrolytes. For sample characterizations, scanning electron microscopy was used to characterize the morphology of the multiferroic layers. A profilometer and an ellipsometer were used in parallel with AFM to measure the thickness of thin layers. A probe station or PFM equipped with a semiconductor analyzer were used to measure the current characteristics of the transistors. Details are given in the related chapters when presenting our practical work.

Chapter 3

Local Maps of the Polarization and Depolarization in Organic Ferroelectric Field-Effect Transistors

Abstract. In this chapter, we study the local ferroelectric polarization and depolarization of poly(vinylidene fluoride-*co*-trifluoroethylene) (P(VDF-TrFE)) in p-type ferroelectric field-effect transistors (FeFETs). Piezoresponse force microscopy (PFM) is used to obtain local maps of the polarization on model metal-semiconductor-ferroelectric stacks, and on FeFETs stripped from their top-gate electrode; transfer curves are measured on complete FeFETs. The influence of the semiconductor layer thickness and of the polarity and amplitude of the poling voltage are investigated. In accumulation, the stable "on" state consists of a uniform upward-polarized ferroelectric layer, with compensation holes accumulating at the ferroelectric/semiconducting interface. In depletion, the stable "off" state consists of a depolarized region in the center of the transistor channel, surrounded by partially downward-polarized regions over the source and drain electrodes and neighboring regions. The partial depolarization of these regions is due to the incomplete screening of polarization charges by the charges of the remote electrodes. Therefore, thinner semiconducting layers provide higher downward polarizations, which result in a more depleted transistor channel and a higher charge injection barrier between the electrodes and the semiconductor, leading to lower threshold voltages and higher on/off current values at zero gate bias. Clues for optimization of the devices are finally provided.[*]

[*] Results in this chapter were published in Scientific Reports 6, 22116 (2016).

3.1 Introduction

Since the first organic memory ferroelectric field-effect transistor (FeFET) was demonstrated by Naber *et al.* in 2005,[10] organic non-volatile memory FeFETs have become a promising and active topic, evidenced by increasing numbers of scientific publications and applications.[10, 12-16, 18, 19, 112-114] The structure of a typical FeFET is given in Fig. 3.1 (c). Here, we report for the first time on direct microscopic measurements of the spatial distribution of polarization in the ferroelectric layer of a real organic FeFET, and on the effect of the semiconducting thickness on the stability of the polarized states.

In organic FeFETs, poly(vinylidene fluoride-*co*-trifluoroethylene) (P(VDF-TrFE)) is the most often used ferroelectric material, due to its high remnant polarization, short switching time, and low processing temperature (typically 120-140 ℃).[93, 160] As the memory functionality of a FeFET uses different polarization states of the ferroelectrics to store information, the polarization and depolarization behavior of P(VDF-TrFE) has been studied in FeFETs under different conditions, *e.g.*, varying device configurations, changing poling conditions, and using different organic or inorganic semiconductors.[10, 12, 14, 16, 17, 20, 113, 161] A common conclusion from these previously-published studies is that, when the semiconductor is in the accumulation regime, the accumulation charges compensate the polarization charges of the ferroelectric layer in contact with the semiconductor (Fig. 3.1 (c)), thereby decreasing the electrostatic energy. After removing the poling voltage, the polarization remains stabilized by these mobile compensating accumulation charges, leading to high source-drain current values. Starting from this polarization state, depolarization only occurs when the gate bias exceeds the coercive voltage of P(VDF-TrFE).

In contrast, when the semiconductor is poled in the depleted state, different ferroelectric polarization behaviors have been reported and the details of the mechanism remain elusive. For instance, Naber *et al.* reported that the polarization switches between a stable polarized state and a depolarized state in metal-ferroelectric-semiconductor-metal

(MFS) devices with organic poly(3-hexylthiophene) (80 nm layer thickness) as semiconductor. These two states correspond to the accumulation and depletion regimes of the semiconductor, respectively, which means that the depleted semiconductor layer prevents the formation of a stable polarization state.[15] This was modeled later on by Brondijk *et al.* for a FeFET device.[17] On the other hand, Kam *et al.* showed a close-to-full polarization reversal in MFS diodes using a small molecular semiconductor pentacene (30 nm layer thickness), and proposed the existence of a stable polarization state when the semiconductor is depleted, but only below the source-drain electrode regions in a bottom-gate top-contact FeFET.[18] Most recently, Gelinck *et al.* reported a close-to-full polarization reversal in a dual-gate FeFET using 20 nm inorganic indium-gallium-zinc oxide as the semiconductor, but only under certain biasing conditions, i.e., by applying a second gate bias to introduce a second charge accumulation layer. These authors state that this second accumulation layer causes the redistribution of electric field lines, which can effectively decrease the depolarization field and leads to a stable polarization state.[20]

Since several polarization states are proposed in FeFET devices when the semiconductors are depleted, namely depolarized or partially polarized, it is difficult to have a complete understanding of the general rules which control polarization and depolarization in FeFETs. A complicating factor is that the polarization might depend on the semiconductor layer thickness: indeed, analysis of the literature suggests that, the thinner the used layer, the more probable it is to obtain a stable polarization state in the depleted regime, although different semiconductors are employed. A possible reason would be that thinner semiconductor layers screen less the charges of the source and drain electrodes, which can thus partially compensate the polarization charges of the ferroelectric material. Another possibility is that, since the depleted semiconductor acts like an insulator which shares the poling voltage with the ferroelectrics, larger poling voltages, compared to the one applied to obtain the stable polarization when the semiconductor is in accumulation, are needed to reach the coercive field of P(VDF-TrFE). In addition, the location of P(VDF-TrFE),

either over the source or drain regions, or over the channel region (Fig. 3.1 (c)), may also affect the polarization behavior. These hypotheses do not obey the common belief that, in order to obtain a stable polarization of the ferroelectric material, a poling field sufficiently large compared to the coercive field is needed, together with polarization-compensating mobile charges in direct contact with the ferroelectric layer.[162]

These uncertainties largely result from the fact that there is currently no direct imaging of the switching of the transistor from its stable polarization state to its depolarized state, and more specifically of how the poling voltage distributes over the channel and electrode regions. In order to progress in theses issues, we therefore study for the first time by piezoresponse force microscopy (PFM) the local polarization and/or depolarization behavior in metal-semiconductor-ferroelectric (MSF) devices and unipolar FeFETs, for different semiconductor thicknesses and poling conditions. Then we fabricate and characterize unipolar FeFET devices, and check the influence of the semiconductor thickness and of the poling conditions on the device performance. Our microscopic studies reveal the complexity of the polarization state in the FeFET structure when the semiconductor is depleted, from which the behavior of FeFET devices can be fully explained and therefore improved.

3.2 Experimental

Materials. P(VDF-TrFE) (65 wt% of VDF units and a weight-average molar mass of *ca.* 300 000 g/mol) was provided by Solvay Specialty Polymers. Poly(triarylamine) (PTAA, a p-type amorphous organic semiconductor) was purchased from Flexink. P(VDF-TrFE) was dissolved in acetylacetone (65 g/L). PTAA was dissolved in toluene (2, 5, and 10 g/L). All solutions were filtered through PTFE filters with 0.45 μm pore size before spin-coating.

Device Fabrication. MSF devices (Fig. 3.1 (a)) were fabricated on a Si/SiO_2 substrate covered by a 10/100 nm thick Cr/Au layer. PTAA layers of 5-45 nm thickness were spin-coated from solutions of different concentration using various spin speeds. On top of the PTAA layers, *ca.* 200 nm of P(VDF-TrFE) was spin-coated (5000 rpm, 500 r/s, 1 min) from a 65 g/L P(VDF-TrFE) solution. We note that acetylacetone, used to dissolve P(VDF-TrFE), is an orthogonal solvent to the underlying PTAA layer. The resulting samples were annealed at 135 ℃ for 10 min in air to improve the crystallinity of P(VDF-TrFE). A conductive tip was used as the top electrode when characterizing the devices in a PFM setup. For FeFET devices (Fig. 3.1 (b)) and (c)), 5/30 nm thick Cr/Au source-drain electrodes were defined by standard photolithography on a Si (100) substrate covered by 200 nm of thermal SiO_2. On this substrate, 10-45 nm thick PTAA layers were spin-coated from PTAA solutions of different concentration using various spin speeds. On top of the PTAA layers, *ca.* 340 nm of P(VDF-TrFE) was spin-coated (2000 rpm, 500 r/s, 1 min) from a 65 g/L P(VDF-TrFE) solution. The resulting samples were annealed at 135 ℃ for 10 min in air. In the case of devices tested in PFM, a conductive tip was used as top electrode; in the case of devices for current characterization, 70 nm-thick Au top electrodes were evaporated through a shadow mask.

Device Characterization. The piezoresponse of the P(VDF-TrFE) films in MSF and FeFET devices was checked by PFM (Bruker Icon Dimension) in contact mode. The PFM technique allows to pole P(VDF-TrFE) and check the polarization on any desired position. To pole the device, a dc bias was applied to the conductive tip during scanning, while keeping the bottom electrodes grounded. An ac bias (1.5 V peak-to-peak amplitude) was then applied to the bottom electrodes to image the piezo/ferroelectric response, while keeping the tip grounded. The conductive Si tip was purchased from Nanosensors (Boron-doped diamond-coated, force constant of 0.02−0.77 N/m). The current characterization of the FeFET devices was performed in air by using an Agilent B1500A semiconductor device analyzer equipped with a probe station. To obtain the transfer curves of FeFETs, a -5 V

source-drain voltage was applied while sweeping the gate voltage from a positive value to a negative value, and to a positive value again. The devices were operated in the linear regime with these operation conditions.[163]

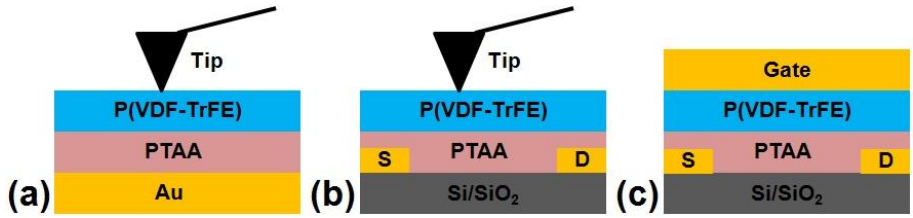

Figure 3.1: Schematic drawing of the device configurations used in this work. (a) A MSF sample using a mobile conductive tip as top electrode; (b) A top-gate bottom-contact FeFET using a mobile conductive tip as gate electrode; (c) A top-gate bottom-contact FeFET device used for current characterization.

3.3 Results and Discussion

3.3.1 PFM studies of Metal-Semiconductor-Ferroelectric devices

The polarization behavior of a P(VDF-TrFE) film of 200 nm thickness was first checked by PFM in MSF samples with a semiconducting PTAA layer of variable thickness (Fig. 3.1 (a)). Fig. 3.2 shows PFM amplitude images corresponding to samples with PTAA layer thicknesses of 0, 5, 15, 25 and 35 nm. In all images, two small regions (2 x 2 μm^2) were first poled by applying 30 V (left-bottom) or -30 V (right-top) to the conductive tip, while keeping the bottom electrode grounded. The PFM amplitude images were then obtained by scanning the tip on a larger area (6 x 6 μm^2) while applying only an ac bias to the bottom electrode (1.5 V peak-to-peak amplitude) while keeping the tip grounded. The contrasts of PFM amplitude between the positively- or negatively-poled regions and the unpoled background are plotted in Fig. 3.2 (f) as a function of PTAA layer thickness. The PFM amplitude contrast between poled and unpoled regions indicates that P(VDF-TrFE) is well-polarized and that the poled states are stable

since the images are taken at zero poling bias well after poling. In these PFM amplitude images, a larger contrast indicates that more dipoles are aligned, with as a consequence a larger remnant polarization.

When the bias applied to the tip (V_{tip}) is -30 V, the contrast is almost constant from 0 to 35 nm PTAA layer thickness, showing that the polarization behavior is hardly affected by the semiconducting layer (which is in accumulation state in this case); this is because the accumulation charges (holes) have been trapped at the interface and stabilize the ferroelectric polarization (Fig. 3.2 (h)). However, the polarization behavior is completely different when V_{tip} is 30 V, in which case the PTAA layer is depleted. The contrast then decreases with increasing PTAA layer thickness and vanishes for 35 nm PTAA layer thickness. This observation is in good agreement with a previous result showing that there is no contrast for 45 nm PTAA layer thickness.[163] This decrease may *a priori* result from two different factors. First, the depleted PTAA layer acts like an insulator, which shares the poling bias with the P(VDF-TrFE) film; therefore, for a sufficiently thick PTAA layer, the electric field in the P(VDF-TrFE) layer might be too low to orient the dipoles during poling. Second, the PTAA layer increasingly screens the free electrons in the bottom metallic electrode, preventing them from fully compensating the polarization charges, resulting in depolarization after poling (Fig. 3.2 (h)).

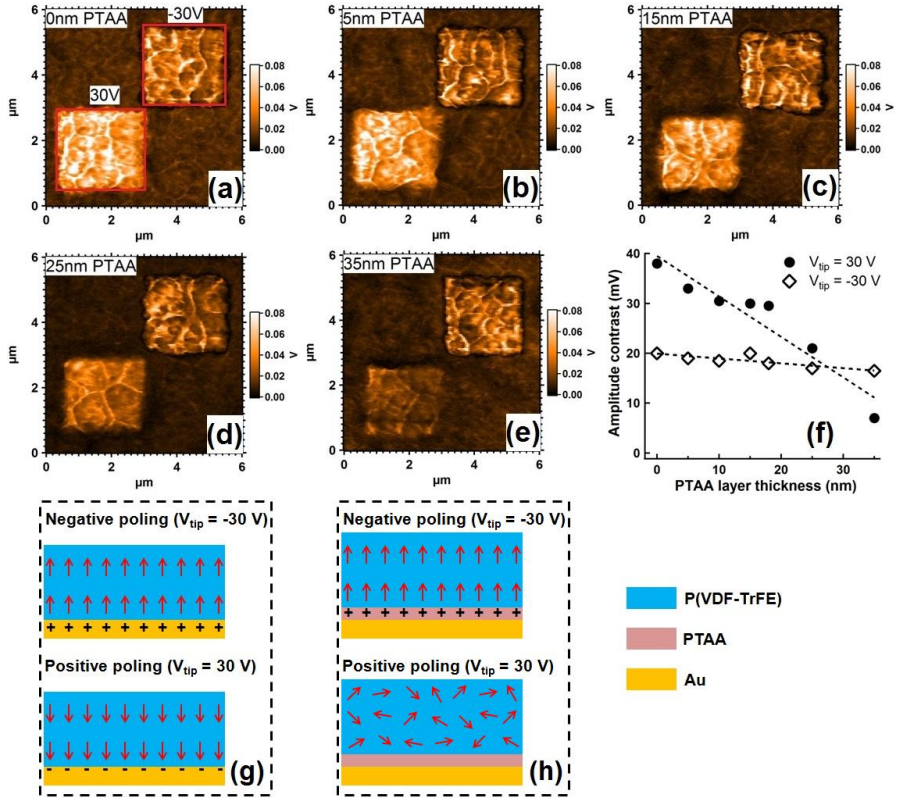

Figure 3.2: PFM amplitude images of MSF samples with a PTAA (S) layer thickness of (a) 0 nm, (b) 5 nm, (c) 15 nm, (d) 25 nm, and (e) 35 nm. On these samples, one small region (2 x 2 μm^2, left-bottom) was poled by applying a 30 V tip bias and the other one (2 x 2 μm^2, right top) a -30 V tip bias, while keeping the bottom electrode grounded. These two regions are boxed in red in (a). The PFM images were subsequently obtained at zero poling voltage over larger areas (6 x 6 μm^2). The PFM amplitude contrasts between these two small regions and the unpoled background are shown in (f). The contrast is calculated as the difference of the average amplitude of the poled region and the unpoled background. Dashed lines are guides to the eye. Schematic descriptions of the polarization state after removal of the poling voltage are shown in (g) and (h), for zero and 35 nm PTAA layer thickness.

It is possible to decide which effect is dominant in our case; indeed, the voltage over the ferroelectric layer is $V_F = VC_S/(C_S+C_F)$,

where V is the poling voltage, and C_F (resp. C_s) is the capacitance of the ferroelectric (resp. semiconducting) layer. Taking ε_F = 10 for the relative permittivity of the ferroelectric material and ε_S = 3 for the one of the depleted PTAA layer,[21, 51] the voltage over the 200 nm-thick ferroelectric layer when poling at 30 V decreases from 30 to 17.1 V when the PTAA layer thickness is increased from zero to 45 nm. This corresponds to an electric field from 150 to 64 MV/m, which is in all cases above the coercive field of our P(VDF-TrFE) layer (61.5 MV/m, see below). Therefore, the loss of polarization observed for the higher PTAA thickness does not result from incomplete poling of the ferroelectric, but from depolarization after poling due to the improper screening of the polarization charges by the too-distant free electrons of the metal. Nevertheless, a considerable polarization is still obtained when the PTAA layer is below *ca.* 20 nm, showing that two stable polarization states can be obtained in functional electronic devices if the semiconductor layer is thin enough not to screen fully the compensating charges of the metallic electrode.

3.3.2 PFM studies of FeFET devices

In FeFET devices, the PTAA and P(VDF-TrFE) stacked layers are not always sandwiched between two metallic electrodes (Fig. 3.1 (c)). Indeed, in the channel regions, the semiconducting/ferroelectric stack lies over an insulating region (SiO_2 in our case), which is significantly different from a MFS device. Therefore, we further checked by PFM the local polarization switching in a FeFET device, using the configuration shown in Fig. 3.1 (b), again with different PTAA layer thicknesses and poling polarities.

Fig. 3.3 (a-c) shows the PFM amplitude images of FeFETs with 0 nm (as a reference), 5 nm, and 25 nm PTAA layer, respectively. 40 V poling biases of opposite polarity were applied over two small regions before imaging, as indicated; P(VDF-TrFE) is polarized when there is a PFM amplitude contrast between a poled region and the background – in this context, it is important to note that the contrast may be

positive or negative, depending on the specific conditions on acquisition. Fig. 3.3 (a-c) shows that the polarization depends on location. The source-drain Au electrode regions and the SiO_2 channel regions, both of 2 μm width, are marked in Fig. 3.3 (a). Over the source and drain electrode regions, P(VDF-TrFE) is in a stable polarized state having a large contrast with the unpolarized background, irrespective of the polarity of the poling voltage and of whether a PTAA layer is or not present. This is consistent with the results obtained on MFS devices with thin PTAA layers.

However, the polarization behavior is different over the SiO_2 channel regions. In the case of the reference FeFET without a PTAA layer (Fig.3. 3 (a)), a significant portion of P(VDF-TrFE) is not polarized due to a dearth of compensation charges at the SiO_2/P(VDF-TrFE) interface, whatever the polarity. When a PTAA layer is added in the device (Fig. 3.3 (b-c)), the polarization over the channel regions now depends on the polarity of the poling voltage. For a negative bias (-40 V), the P(VDF-TrFE) can be polarized everywhere, since the PTAA layer is in accumulation, acting as an electrode during poling and providing the holes needed to stabilize the polarization after removal of the poling voltage. In contrast, when a positive bias (40 V) is applied, the central portion of the channel regions is not polarized, because the applied bias is not exceeding the coercive voltage of P(VDF-TrFE) in these regions.

Nevertheless, in the case of the positive poling voltage for all PTAA thicknesses, and for the negative poling voltage only for the reference device without PTAA, a narrow stripe of P(VDF-TrFE) resting over the insulating channel regions is also polarized over a width w in the vicinity of the source-drain electrode regions. This can be seen from the width of the polarized and unpolarized regions, compared to the width of the source-drain electrodes and of the channel (both equal to w_e = 2 μm): for instance, in Fig. 3.3 (b), the width of the poled regions is 3.04 μm while the width of the unpoled ones is 0.96 μm; hence, there is a stripe of width w=(3.04-2)/2=0.52

µm of poled P(VDF-TrFE) lying over both edges of the channel region.

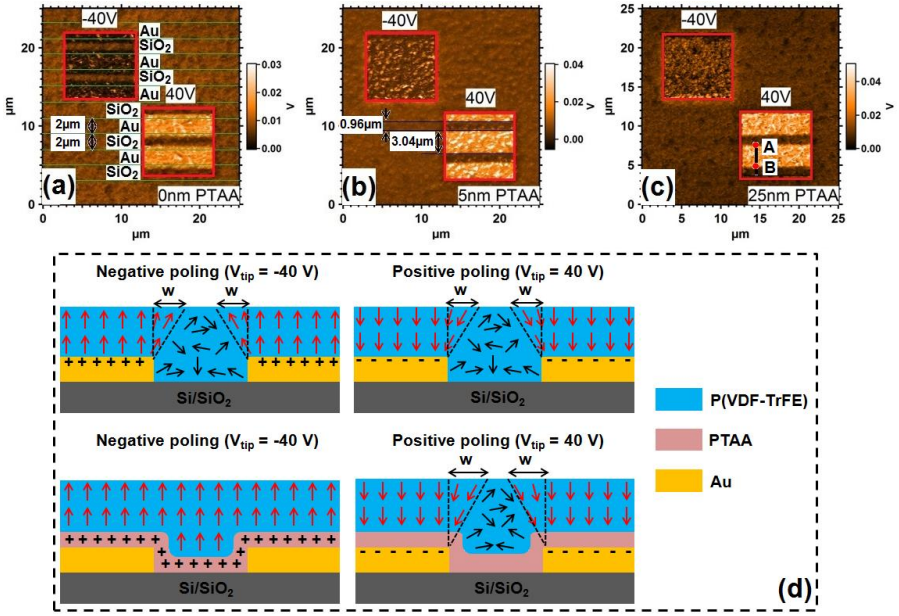

Figure 3.3: (a-c) PFM amplitude images of a 340 nm P(VDF-TrFE) film in a FeFET configuration with PTAA layers of different thickness. All images have two small regions (8 x 8 µm^2, boxed in red) poled by applying -40 V or 40 V to the tip while keeping the source-drain electrodes grounded. Then the PFM images were obtained over a large region (25 x 25 µm^2). (a) A reference sample with 0 nm PTAA layer. The underlying source-drain Au regions and SiO_2 regions are indicated by green lines. The width of these two regions is 2 µm. (b) A sample with 5 nm PTAA layer. For 40 V tip bias, the width of the regions with strong and minor contrast with the background are 3.04 µm and 0.96 µm, respectively. (c) Same, for a 25 nm thick PTAA layer. Points A and B indicate the borders of the poled region with strong contrast. A cross section along the black line AB is drawn in the Supporting Information for detailed analysis. (d) Schematic cross-section of a FeFET, showing the polarization after poling, depending on poling voltage polarity, in the absence or presence of a thin PTAA layer. Red arrows indicate the dipole moments in poled regions and black arrows are for unpoled regions. The compensating charges in the PTAA or electrodes are also indicated.

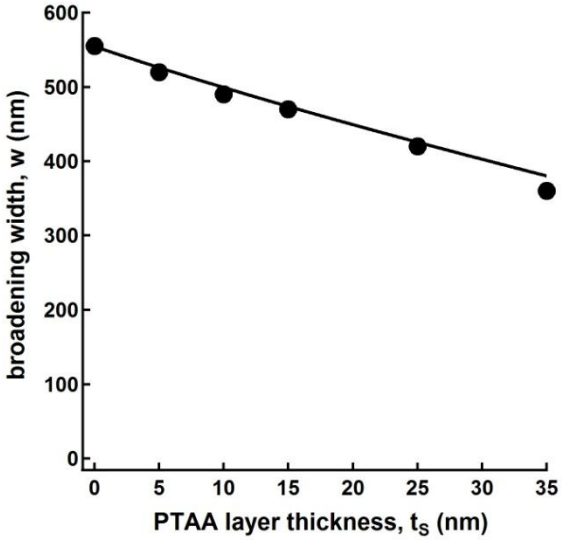

Figure 3.4. Width of the poled stripe at the edge of the electrodes over the channel regions, *w*, versus PTAA layer thickness, t_S, for the FeFETs of Fig. 3 comprising a ferroelectric layer of 340 nm thickness, after positive poling at 40 V. The closed circles are the experimental data; the continuous line is the prediction from the model (Equation 3.1).

The permanently-polarized regions are defined by the regions over which the electric field in the ferroelectric layer during poling is larger than the coercive field; they are shown schematically in Fig. 3.3 (d) for the different cases considered here. A detailed analysis of this phenomenon needs to take into account the division of the poling voltage between the insulating depleted PTAA layer and the ferroelectric layer, and allows to obtain the size and shape of the polarized regions. From this analysis (in the Supporting Information), the coercive field E_c of the P(VDF-TrFE) layer is found to be 61.5 MV/m, and the broadening of the polarized regions at the edge of the electrodes, *w*, is computed to be:

$$w = (t_F + t_S) \cdot \tan\left(\arccos\left(\frac{E_c t_F}{V} \cdot \left(1 + \frac{\varepsilon_F}{\varepsilon_S}\frac{t_S}{t_F}\right)\right)\right) \quad \text{(Equation 3.1)}$$

with t_F and t_S the thickness of the ferroelectric and semiconducting layers, respectively, V the applied poling voltage, and ε_S (3) and ε_F (10) the relative permittivities of the semiconducting and ferroelectric materials, respectively. This equation represents properly the broadening of the poled regions seen by PFM at the top surface of the ferroelectric layer (Fig. 3.4).

During the poling at positive voltages, the depleted PTAA layer thus acts as an insulator and voltage divider; therefore, the effective voltage on the P(VDF-TrFE) is lower than the total applied poling voltage, and the poled regions decrease in size for thicker PTAA layers, as Fig. 3.4 clearly shows. This effect defines the shape and size of the poled regions. However, after positive poling, the depleted PTAA layer plays a second role, which is to screen the compensating charges provided by the metallic electrodes, as was seen in the MSF devices. Due to incomplete compensation, the poled regions partially depolarize, resulting in a lower PFM contrast. This was confirmed by checking the polarization of P(VDF-TrFE) after application of different poling voltages to a FeFET comprising a 25 nm-thick PTAA layer (Fig. 3.5). When the PTAA layer is in accumulation mode and plays the role of an electrode, the PFM contrast between poled and unpoled regions increases for more negative poling voltages, reaching saturation below -30 V poling voltage (the 'coercive voltage' is about -21 V for a 340 nm-thick ferroelectric layer). However, when the PTAA layer is depleted, the PFM contrast in the poled regions is far from saturation at 30 V, which is essentially due to depolarization after poling since our previous model shows that the coercive field is attained above the electrodes in these conditions.

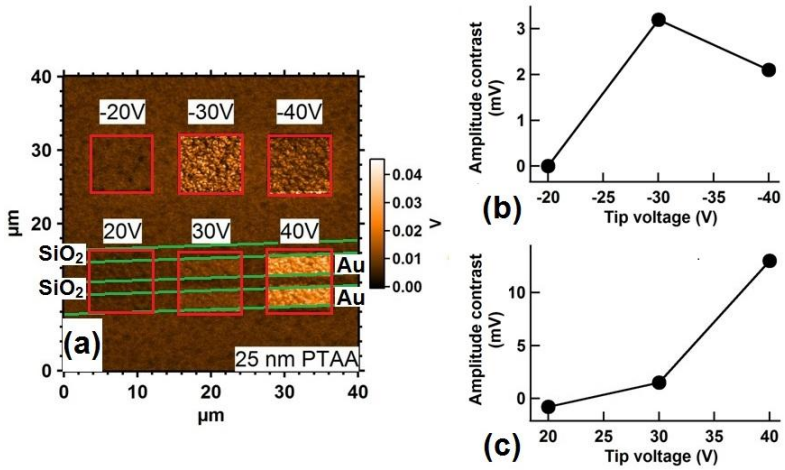

Figure 3.5: PFM response of a P(VDF-TrFE) film in a FeFET configuration with a 25 nm-thick PTAA layer, measured for different poling voltages. (a) PFM amplitude image with six small regions poled by applying different tip voltages (8 x 8 μm^2). The poled regions are boxed in red and the applied tip voltages are marked on top of each red box. The underlying Au and SiO_2 regions are the same as in Fig. 3.3, and are therefore not marked on the image. The PFM amplitude contrast between the poled regions and the unpoled background region is plotted in panels (b) and (c).

At this stage, we have thus developed a fine understanding of polarization in FeFETs during and after poling. When the semiconducting PTAA is in accumulation, a stable upward polarization state is obtained over the complete device during and after poling, because the PTAA layer acts as an electrode during poling, and subsequently provides free holes which compensate the polarization charges at the P(VDF-TrFE)/PTAA interface. In this case, the thickness of PTAA layer has minor influence on the polarization behavior and the saturation polarization is obtained for the same poling voltage, whatever the PTAA thickness (30 V is enough for 340 nm P(VDF-TrFE) with our processing conditions). When the semiconducting PTAA is depleted, the poling efficiency is reduced, because the voltage is divided between the insulating PTAA layer and the ferroelectric layer; therefore, poled regions are limited to the

regions shown in Fig. 3.3 (d) and described by Eq. 3.1. However, even though the internal poling field is high enough in these regions, their polarization is partially lost when the poling field is removed, because the compensating charges provided by the metallic electrodes are not in direct contact with the ferroelectric layer, which corresponds to increased electrostatic energy as shown by the study of the MSF systems. Therefore, thinner PTAA layers (typically below *ca.* 20 to 25 nm) are needed if two stable polarization states of opposite polarity are desired. In addition, we also checked these two polarization states right after and one day after the poling; no significant decreasing of the amplitude contrast was observed, indicating these two polarization states are stable over long times (Fig. 3.10 in the Supporting Information).

3.3.3 Characterization of complete FeFET devices

The previous experimental results can now be used to describe the behavior of complete FeFET devices (Fig. 3.1 (c)). When the FeFET is poled negatively, the ferroelectric layer is completely upward-polarized provided the poling voltage corresponds to an electric field larger than E_c (Fig. 3.6 (a)). When the poling voltage is decreased to zero, the polarization is essentially conserved, corresponding to the stable "on"-state with polarization-compensating holes accumulated in the semiconducting layer and therefore a high channel conductance (Fig. 3.6 (b)). When a positive poling voltage is applied onto this stable state, the polarization state of the ferroelectric switches downwards at a given switching voltage V_{dp}, over the metallic electrodes and in a narrow edge region over the channel described by equation 3.1. The extent of polarization depends on the conditions of poling. In the rest of the channel region, the ferroelectric depolarizes due to the lack of compensating charges in the now-depleted semiconducting channel (Fig. 3.6 (c)). This corresponds to a strongly-depleted semiconducting channel, and a low current. When the poling voltage is subsequently decreased to zero, the ferroelectric polarization in the poled region partially depolarizes

depending on the thickness of the PTAA layer. Hence, the stable "off"-state is one into which, depending on the thickness of the PTAA layer, a partially-polarized region exists over the electrodes and close to them, whereas the material is unpolarized in the remaining part of the device over the channel (Fig. 3.6 (d)). Depending on the extent of depolarization and thus on the PTAA thickness, the semiconducting channel will be more or less depleted, with a more or less low channel conductance. This description is valid for a p-type semiconducting layer such as PTAA; it should be reversed if a n-type semiconductor is used.

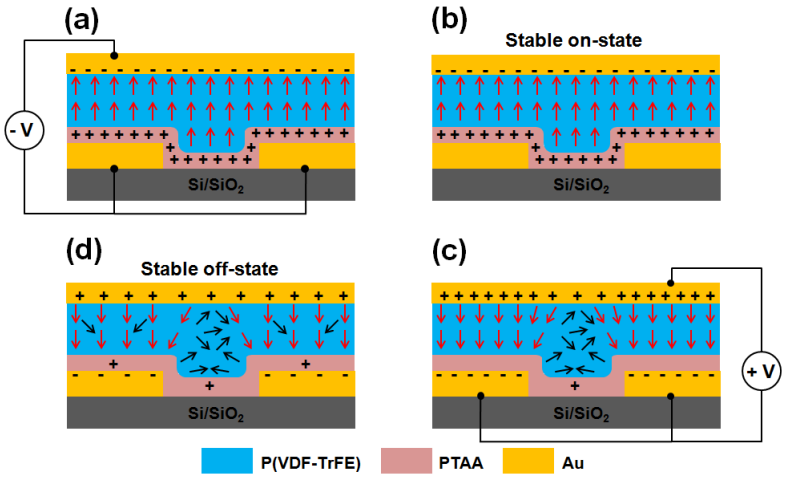

Figure 3.6. Schematic drawing of the state of a FeFET at different stages of its poling (the poling voltage is applied to the gate electrode and the source/drain electrodes are grounded (V_{ds} = 0)). The red arrows indicate poled regions, black arrows showing the local dipole moments in depolarized regions. The degree of the depolarization in the case of positive poling depends on the thickness of the PTAA layer. Compensating charges are also indicated.

FeFET devices were then fabricated with a P(VDF-TrFE) layer of 340 nm, while the semiconducting PTAA layer thickness was different for each device, ranging from 10 nm to 35 nm. Fig. 3.7 (a) shows three series of transfer curves obtained by applying different

poling gate voltages of a FeFET with a channel length L = 2 µm, a channel width W = 31.5 mm and a 35 nm semiconducting PTAA layer. All curves exhibit hysteresis loops which are typical for memory FeFETs.

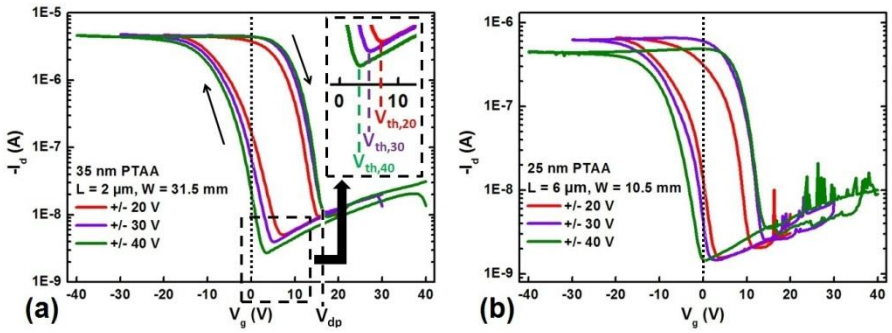

Figure 3.7: Transfer curves of two FeFETs with different source-drain configuration and PTAA layer thickness. Both graphs present three transfer curves with different gate sweeping voltage ranges of ±20 V, ±30 V, and ±40 V, by applying a same source-drain voltage V_d of -5 V. A dotted vertical line at 0 V is drawn as reference in both graphs. (a) FeFET with a 35 nm-thick PTAA layer and a source-drain configuration with L = 2 µm and W = 31.5 mm. The threshold voltages V_{th} in the case of different sweeping voltage ranges are indicated in the enlarged insertion panel. Black arrows indicate the gate voltage sweeping direction. The depolarization voltage (V_{dp}) from the upwards saturated polarization state corresponding to the accumulation regime of PTAA is also indicated. (b) FeFET with a 25 nm-thick PTAA layer and a source-drain configuration with L = 6 µm and W = 10.5 mm.

Starting from the negatively polarized state, the channel current is preserved at a high value when the gate voltage is increased to the stable on-state at 0 V, corresponding to moving from (a) to (b) in Fig. 3.6. When increasing further the gate voltage to positive values, the current decreases abruptly at V_{dp}, at which stage the ferroelectric depolarizes in the channel region (Fig. 3.6 (c)), resulting in a low channel current. Depolarization occurs for a lower value of voltage when the transistor was initially poled at -20 V (red curve), because the saturation of the polarization was not reached for this poling

voltage; however, saturation is obtained when poling at -30 and -40 V (Fig. 3.5 (b)), with as a result an identical depolarization voltage (green and purple curves).

When sweeping back the gate voltage to zero, the current increases again below a threshold voltage V_{th}, which is due to partial depolarization of the ferroelectric over and close to the electrodes (Fig. 3.6 (d)). Interestingly, as shown in the inset of Fig. 3.7 (a), the threshold voltage is lower when using higher poling voltages, which results from three effects: first, higher poling voltages correspond to larger poled regions in the depletion regime (Fig. 3.5); second, higher poling voltages also correspond to more polarized poled regions (Fig. 3.5 (c)) – at least within the 30-40 V poling voltage range; third, this more polarized state makes PTAA more depleted and increases the charge injection barrier between the source-drain electrode and PTAA (a simplified band diagram of the Au/PTAA/P(VDF-TrFE) structure is shown in Fig. 3.11 of the Supporting Information).[11, 101]

Less positive V_{th}'s are beneficial, because they increase the on/off current ratio at zero gate bias which is an important operational parameter for FeFET memory devices. For instance, the on/off ratio of the FeFET of Fig. 3.7 (a) is increased by a factor of 10 by changing the positive poling voltage from 20 V to 40 V.

Fig. 3.7 (b) shows transfer curves of a FeFET employing a different device configuration (L = 6 µm, W = 10.5 mm) and a PTAA layer of different thickness (25 nm) compared to that in Fig. 3.7 (a). A generally similar behavior as in Fig. 3.7 (a) is observed, indicating that our analysis is independent of the FeFET configuration and of the semiconducting PTAA layer thickness. The current in the on-state is lower due to the lower channel conductance. Importantly, the threshold voltage in Figure 7b is less positive (and even negative) than in Fig. 3.7 (a); this results from the thinner PTAA layer, leading to a wider poled region of lower degree of depolarization, resulting in a more depleted PTAA layer and a larger charger injection barrier. The importance of the PTAA thickness was also checked by using the same device configuration: Fig. 3.8 presents the transfer curves of two

FeFETs with L = 6 µm and W = 10.5 mm, but of different PTAA layer thickness (10 and 25 nm). The poling voltage sweeping range of the two FeFETs was the same (±30 V). As expected, V_{th} is less positive for the device with a 10 nm PTAA layer, because the poled regions are larger and more polarized. However, the right part of the curves coincides, indicating identical depolarization voltages, because the same saturated polarization on-state is obtained by applying a -30 V gate poling voltage.

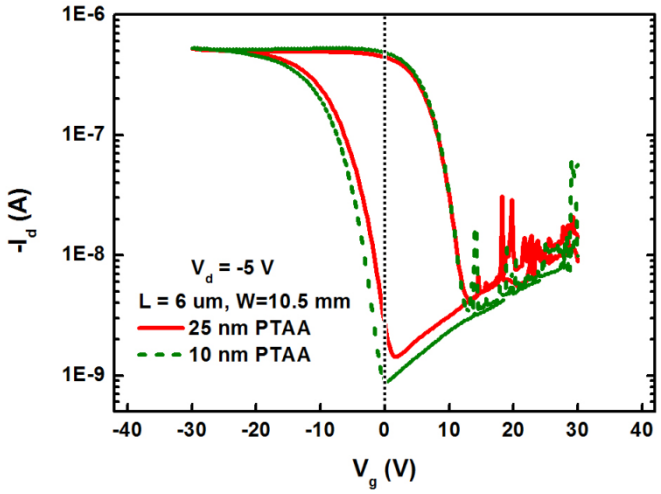

Figure 3.8: Transfer curves of two FeFETs with a 10 and 25 nm PTAA layer, respectively. A dotted vertical line at 0 V is drawn as reference

The present results demonstrate that thinner semiconducting layers give larger downwards polarizations and therefore better device performance. However, the semiconducting layer thickness might also affect the film quality and therefore the semiconducting properties. Fig. 3.12 in the Supporting Information shows that a flat surface with a roughness smaller than 0.2 nm is obtained for a 10 nm PTAA layer. In contrast, PTAA films less than 10 nm exhibit a large amount of defects, probably due to the fast evaporation of the solvent during the spin-coating. Of note, these defects could have a huge influence on the conductance of a semiconductor device (*e.g.*, a FeFET), but do not

affect the polarization behavior of P(VDF-TrFE) observed in this chapter. Therefore, the optimized PTAA layer thickness should be in the range of 10 to 20 nm in order to obtain a considerable downwards polarization state and a large on/off ratio at zero gate bias. A further factor to take into account is that the mobility of the semiconductors (especially small molecular ones) strongly depends on the film thickness.[164, 165]

We thus conclude that, when the PTAA layer is depleted, the spatial extent and magnitude of the polarization over the source-drain electrodes and neighboring regions modulate the position of the threshold voltage, resulting in higher or lower on/off current values at zero gate bias. The on/off ratio can be increased by up to 2 orders of magnitude in our case by carefully choosing the PTAA layer thickness, *e.g.*, 10 nm compared to 45 nm. Similar degrees of improvement of the on/off ratio were also reported recently;[21] in that work, a 80 nm PTAA layer was used and a second gate was employed to control the threshold voltage and the on/off current ratio. Our work shows that tuning the PTAA layer thickness affords another handle to control the on/off ratio, with the advantage of being intrinsic and not requiring to use a second controlling gate.

3.4 Conclusions

In summary, we have systematically studied the local ferroelectric polarization and/or depolarization of P(VDF-TrFE) in MFS and unipolar top-gate bottom-contact FeFET devices using p-type poly(triarylamine) as organic semiconductor. PFM results show that a stable "on" upward-pointing polarization state can be obtained irrespective of the location in FeFETs of P(VDF-TrFE) (on channel regions or source-drain electrode regions), in which the semiconducting layer acts as an electrode during poling and provide compensating charges at the PTAA/P(VDF-TrFE) interface after removal of the poling voltage. Another stable state is also achievable in these devices when the depleted PTAA layer is thin enough and/or

the poling voltages are sufficiently large. In this state, the ferroelectric is depolarized over the main part of the channel regions, whereas it is polarized downwards over the electrodes and neighboring channel regions. The size of the polarized regions depends on the thickness of the semiconducting layer, because PTAA acts as an insulator dividing the applied voltage during poling; in addition, their degree of polarization after removal of the poling voltage also depend on the thickness of the PTAA layer, which screens the polarization-compensating charges accumulated in the source and drain electrodes. These polarized regions in the second stable state make the PTAA more depleted and modify the charge injection barrier between the electrode and the PTAA layer. As a result, FeFET devices of thinner PTAA layer have less positive (and even negative) threshold voltages, leading to an increase of the on/off current ratio at zero gate bias and therefore to an improvement of the memory device performance.

The semiconductor thickness dependence of the ferroelectric polarization in a FeFET is likely to be universal, because similar polarization behaviors were reported for other organic/inorganic semiconductors.[18, 20] Therefore, our investigation and results provide new clues for device design and performance optimization of memory FeFETs. In addition, our results give a complete spatial view, and thereby understanding, of ferroelectric polarization and depolarization in these complex devices, and on the working mechanism of memory FeFETs, as summarized in Fig. 3.6.

3.5 Supporting Information

3.5.1 Computation of the layer thicknesses and fields in the poling region in FeFET devices.

A cross-section of a FeFET device is shown in Fig. 3.9. Previous AFM experiments performed for thin PTAA layers (up to 45 nm thick) spin-coated over protruding gold electrodes showed that the PTAA

layer conformally covers the electrodes;[163] what is not known, however, is the exact profile of the PTAA layer at the edge of the electrodes. As for the P(VDF-TrFE) layer, it is thick enough to planarize the structure. Points A and B in Fig. 3.9 are the positions where the PFM contrast starts to appear, *i.e.*, at which the coercive field is reached when a poling voltage of 40 V is applied (Fig. 3.3 (c)). Stated otherwise, the electric field in P(VDF-TrFE) is equal to the coercive field along the line AC of Fig. 3.9. Based on the geometry of the cross-section, on the ferroelectric and semiconducting layer thicknesses (t_F = 340 nm and t_S = 0 to 35 nm, respectively), and on the measured value of broadening of the poled region (w, Table 3.1), it is possible to compute the voltage drop *in the ferroelectric layer* along the AC line, $V_{AD} = t_F' E_c$, where E_c is the coercive field and t_F' is the thickness of the ferroelectric layer along the AC line (Fig. 3.9).

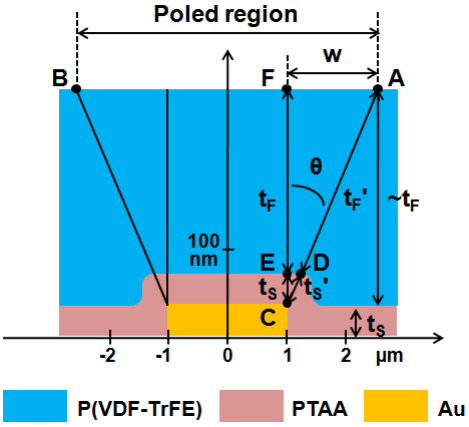

Figure 3.9. Schematic drawing of the cross-section of a FeFET device. The AC line indicates the boundary of the region beyond which the electric field during poling is below the coercive field.

In the absence of a PTAA layer (Fig. 3.3 (a)), the voltage drop V_{AD} is the applied voltage (40 V); since w = 555 nm and t_S = 0, t_F' = 651 nm, which provides an experimental value for the coercive field

E_c = 61.5 MV/m, close to the reported values of coercive field for relatively thick P(VDF-TrFE) films.[15, 20]

In the presence of a PTAA layer thin enough not to fully screen the compensating charges from the electrodes, the following two equations may be solved to obtain t_F' and t_S', which are the thicknesses of the ferroelectric and semiconducting layers along the AC line (Fig. 3.9):

$$t_F' + t_S' = \sqrt{(t_S + t_F)^2 + w^2} \quad \text{and} \quad V_{AD} = E_c t_F' = V \frac{\epsilon_S / t_S'}{(\epsilon_S / t_S') + (\epsilon_F / t_F')},$$

where V is the applied poling voltage (40 V), and ε_S = 3 (resp. ε_F = 10) is the relative permittivity of the semiconducting (resp. ferroelectric) layer. The first equation is purely geometrical, whereas the second expresses that the applied poling voltage is shared between two series capacitors and that the electric field on the ferroelectric layer at the limit of the polarization zone is equal to the coercive field.

The resulting thickness values are collected in Table 3.1, from which the voltage drops $V_{AD} = t_F' E_c$ and $V_{DC} = V - V_{AD}$ can be trivially computed. These voltage drops are very close to the values of voltage drops in flat MSF devices of same layer thickness, which indicates that the voltage division is essentially not perturbed by edge effects in the poled region. Therefore, it becomes possible to simplify the estimation of the width of the poled region, w. Defining θ as the angle between the AC line and the vertical direction (Fig. 3.9),

$$w = (t_S + t_F)\tan(\theta) \quad \text{and} \quad E_c = \frac{V_{AD}}{t_F'} \approx \frac{V_{EF}}{(t_F / \cos\theta)},$$

in which $V_{EF} = \dfrac{V}{1 + (\epsilon_F / \epsilon_S) \cdot (t_S / t_F)}$ is the voltage drop in the ferroelectric layer over the electrodes, far from their edges (as in a MSF device). Therefore,

$$w \approx (t_F + t_S)\tan\left(\arccos\left(\frac{E_c t_F}{V}\cdot(1+\frac{\epsilon_F}{\epsilon_S}\frac{t_S}{t_F})\right)\right)$$
$$= (t_F + t_S)\sqrt{\frac{V^2}{{E_c}^2{t_F}^2\cdot(1+\frac{\epsilon_F}{\epsilon_S}\frac{t_S}{t_F})^2}-1} \qquad \text{(Equation 3.2).}$$

Table 3.1: Different geometrical and electrical parameters obtained from the analysis of PFM images of poled FeFET devices.

t_S[(1)] (nm)	w[(2)] (nm)	t_F' [(3)] (nm)	t_S' [(4)] (nm)	V_{AD}[(5)] (V)	V_{DC}[(6)] (V)	w_{calc}[(7)] (nm)
0	555	651	0	40	0	554
5	520	615	9	37.8	2.2	526
10	490	585	17	36.0	4.0	499
15	470	564	25	34.7	5.3	474
25	420	518	38	31.9	8.1	426
35	360	471	49	29.0	11.0	380

(1) Measured thickness of the PTAA layer; (2) Measured broadening of the P(VDF-TrFE)-polarized region on one side of the source or drain electrodes; (3) Computed distance DA in Fig. 3.9; (4) Computed distance CD in Fig. 3.9; (5) Computed voltage drop over the ferroelectric layer, along the line AC of Fig. 3.9; (6) Computed voltage drop over the semiconductor layer, among the line AC of Fig. 3.9; (7) Computed broadening of the P(VDF-TrFE) region, equation 3.2.

A comparison between the measured and computed values of w is given in Table 3.1 and Fig. 3.4. The measured and computed values agree very well, within better than 20 nm, confirming the predictive ability of equation 3.2 when using E_c=61.5 MV/m, ε_S = 3 and ε_F = 10.

3.5.2 Stability of the two polarization states

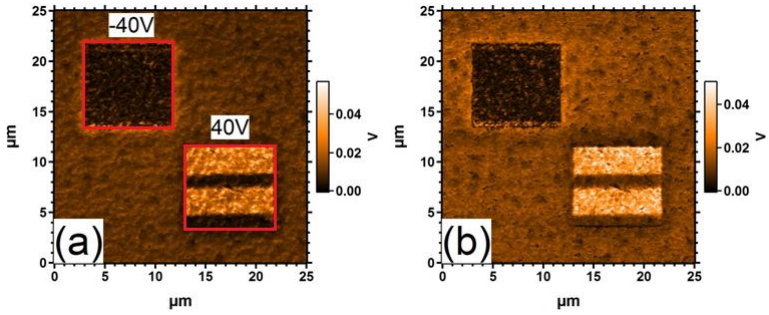

Figure 3.10: PFM amplitude images of a FeFET with 15 nm PTAA and 340 nm P(VDF-TrFE) which was poled on two small regions by -40 V (left-top) and 40 V (right-bottom) tip bias. (a) The image was taken right after the poling; (b) The image was taken one day after the poling and no significant decreasing of the amplitude contrast is observed compared to that in (a), showing that the two polarization states in our FeFET are stable over long times.

3.5.3 Simplified band diagram of the metal/semiconductor/ferroelectrics structure

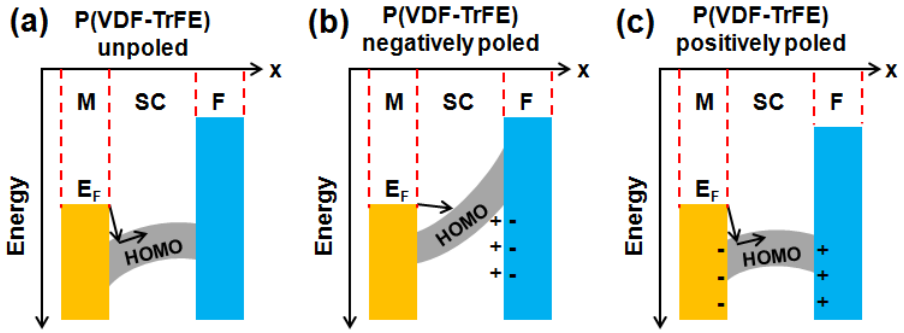

Figure 3.11. Band diagram of the Au/PTAA/P(VDF-TrFE) (M/SC/F)structure, taking 4.8 eV for the work function of Au,[101] and 5.2-5.6 eV for the HOMO level of PTAA.[166] (a) P(VDF-TrFE) is unpoled; (b) P(VDF-TrFE) is negatively poled and PTAA is in the accumulation state; (c) P(VDF-TrFE) is positively poled and PTAA is in the depletion state.

3.5.4. AFM images of thin PTAA layers

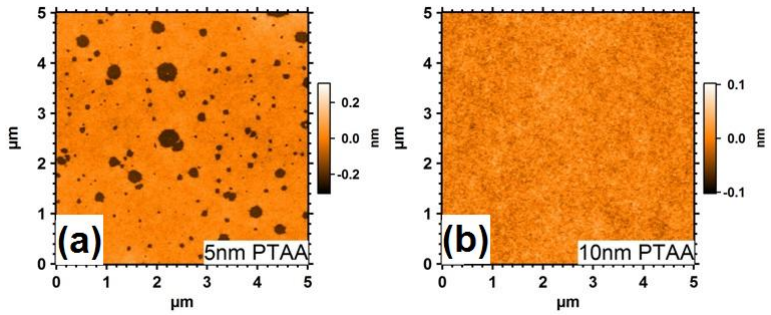

Figure 3.12: Topography images of two PTAA layers spin-coated on SiO_2. The PTAA layer thickness is (a) 5 nm and (b) 10 nm.

Chapter 4

An Organic Ferroelectric Field-Effect Transistor with P(VDF-TrFE) Nanowires as Gate Dielectric

Abstract. In this chapter, we demonstrate the fabrication of an organic ferroelectric field-effect transistor (FeFET) incorporating a ferroelectric gate dielectric made of nanowires obtained by nanoimprinting poly(vinylidene fluoride-co-trifluoroethylene) over a layer of semiconducting poly(triarylamine). The imprinting process results in a decreased switching voltage for the ferroelectric, by a factor of *ca.* 1.5, resulting in a decreased operating voltage compared to a reference FeFET with a continuous ferroelectric layer. The transistor consists of a large number of nanowire-gated transistors placed in parallel, which also offers interesting possibilities for a strong size reduction of organic FeFETs.[*]

[*] Results in this chapter were published in Applied Physics Letters, 105, 113113 (2014)

4.1 Introduction

Organic ferroelectric field-effect transistors (FeFETs) incorporating poly(vinylidene fluoride-*co*-trifluoroethylene) (P(VDF-TrFE)) as gate dielectric, have been intensively studied for non-volatile memory applications over the last decade.[12-16, 18, 19, 112-114, 167-171] P(VDF-TrFE) crystallizes predominantly in a polar ferroelectric phase characterized by a remnant polarization of *ca.* 70 mC/m^2 (for ~30% TrFE) and a coercive field of *ca.* 50 MV/m. By applying a gate voltage V_{gs}, the P(VDF-TrFE) is permanently polarized, resulting in the accumulation of charge carriers in the semiconducting layer at its interface with the P(VDF-TrFE) layer even after gate voltage removal, *i.e.*, at V_{gs} = 0 V. The source-drain current I_{ds}, which is measured by applying a small source-drain voltage V_{ds}, therefore exhibits two current states, I_{on} and I_{off}, depending on the direction of polarization of P(VDF-TrFE) and on the semiconductor type. Since FeFET memories typically require smaller V_{gs} and higher ON/OFF current ratios, several methodologies have been explored to improve performance, including using high mobility semiconductors, improving the ferroelectric properties of P(VDF-TrFE), or optimizing the quality of the semiconductor/P(VDF-TrFE) interface.[13, 15, 16, 113, 172, 173]

Here we focus on exploring the effect of nanoimprinting lithography (NIL) on the ferroelectric performance of P(VDF-TrFE) in an organic FeFET. We have previously reported that, when P(VDF-TrFE) crystallizes in confinement in the nanocavities or nanochannels of a NIL mold, preferred crystallographic orientation and a significant increase of crystal perfection are observed; as a result, the coercive field of the material is significantly decreased.[57, 58] Similar improvements were also reported for the crystallization of P(VDF-TrFE) in other confined media.[60, 174] Here, we integrate nanoimprinting of P(VDF-TrFE) in the FeFET fabrication process, in order to decrease the gate voltage V_{gs} needed to reach the saturation remnant polarization P_r; this concept simultaneously leads to an unusual FeFET wherein the gate ferroelectric is in the form of nanowires running perpendicular to source and drain (Fig. 4.1).

4.2 Experimental

Materials. P(VDF-TrFE) with 35 weight % of TrFE units and a weight-average molar mass of *ca.* 300 000 g/mol was provided by Solvay Specialty Polymers. Poly(triarylamine) (PTAA) was purchased from Flexink. P(VDF-TrFE) was dissolved in acetylacetone at different concentrations (35 g/L or 60 g/L). PTAA was dissolved in toluene (10 g/L). All solutions were filtered by PTFE filters with pore size of 0.45 µm before spincoating.

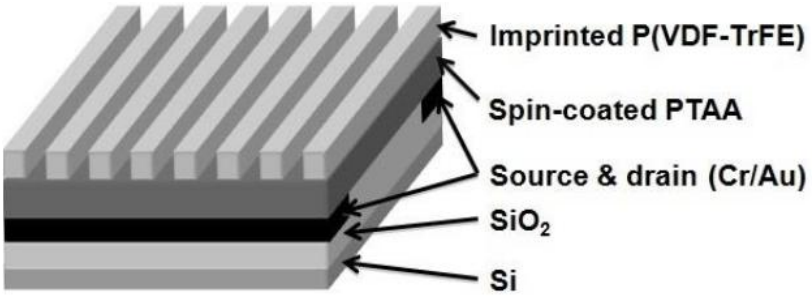

Figure 4.1: Scheme of a FeFET with nanoimprinted ferroelectric. In the case of the reference FeFET, the imprinted P(VDF-TrFE) was replaced by a continuous film.

FeFET Fabrication. Source and drain electrodes were defined by standard photolithography on a Si (100) substrate covered by 200 nm of thermally-grown SiO_2, followed by the local etching of 30 nm SiO_2, the deposition of 5/25 nm Cr/Au, and metal lift-off. These processes led to buried interdigitated source-drain electrodes in an almost perfectly planar substrate. The PTAA solution was spincoated at 2000 rpm for 1 min on this substrate, resulting in the deposition of *ca.* 45 nm PTAA. A 35 g/L P(VDF-TrFE) solution was then spincoated at 3500 rpm for 1 min on the PTAA layer. Acetylacetone, used to dissolve P(VDF-TrFE), is an orthogonal solvent and hence does not affect the underlying PTAA layer. The P(VDF-TrFE) film, of *ca.* 95 nm initial thickness, was nanoimprinted under 60 bar at 135 °C (in-between the Curie transition and the melting point) with an

Obducat imprinter. (using mold L400, see its geometry in Appendix A1) After 10 min imprinting time, the system was cooled to room temperature. During imprinting, the line direction was placed normal to the source-drain direction. After imprinting, the resulting P(VDF-TrFE) nanowires were of *ca.* 200 nm width, 200 nm spacing , and 185 nm height. They were effectively isolated from each other, since the initial thickness of the P(VDF-TrFE) layer was selected to be *ca.* 95 nm in order to ensure nanoimprinting in complete confinement. The resulting device is shown in Fig. 4.1. For the reference device, a 60 g/L P(VDF-TrFE) solution was spincoated at 3500 rpm for 1 min on the PTAA layer, resulting in a film of *ca.* 185 nm thickness, equal to the height of the ferroelectric nanowires in the imprinted samples. This reference device was annealed at 135 ℃ for 10 min on a hot plate to improve crystallinity. The thicknesses of the PTAA layer and of the P(VDF-TrFE) layers were measured by Atomic Force Microscopy (AFM).

Characterization of Morphology and Piezoresponse. The morphology of the continuous films and nanoimprinted nanowires was checked by a Multimode AFM (Nanoscope IV, Bruker) in tapping mode with silicon cantilevers from Nanosensors (force constant of ~40 N/m, apex radius of curvature <7 nm). The piezoresponse of the continuous and nanoimprinted P(VDF-TrFE) films was checked by Piezoresponse Force Microscopy (PFM) in contact mode. An Agilent 5500 AFM (Agilent Technologies) system equipped with a Mac III Controller lock-in amplifier was adapted to the requirements of the PFM technology, in order to apply dc biases larger than 10 V. To make PFM measurements, the source-drain electrodes were used as bottom electrodes. A conductive Si cantilever from Nanosensors (Boron-doped diamond-coated, force constant of 0.02−0.77 N/m) was used as a mobile top electrode. The ferroelectric response was inspected in PFM image mode with an oscillating voltage of 0.5 V amplitude, added to a polarizing dc bias. All PFM measurements were done by applying the ac driving bias V_{tip} on the cantilever, while the

poling was done by applying the dc bias $V_{s\&d}$ on the source-drain electrodes and setting the ac bias to zero (Fig. 4.2 (a)). Here we define the poling voltage $V_{tip,pol} = V_{gs} = V_{tip} - V_{s\&d} = -V_{s\&d}$.

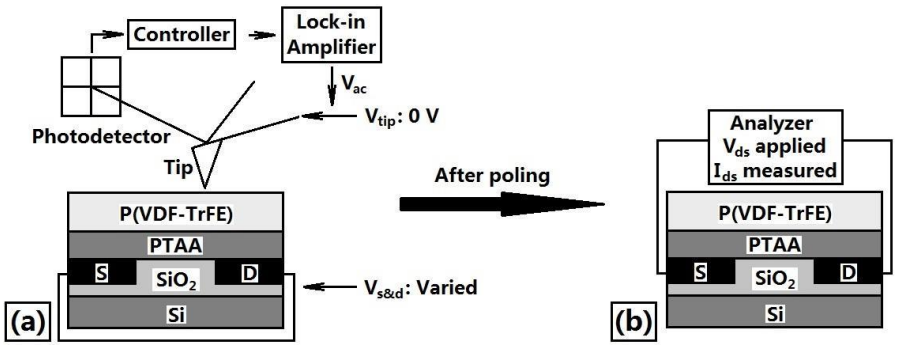

Figure 4.2: Configuration of the setups for (a) applying $V_{tip,pol}$ to pole P(VDF-TrFE) and (b) applying V_{ds} to measure I_{ds}. The structure of the FeFET device here is along the P(VDF-TrFE) nanowire shown in Fig. 4.1 and normal to the long axis of the S/D electrodes.

FeFET Characterization. P(VDF-TrFE) was first poled by applying a poling voltage $V_{tip,pol}$. Then the source-drain current I_{ds} was measured after the removal of $V_{tip,pol}$. As shown in Fig. 4.2 (a), the same setup configuration as for PFM measurements was used to pole P(VDF-TrFE). Then a Keithley analyzer (Model 6430 with femtoampere accuracy) was used to apply a source-drain voltage V_{ds} and measure the source-drain current I_{ds} (Fig. 4.2 (b)).

4.3 Results and Discussion

4.3.1 FeFET fabrication

Fig. 4.3 shows the topography of the surfaces along the different fabrication steps. To avoid contamination and damage to the NIL molds, the Au electrodes should not be higher than the SiO_2 part.

Therefore, the Au electrodes were buried into the substrate as mentioned above. Fig. 4.3 (a, e) shows such a substrate with Au electrodes at the same level as the SiO_2 background. Deposition of the PTAA layer flattens further the substrate (Fig. 4.3 (b, f)). A surface devoid of any topology of electrodes is obtained after spincoating *ca.* 95 nm P(VDF-TrFE) on PTAA (Fig. 4.3 (c, g)): the average roughness is 8.0 nm, comparable to the values reported for a P(VDF-TrFE) film spin-coated on a flat surface.[14, 168] NIL applied on this P(VDF-TrFE) film produces well-defined nanowires of *ca.* 185 nm height and 200 nm width (Fig. 4.3 (d, h)). The nanowires were imprinted perpendicularly to the source and drain electrodes. Due to tearing during demolding, and mold imperfections, a few defects were distributed along the array of nanowires; Fig. 4.3 (d) shows a typical image. After optimization, the process led to well-structured nanoimprinted FeFETs with a reasonable production yield (> 90%). For current characterization, a conductive PFM cantilever was used as gate instead of a traditional metal electrode. The schematic diagram of such a nanoimprinted FeFET with top-gate bottom-contact configuration and a mobile gate is shown in Fig. 4.2 (a).

4.3.2 Piezoresponse of the continuous P(VDF-TrFE) film and of the nanoimprinted P(VDF-TrFE) film

The switching of the continuous and nanoimprinted P(VDF-TrFE) films atop PTAA in the FeFET architecture was studied by PFM : a series of regions of the sample were poled by scanning the grounded tip while applying increasing dc voltages $V_{s\&d}$ to the source and drain electrodes; the sample was then imaged in PFM mode at zero dc bias. Fig. 4.4 (a, b) shows the resulting amplitude images, (c, d) phase images, of the continuous P(VDF-TrFE) film (a, c) and of the nanoimprinted P(VDF-TrFE) film (b, d)) For both films, the piezoresponse changes depending on the previously-applied $V_{s\&d}$. 10 V is insufficient to align the dipoles of P(VDF-TrFE); however, starting from 15 V for the continuous film and 12.5 V for the

nanoimprinted film, the PFM contrast starts to appear due to partial dipole alignment. The contrast increases for larger positive $V_{s\&d}$ and reaches a maximum when $V_{s\&d}$ is large enough to permanently align most dipoles in one direction. The maximum contrast means that the saturation P_r is obtained.

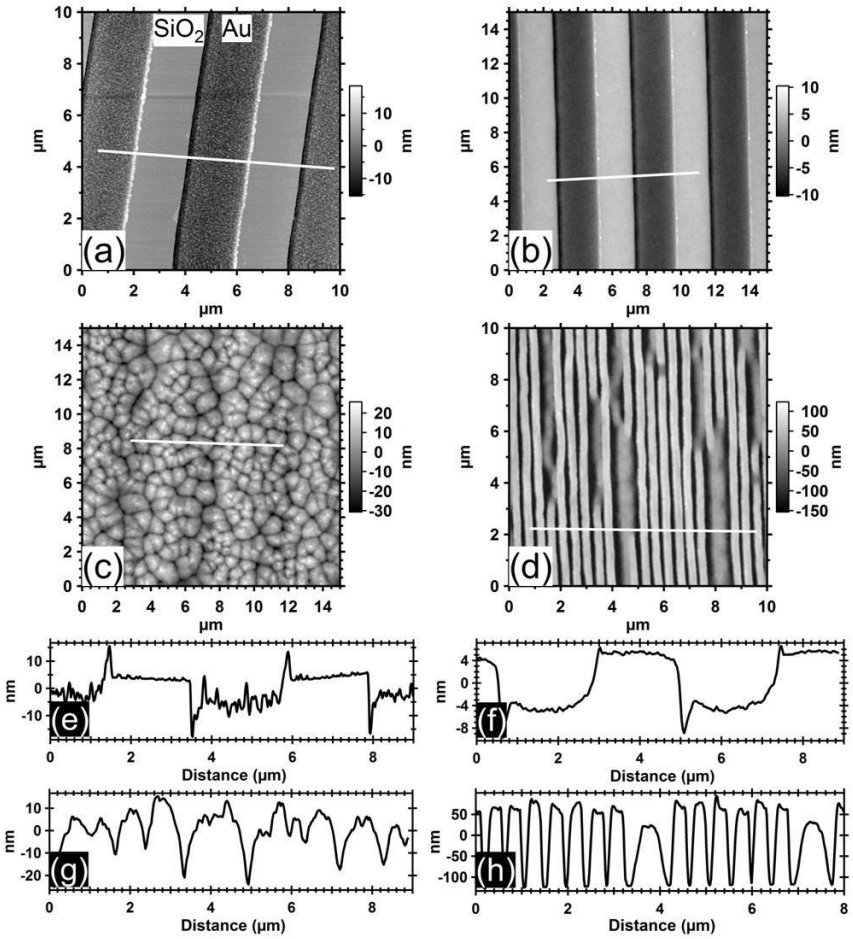

Figure 4.3: AFM morphology of: (a) buried S/D substrate; (b) PTAA layer spincoated on (a); (c) P(VDF-TrFE) layer spincoated on (b); (d) P(VDF-TrFE) nanowires by making nanoimprint on (c); (e)-(h) height profiles of the cross sections of (a)-(d): (e) corresponds to (a), (f) to (b), (g) to (c), and (h) to (d).

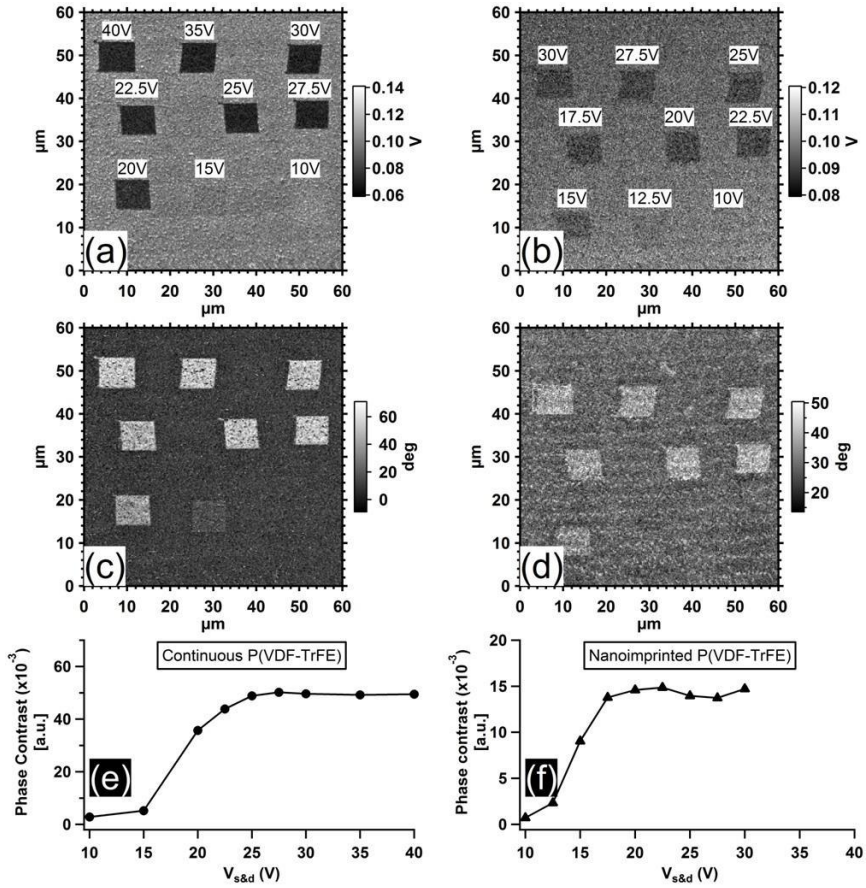

Figure 4.4: PFM piezoresponse (a) (b) amplitude images, (c) (d) phase images: (a) (c) for the continuous P(VDF-TrFE) in a reference FeFET and (b) (d) for the nanoimprinted P(VDF-TrFE) in a nanoimprinted FeFET. In all the images the background was polarized initially with a dc voltage of 0 V, and the smaller square areas of 8 µm x 8 µm were polarized with increasing positive dc voltages $V_{s\&d}$ applied on source-drain electrodes (given in panels (a) and (b)). All PFM images were recorded with a 0 V dc voltage; (e) (f) PFM piezoresponse phase contrast versus source-drain voltage $V_{s\&d}$: (e) for the continuous P(VDF-TrFE) and (f) for the nanoimprinted P(VDF-TrFE).

To determine at which voltage the maximum P_r can be obtained, the phase contrast was plotted versus $V_{s\&d}$ in Fig. 4.4 (e, f) for both the continuous and nanoimprinted P(VDF-TrFE) films. Here, the phase contrast was defined as $A_0\cos\varphi_0$ - $A\cos\varphi$, where A_0 and φ_0 are the average amplitude and the average phase of the background; A and φ are the average amplitude and phase of the smaller square areas where $V_{s\&d}$ was applied. As shown in Fig. 4.4 (e) and (f), the contrast reaches a maximum at 27.5 V and a plateau is obtained for voltages larger than 27.5 V for the continuous P(VDF-TrFE) film, while this point is 20 V for the nanoimprinted P(VDF-TrFE) film. Note that the thickness of the continuous film was selected so as to be equivalent to the height of the nanowires of the nanoimprinted sample. This means that the switching field of the nanoimprinted P(VDF-TrFE) is indeed lower than the one of the continuous film. For instance, at 15 V, *ca.* 5% of the maximum polarization contrast is obtained for the continuous film, whereas *ca.* 60% is obtained for the nanoimprinted film. Hence, the P(VDF-TrFE) dipoles are more easily aligned in nanowires than in the continuous film, with a switching voltage reduced by a factor of about 1.5. Previously, we showed that the coercive field of P(VDF-TrFE) imprinted over Si in nanowires of similar width was reduced by a factor of about 2 compared to a continuous film.[57] The lower effect found here might be due to the different nature of the bottom electrode.

4.3.3 Current characterization of the FeFETs

As before, a conductive cantilever was used as gate for the characterization of the device. The grounded tip was scanned over a defined area of 50 µm x 50 µm while setting $V_{s\&d}$ to a given value, in order to pole the system at $V_{tip,pol} = -V_{s\&d}$. Then, the polarization-induced source-drain current I_{pol} was measured as displayed in Fig. 4.2 (b), for different source-drain voltages V_{sd} and no applied gate voltage. Here, I_{pol} is defined as $I_{pol} = I_{ds} - I_{initial}$, where $I_{initial}$ is the source-drain current I_{ds} measured after the scanning at

$V_{tip,pol}$ = 0 V. This definition of the polarization-induced current rests on the fact that the P(VDF-TrFE) cannot be polarized at 0 V poling voltage; therefore, I_{pol} = 0. For both the reference and the nanoimprinted FeFET, I_{pol} is plotted in Fig. 4.5 versus V_{ds} (after scanning and removal of $V_{tip,pol}$), and in Fig. 4.6 versus the previously-applied $V_{tip,pol}$ at V_{ds} = 10 V.

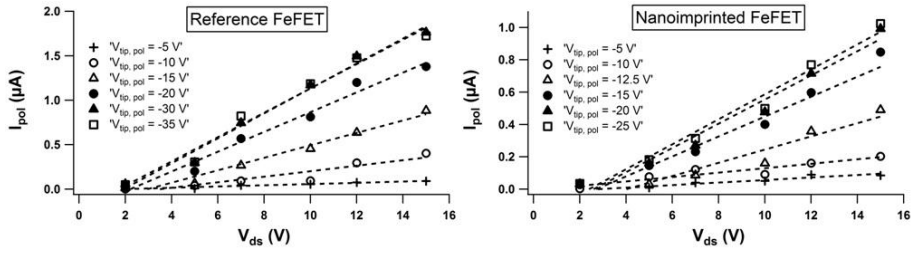

Figure 4.5: Polarization-induced current I_{pol} (upon removal of $V_{tip,\,pol}$) versus V_{ds}, for a reference and a nanoimprinted FeFET. The tip electrode scanning size for both FeFETs was 50 µm x 50 µm. Because the fill factor of the mold is 0.5, the equivalent active area is 25 µm x 25 µm for the nanoimprinted FeFET.

Fig. 4.5 shows the output characteristics of a reference and a nanoimprinted FeFET. I_{pol} increases linearly with increasing V_{ds} for source-drain voltages lower than 15 V, for both FeFETs. The different curves coincide for poling voltages -$V_{tip,\,pol}$ larger than 30 V for the reference FeFET and larger than 20 V for the nanoimprinted FeFET, confirming that the maximum P_r is reached for $V_{tip,pol}$ = -30 V and -20 V for the reference and nanoimprinted FeFET, respectively.

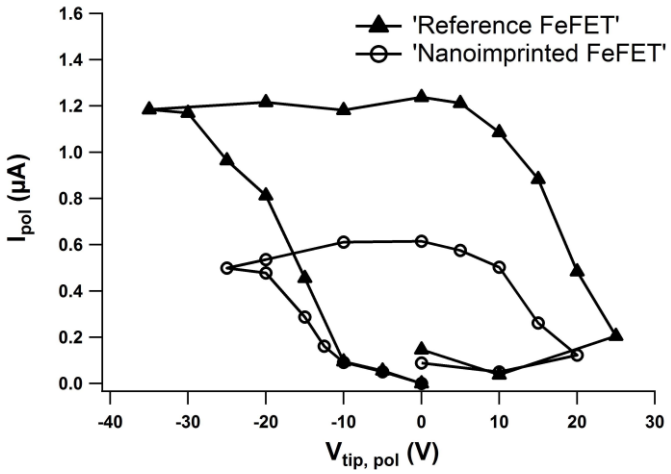

Figure 4.6: Transfer characteristics of a reference and a nanoimprinted FeFET. The polarization-induced current I_{pol} was measured at V_{ds} = 10 V upon removal of $V_{tip,\,pol}$. The tip electrode scanning size for both FeFETs was 50 µm x 50 µm. Because the fill factor of the mold is 0.5, the equivalent active area is 25 µm x 25 µm for the nanoimprinted FeFET. The measurement was started at $V_{tip,pol}$ = 0 V, performed with a clockwise sequence, and finished again at $V_{tip,pol}$ = 0 V.

Fig. 4.6 presents the transfer characteristics with a clear hysteresis for both the reference and the nanoimprinted FeFETs. I_{pol} increases with decreasing $V_{tip,pol}$ starting from 0 V, and saturates below $V_{tip,pol}$ = -30 V and -20 V for the reference and nanoimprinted FeFET, respectively. This again confirms that the maximum polarization is reached faster for the nanoimprinted FeFET, which is consistent with the previous observation : the minimum $V_{tip,pol}$ needed to obtain the saturation value of I_{ds} is decreased by a factor of *ca.* 1.5 in the imprinted FeFET. This reduction is a significant improvement for the performance of the FeFET memory. When sweeping back $V_{tip,pol}$ (Fig. 4.6), I_{pol} keeps its saturation until $V_{tip,pol}$ reaches 15 V for the reference FeFET and 10 V for the nanoimprinted FeFET. At this stage, I_{pol} starts to decrease, due to the switching of the direction of the P(VDF-TrFE) dipoles. Above $V_{tip,pol}$ = 25 V and 20 V for the reference and

nanoimprinted FeFETs, respectively, I_{pol} goes back close to its initial 0 value, corresponding to a random orientation state for the dipoles of P(VDF-TrFE). The lack of permanently aligned polarization after the application of a positive $V_{tip,pol}$ is due to the depolarization of the ferroelectrics in the absence of stabilizing negative charges in the p-type semiconductor layer, resulting in I_{pol} close to 0. (see Supporting Information for the demonstration and comment of the depolarization of the ferroelectrics after application of a positive poling voltage, Fig. 4.7)

We noticed that the saturation value of I_{pol} and the ON/OFF current ratio for the reference FeFET are *ca.* 2.5 times larger than those of the nanoimprinted FeFET. This is because the active area of the nanoimprinted FeFET is half of that of the reference FeFET, since the fill factor of the mold is 0.5 (the defects of nanoimprinted P(VDF-TrFE) shown in Fig. 4.3 (d) are probably responsible for a supplementary small reduction of current). Therefore, each P(VDF-TrFE) nanowire acts more or less in isolation from its neighbors, showing that the transistor which we made actually consists of a series of nanowire transistors placed in parallel. Hence, the system is potentially suited for a reduction of memory size, possibly down to one single nanowire. This would however require a complex integration of the gate electrodes, which was not attempted here.

Further improvements might be obtained by decreasing the thickness of the ferroelectric nanowires, or increasing the confinement of the polymer to decrease further the coercive field.[57, 58] In parallel, the fill factor of the mold could be increased for maximizing the current; alternatively, selecting a semiconductor of higher mobility would also improve the current. For final integration, the deposition of an insulating layer in the open grooves of the ferroelectric layer should be performed. These possible improvements will be investigated in further work.

4.4 Conclusions

We have integrated NIL in the fabrication process of a top-gate bottom-contact organic FeFET. A buried source-drain substrate was designed for the fabrication process. P(VDF-TrFE) imprinted in complete confinement on top of PTAA showed a decreased switching field compared to a continuous reference. In addition, the electric field needed to maximize the remnant polarization P_r was significantly decreased by a factor of *ca.* 1.5 compared to a continuous film. A current characterization was performed by using a conductive PFM cantilever as gate electrode. Our results show that the nanoimprinted FeFET needs a smaller gate voltage to reach the maximum polarization-induced current, compared to the homogeneous reference. This leads to a decreased operating voltage for the memory application. Since our fabricated transistor consists of a large number of nanowire-gated transistors placed in parallel, it also offers interesting possibilities for a strong size reduction of organic FeFETs.

4.5 Supporting Information

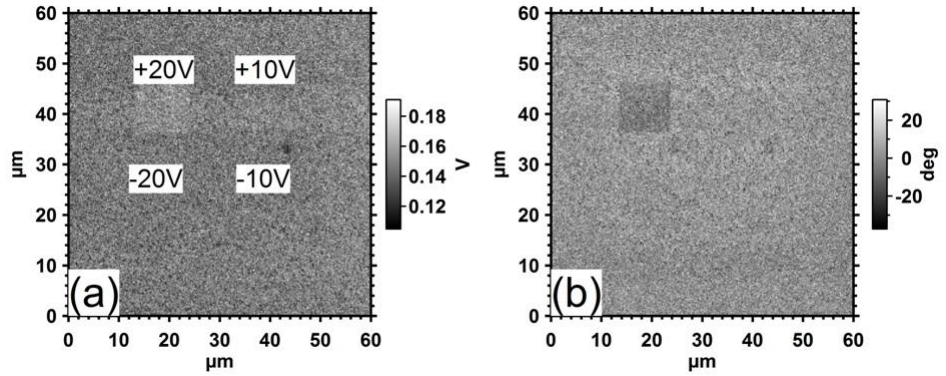

Figure 4.7: PFM piezoresponse (a) amplitude image and (b) phase image of the nanoimprinted P(VDF-TrFE) in a nanoimprinted FeFET. In both images the background was polarized initially with a dc voltage of 0 V, and the smaller square areas of 10 µm x 10 µm were polarized with different dc voltages $V_{s\&d}$ (indicated in the amplitude image) applied on source and drain electrodes. Both images were recorded with a 0 V dc voltage. These two images show that the P(VDF-TrFE) in our device can only be polarized by applying a negative poling voltage $V_{tip,pol}$ ($V_{tip,pol} = V_{gs} = V_{tip} - V_{s\&d} = -V_{s\&d}$) and that this $V_{tip,pol}$ should be large enough ($V_{tip,pol} = -V_{s\&d} = -20$ V); there is only a minor contrast (small squares are not visible) when applying a positive $V_{tip,pol}$ of 20 V and 10 V. This indicates that a positive $V_{tip,pol}$ cannot polarize permanently P(VDF-TrFE) on a PTAA layer: the dipoles go back to a depolarized state when the poling voltage is removed, due to the lack of negative free carriers in p-type PTAA.

Chapter 5

Organic Ferroelectric/Semiconducting Nanowire Hybrid Layer for Memory Storage

Abstract. Ferroelectric materials are important components of sensors, actuators and non-volatile memories. However, possible device configurations are limited due to the need to provide screening charges to ferroelectric interfaces to avoid depolarization. In this chapter, we show that, by alternating ferroelectric and semiconducting nanowires over an insulating substrate, the ferroelectric dipole moment can be stabilized by injected free charge carriers accumulating laterally in the neighboring semiconducting nanowires. This lateral electrostatic coupling between ferroelectric and semiconducting nanowires offers new opportunities to design new device architectures. As an example, we demonstrate the fabrication of an elementary non-volatile memory device in a transistor-like configuration, of which the source-drain current exhibits a typical hysteretic behavior with respect to the poling voltage. The potential for size reduction intrinsic to the nanostructured hybrid layer offers opportunities for the development of strongly miniaturized ferroelectric and piezoelectric devices.[*]

[*] Results in this chapter were published in Nanoscale, 8, 5968-5976 (2016)

5.1 Introduction

When a ferroelectric material is poled by a sufficiently strong electric field, its permanent dipole moments align in the direction of the field, thereby creating a surface charge at the ferroelectric interface. However, when the poling field is removed, the created surface charge must be screened or effectively reduced to decrease polarization energy.[162] In ferroelectric capacitors, screening typically occurs by the accumulation of charges of opposite sign in the metallic electrodes deposited on the ferroelectric interfaces;[161] however, in the absence of such electrodes, the ferroelectric material depolarizes, resulting in the appearance of a large number of very small randomly-oriented ferroelectric domains.[18] This depolarization process limits the possible configurations for functional devices, *e.g.*, ferroelectric memory devices, since these devices use the orientation of the dipole moment to permanently store information. Here, we show that stable polarization states can also be obtained in a hybrid ferroelectric/semiconducting layer consisting of alternating ferroelectric and semiconducting nanowires. We then demonstrate the interest of such hybrid layers by integrating them into a basic organic non-volatile memory device in a transistor-like architecture having a strong potential for size reduction.

In ferroelectric memories, the storage capability is realized by two opposite directions of the remnant polarization of the ferroelectric component which are associated to bits 1 and 0. In ferroelectric capacitors, reading involves the destructive measurement of the flow of screening charges transferred between the bottom and top metallic electrodes when the polarization is switched. Organic non-volatile memory devices with a non-destructive reading operation have also been realized by co-integrating ferroelectric and semiconducting polymers, either in stacked layers as in ferroelectric field-effect transistors (FeFETs),[10, 12-16, 18, 19, 112-114, 167-169] or in mixed layers as in blend diodes;[11, 101-103, 105, 111, 175] more recently, the electrostatic coupling between co-integrated ferroelectric and semiconducting

polymers has even been used to enhance the efficiency of organic solar cells.[176-179]

In a classical FeFET (Fig. 5.1 (a)), a ferroelectric layer is used as gate dielectric. In the 'on' state, this layer is polarized by applying a proper gate voltage depending on the type of the semiconductor, resulting in the presence of negative or positive polarization charges in the ferroelectric material at the ferroelectric/semiconductor interface. Therefore, charge carriers accumulate in the semiconducting layer to screen the polarization charges, leading to a lower channel resistance and to a high 'on' value of the source-drain current. In the low-current 'off' state, the ferroelectric layer is partially depolarized or unpolarized due to the dearth of charge carriers of proper sign in the semiconductor layer.[20] In these standard devices, the polarization charges are thus screened by injected free charges in contact with the planar polarized ferroelectric interface.

In a ferroelectric diode based on phase-separated ferroelectric-semiconductor blends (Fig. 5.1 (b)), the blends are sandwiched between the top and bottom electrodes, creating semiconducting channels running from bottom to top through the continuous phase of the ferroelectric. The permanent polarization of the ferroelectric material is achieved by applying a large enough electrical field between the two electrodes. Here again, screening charges are provided by metal electrodes in direct contact with the polarized ferroelectric interface.

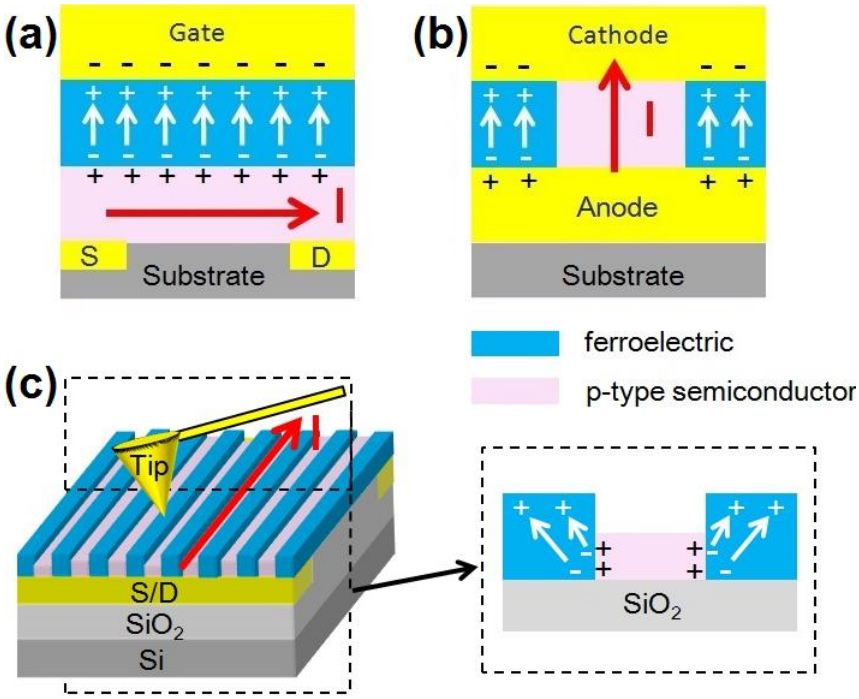

Figure 5.1: Idealized schemes of the configuration and location of the screening charges in different types of non-volatile memory devices based on ferroelectric P(VDF-TrFE) and p-type semiconductor. (a) Poled standard memory FeFET in its 'on' state. (b) Poled memory blend diode. (c) New hybrid transistor in its 'on' state, consisting of alternating ferroelectric P(VDF-TrFE) and semiconducting PTAA nanowires. A conductive AFM tip is used as mobile top gate electrode. The 'off' state of a FeFET or a ferroelectric diode has been shown in previous chapters and the 'off' state of the new hybrid transistor will be shown in details afterwards in this chapter.

In the present work, we design a new configuration, based on a ferroelectric-semiconductor hybrid layer integrated in the architecture of an organic hybrid transistor (Fig. 5.1 (c)). In this hybrid transistor, the ferroelectric polymer layer is shaped by nanoimprint lithography into nanowires separated by channels of a semiconducting polymer. With this new configuration, we demonstrate screening of the polarization charges of the ferroelectric material by

laterally-accumulated charges in the neighboring semiconducting channels. This lateral accumulation results in the formation of conducting channels in the semiconducting nanowires, whose conductance becomes modulated by the polarization state of the ferroelectric nanowires, leading to the fabrication of a new type of non-volatile memory configuration. Although presented in the context of a memory device for convenience, our aim is first and foremost to demonstrate the possibility to generate stable polarization states in a lateral nanowire configuration, which opens new perspectives for the fabrication of a range of ferroelectrics-based devices.

5.2 Experimental

Materials. P(VDF-TrFE) copolymer (65 wt% of VDF, M_w = 300 000 g/mol, Fig. 5.1 (d)) was provided by Solvay Specialty Polymers. PTAA was purchased from Flexink. P(VDF-TrFE) was dissolved in acetylacetone (35 or 45 g/L) and PTAA was dissolved in toluene (5 g/L). All solutions were filtered through PTFE filters with pore sizes of 0.45 µm before spin-coating.

Sample Fabrication. A planar substrate with buried interdigitated source-drain electrodes was used. Source-drain electrodes were defined by standard photolithography on a Si (100) substrate covered by 200 nm of thermally-grown SiO_2, followed by the local vertical etching of 30 nm SiO_2, the deposition of 5/25 nm Cr/Au, and metal lift-off. The channel length and the channel width are 2 µm and 31 mm, respectively. The 35 or 45 g/L P(VDF-TrFE) solution was spin-coated at proper speeds on this substrate to obtain a P(VDF-TrFE) film of *ca.* 98 nm for the mold with lines of *ca.* 200 nm width, 400 nm period, and 200 nm depth or of *ca.* 165 nm for the mold with lines of *ca.* 200 nm width, 1200 nm period, and 200 nm depth. These films were nanoimprinted with an Obducat imprinter at 60 bar and 135 ℃ (in-between the Curie transition and the melting point of P(VDF-TrFE)) with the mold line direction placed normal to the

source-drain direction. After 10 min imprinting time, the system was cooled to room temperature. The initial thickness of the P(VDF-TrFE) layer was selected to be *ca.* 98 nm or *ca.* 165 nm in order to ensure nanoimprinting in complete confinement, resulting in the formation of effectively isolated P(VDF-TrFE) nanowires of *ca.* 200 nm or 1000 nm width, 200 nm opening and 200 nm height, and fully open trenches separating two P(VDF-TrFE) nanowires. The PTAA solution in toluene (5 g/L concentration) was spin-coated at proper speeds on the nanoimprinted P(VDF-TrFE) layer, resulting in the deposition of typically 80-100 nm PTAA between the ferroelectric nanowires and of 10-15 nm PTAA atop them.

Sample Characterization. The height profiles of the PTAA layer and of the P(VDF-TrFE) layer were characterized by atomic force microscopy (AFM) in tapping mode with a silicon cantilever (PPP-NCHR from Nanosensors): devices at different stages of the fabrication process were scratched down to the SiO_2 layer, and the topography of the sample was measured taking the bottom of the scratch as reference for height. From the obtained topographic profiles averaged over a series of stripes, the complete vertical architecture of the organic layer was reconstructed. The piezoresponse of the hybrid layer was checked by PFM (Piezoresponse Force Microscopy, Bruker Icon Dimension) in contact mode. The source-drain electrodes were used as bottom electrodes. A Boron-doped diamond-coated conductive Si cantilever (CDT-CONTR from Nanosensors) was used as a scanning top gate electrode. The ferroelectric response was characterized in PFM imaging mode with an oscillating ac voltage of 1.5 V amplitude, with no added dc bias. All PFM measurements were done by applying the ac driving bias V_{tip} on the cantilever, while the poling was done by applying a dc bias $V_{s\&d}$ on the source-drain electrodes while scanning the grounded tip. The current characterization of the device was performed with a Keithley analyzer (Model 6430). The source-drain current I_{ds} was measured upon removal of the poling gate voltage for a fixed value of source-drain voltage V_{ds}.

5.3 Results and discussion

Well-defined ferroelectric nanowires of 200 nm width and 200 nm interwire opening, or 1000 nm width and 200 nm opening, were fabricated over a perpendicular array of metallic electrodes buried in insulating SiO_2, by nanoimprinting P(VDF-TrFE) in its paraelectric phase;[57, 58, 163] the imprinting parameters described in the Experimental section were selected so as to open fully the P(VDF-TrFE) film between the wires. Subsequently, semiconducting poly(triarylamine) (PTAA) was spin-coated over the nanoimprinted layer to fill the trenches between P(VDF-TrFE) nanowires; PTAA was selected for this work owing to its good stability in air and easy processing conditions resulting from its amorphous nature. The characterization of the vertical structure of the resulting hybrid layer was performed by AFM. Fig. 5.2 (a, b) shows typical topography images of the samples with PTAA nanowires of 200 nm width and P(VDF-TrFE) nanowires of (a) 200 nm or (b) 1000 nm width. The P(VDF-TrFE) lines are not fully continuous due to partial tearing upon demolding; however, this issue does not affect the qualitative behavior of our system, and we did not attempt to improve it in this work. Well-formed nanostructures can still be observed after the deposition of the PTAA layer, indicating that P(VDF-TrFE) nanowires are preserved upon exposure to the toluene PTAA solution.

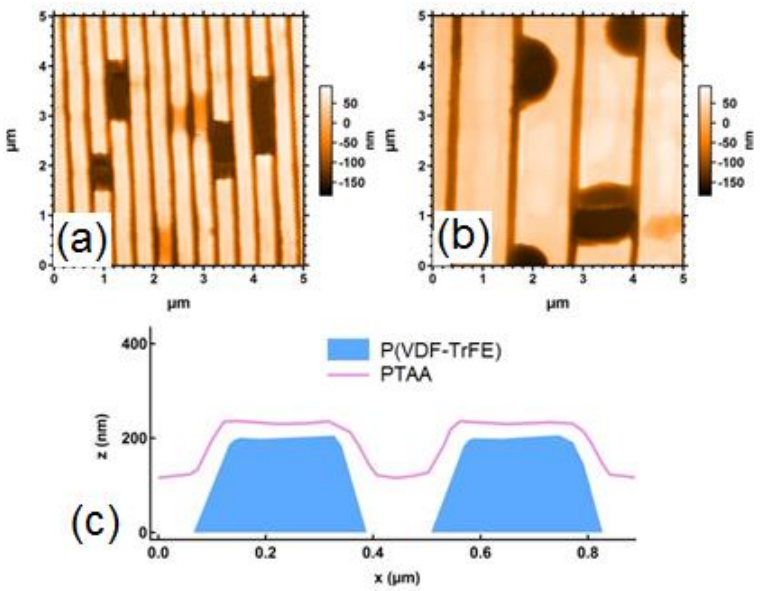

Figure 5.2: AFM topography and reconstructed height profile of the hybrid layer. (a) AFM topography of a sample after spincoating PTAA on nanoimprinted P(VDF-TrFE) nanowires of 200 nm width and 200 nm height. (b) AFM topography of a sample after spincoating PTAA on nanoimprinted P(VDF-TrFE) nanowires of 1000 nm width and 200 nm height. (c) Reconstructed average height profile of the hybrid layer for the sample in panel a, based on AFM measurements performed with the SiO_2 substrate taken as absolute height reference. The sample in panel b has a similar height profile as in panel a, except that the width of P(VDF-TrFE) nanowires is 1000 nm.

The complete vertical profile of the hybrid layer was then reconstructed from AFM measurements, as described in the Experimental section. Fig. 5.2 (c) shows the sample with P(VDF-TrFE) and PTAA nanowires of 200 nm width. The PTAA accumulates between and onto the nanowires of P(VDF-TrFE). The PTAA layer atop P(VDF-TrFE) nanowires plays an important role in the poling of P(VDF-TrFE) and in the signal acquisition when imaging the sample by PFM. One previous report[180] (also presented in Fig. 5.10 of Supporting Information) shows that a P(VDF-TrFE) layer covered on

one side by a PTAA layer can be fully polarized by applying a sufficient high poling voltage when the PTAA is in its accumulation state, but is partially polarized or unpolarized depending on the PTAA layer thickness when PTAA is depleted. Nevertheless, considerably large polarization values can still be obtained when the PTAA layer thickness is smaller than 20 nm. In addition, Fig. 5.11 (Supporting Information) shows that the PFM contrast effectively decreases with increasing PTAA layer thickness when the PTAA layer is lying in between the P(VDF-TrFE) layer and the conductive PFM tip. Therefore, to limit vertical depolarization and contrast dampening, a 5 g/L PTAA solution was chosen in the fabrication of our device, thereby avoiding the formation of a thick semiconducting layer atop the ferroelectric nanowires; with this solution and properly selected spin-coating conditions, only a very thin PTAA layer of *ca.* 10-15 nm rests on the 200 nm high P(VDF-TrFE) nanowires, while a *ca.* 80-100 nm thick PTAA nanowire is formed in the trenches between the P(VDF-TrFE) nanowires (Fig. 5.2 (c)). The optimization of the PTAA layer thickness atop the P(VDF-TrFE) nanowires under different conditions is shown in Fig. 5.14 of the supporting information.

The switching behavior of the ferroelectric nanowires in the hybrid layer resting over an array of perpendicular metal electrodes buried into a SiO_2 layer was then studied by PFM: small regions of the sample were first poled by scanning the grounded tip while applying a 20 V or -20 V dc voltage simultaneously to the source and drain metallic electrodes ($V_{s\&d}$). The sample was then imaged in PFM mode at zero dc bias. When interpreting these images, one should be aware that the roughness of the layer, combined with its hybrid ferroelectric/semiconducting nature, results in values of PFM amplitude and phase which considerably deviate from ideality. The PFM contrast is also weaker compared to the one of a pure P(VDF-TrFE) film, due to the presence of the thin PTAA layer atop the P(VDF-TrFE) nanowires as pointed out before. In the sequel, unless mentioned otherwise, all PFM images are obtained on the sample having P(VDF-TrFE) and PTAA nanowires both of 200 nm width, as shown in Fig. 5.2 (a).

Fig. 5.3 (a, c) shows PFM amplitude and phase images of the hybrid layer after downward poling at $V_{s\&d}$ = -20 V. The hybrid structure consisting of lines oriented perpendicularly to the electrodes is clearly seen. A strong contrast is observed both in PFM phase and amplitude for P(VDF-TrFE) lying atop the Au electrodes, compared to regions that were not poled; however, no contrast appears for poled P(VDF-TrFE) lying over the SiO_2 regions separating the buried electrodes. This indicates that the P(VDF-TrFE) dipoles align during poling, and remain aligned upon removal of the poling voltage when lying over the conducting metallic electrodes; in contrast, the ferroelectric material lying over the insulating SiO_2 regions has a globally randomly-oriented polarization state after poling. The images also confirm that the thin PTAA layer remaining atop the P(VDF-TrFE) nanowires does not prevent to pole the ferroelectric material and to obtain a sufficiently clear PFM contrast.

Fig. 5.3 (b, d) shows PFM amplitude and phase images of the hybrid layer when a positive 20 V source and drain voltage was applied prior to the PFM measurement. A strong contrast can now be observed in PFM phase and amplitude for P(VDF-TrFE) irrespective of its location over Au electrodes or SiO_2 regions. This indicates that the P(VDF-TrFE) dipoles are aligned over the full poled area after removal of the positive upward poling voltage; hence, the ferroelectric material does not depolarize, even when resting over insulating regions although they cannot provide screening charges.

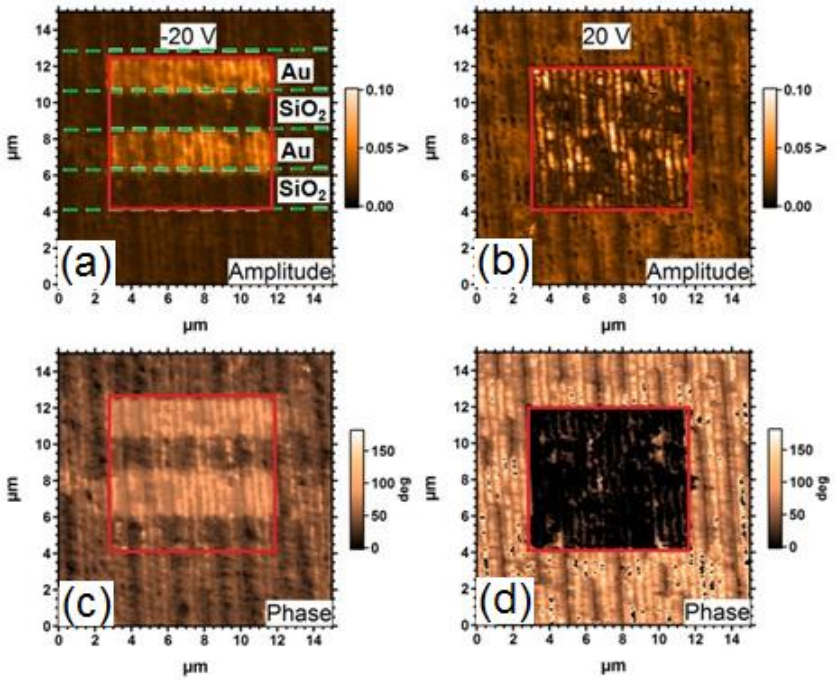

Figure 5.3: PFM piezoresponse of a hybrid P(VDF-TrFE)/PTAA layer. (a,b) are amplitude images, and (c,d) are phase images of the same region of the transistor. The buried Au electrodes and interspersing SiO_2 regions lying below the hybrid layer are indicated in panel (a) by green dashed lines. In all the images the background was scanned initially with a dc voltage of 0 V, and smaller square areas of 8 µm x 8 µm (red-boxed in the images) were polarized by scanning the grounded tip while applying a 20 V (b, d) or -20 V (a, c) dc voltage on source and drain electrodes ($V_{s\&d}$). PFM images were subsequently recorded by applying a 1.5 V ac voltage on the tip and a 0 V dc voltage on sorce and drain electrodes.

As mentioned above, in order for a ferroelectric material to be stable after poling, compensating charges must be provided at its interface to suppress the depolarizing field resulting from its polarization. When P(VDF-TrFE) is poled over a bottom Au electrode, compensating charges are easily provided at the bottom interface by the free carriers of the metal (electrons or holes, depending on the sign of the polarization). As for the top interface, compensating charges are

probably spurious charged species such as for instance ions from the thin water layer present on free surfaces in air, which act through the very thin 10-15 nm PTAA layer covering P(VDF-TrFE). As a consequence, the P(VDF-TrFE) dipoles remain aligned atop the Au electrodes upon removal of positive or negative poling voltages, resulting in two stable polarization states of P(VDF-TrFE) over these electrodes.

However, the polarization and the stabilization mechanism is different for P(VDF-TrFE) dipoles atop insulating SiO_2. Compensating charges are still provided at the top interface by the same mechanism as in the case of Au; however, because SiO_2 is insulating and thick, no compensating charges can be provided at the bottom interface. Hence, P(VDF-TrFE) should depolarize upon removal of the poling field (or does not even polarize upon application of the poling field), which is indeed the case when $V_{s\&d}$ = -20 V: the P(VDF-TrFE) dipoles are in randomly-oriented domains of very small size upon removal of the poling voltage, resulting in a globally non-oriented P(VDF-TrFE) polarization state with no PFM contrast (Fig. 5.5 (a)). However, for $V_{s\&d}$ = +20 V, the field-aligned P(VDF-TrFE) dipoles are stabilized, as demonstrated by the PFM contrast which is preserved upon removal of the polarizing field. This can only be due to the holes injected in the p-type PTAA accumulating laterally at the P(VDF-TrFE)/PTAA interface as drawn schematically in Fig. 5.5 (b). This charge injection occurs during poling, and results in a stable P(VDF-TrFE) polarization state upon removal of the poling voltage.

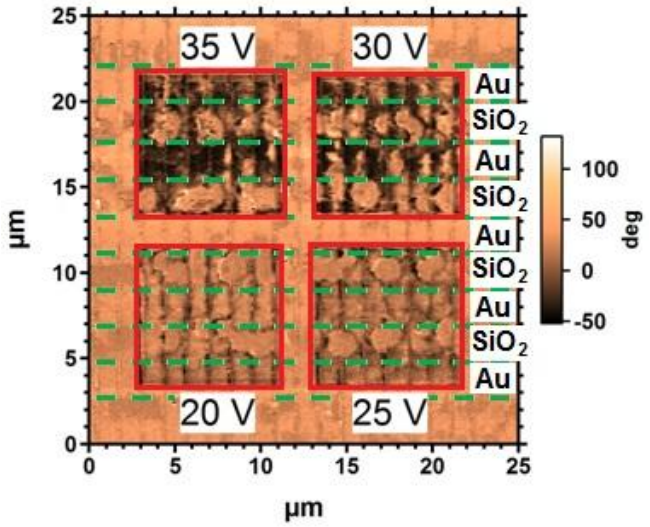

Figure 5.4: PFM phase image of a hybrid P(VDF-TrFE)/PTAA nanowires layer. The width of the P(VDF-TrFE) and PTAA nanowires is 1000 nm and 200 nm, respectively. Four small regions of 8 µm x 8 µm (red-boxed) were polarized by scanning the grounded tip while applying a 20 V, 25 V, 30 V, and 35 V dc voltage on source and drain electrodes ($V_{s\&d}$). The PFM phase image was subsequently recorded by applying a 1.5 V ac voltage on the tip and a 0 V dc voltage on source and drain electrodes. The locations in poled regions showing a minor contrast compared to the unpoled region are nanoimprinting defects as shown in Fig. 5.2 (b).

To estimate to what extent this lateral charge accumulation can screen the polarization charges, we studied at different poling voltages a sample with wider P(VDF-TrFE) nanowires (1000 nm instead of 200 nm, topography shown in Fig. 5.2 (b)). Fig. 5.4 presents the PFM phase images of such a sample; unfortunately, the sample suffered from increased adhesion problems resulting in larger defects. At 20 V, the contrast over SiO_2 appears only in a limited region at the edges of the P(VDF-TrFE) nanowires, indicating that the stable polarization is only obtained at the edges close to the P(VDF-TrFE)/PTAA interface where lateral charge accumulation occurs. This is most probably because the coercive field of P(VDF-TrFE) is not reached on farther

away positions under a 20 V poling voltage. With increasing poling voltage, the width of poled regions increases and covers a substantial portion of the P(VDF-TrFE) nanowires for voltages larger than 30 V, because the coercive field of P(VDF-TrFE) can be reached at a larger distance from the P(VDF-TrFE)/PTAA interface with larger poling voltages. Hence, we conclude that lateral hole accumulation at the P(VDF-TrFE)/PTAA interface is able to stabilize the dipole moments of our P(VDF-TrFE) nanowires over a significant distance, even over the complete nanowire for the case of sub-micrometer widths, provided the amplitude of the poling voltage be large enough. Nanowires of 200 nm width are sufficiently narrow to be polarized on the whole region by applying a 20 V poling voltage, as indeed demonstrated in Fig. 5.3 (b, d).

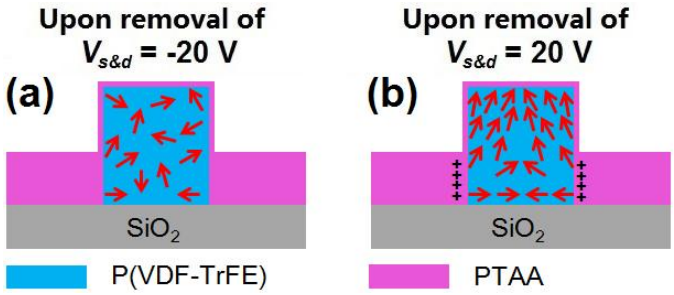

Figure 5.5: Sketch of P(VDF-TrFE) polarization states atop SiO_2 in the hybrid nanostriped layer. (a) Depolarized/unpolarized state upon removal of a downward-poling voltage (V_{tip} = 0, $V_{s\&d}$ = -20 V). (b) Laterally-screened polarized state upon removal of an upward-poling voltage (V_{tip} = 0, $V_{s\&d}$ = 20 V). Arrows indicate the idealized direction of the dipole moments and the polarization of P(VDF-TrFE); the lateral accumulation of holes in the PTAA to stabilize the polarization charges is also shown in panel b. Screening charges at the top of the ferroelectric nanowires are not shown in this sketch; they are most probably provided by adsorbed ions as commonly found for PFM in air.

Fig. 5.6 shows the operational switching between the two states of Fig. 5.5. In Fig. 5.6 (a), the hybrid layer was first poled by a

downward-poling voltage (V_{tip} = 0, $V_{s\&d}$ = -20 V) over a larger region boxed in green, in which the PFM phase contrast indicates that the P(VDF-TrFE) polarization is in a randomly-oriented state. Then, within this larger region, a smaller region boxed in red was poled by an upward-poling voltage (V_{tip} = 0, $V_{s\&d}$ = 20 V) over which the PFM phase contrast shows a stable polarization state screened by holes accumulating laterally as described above. In Fig. 5.6 (b), the reverse poling operations were performed, resulting in a laterally-screened polarization state after upward poling over a larger region (green-boxed), and in a randomly-oriented polarization state resulting from downward poling over a smaller region (red-boxed). Hence, Fig. 5.6 proves that each polarization state of the P(VDF-TrFE) nanowires can be switched into its opposite by proper poling.

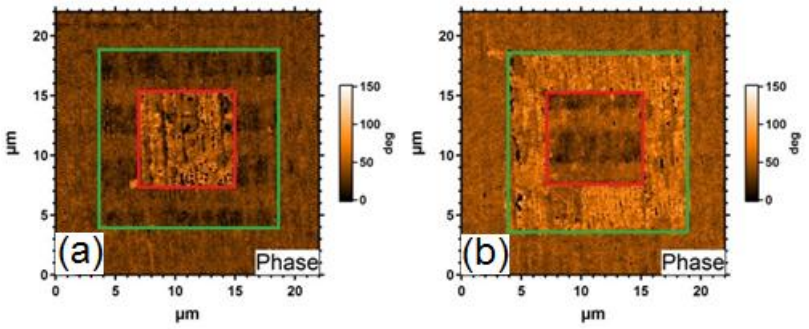

Figure 5.6: PFM phase images of the local switching of the ferroelectric nanowires in the hybrid layer. (a) The system was first poled at $V_{s\&d}$ = -20 V over a larger region (15 µm x 15 µm, green-boxed) and then poled at $V_{s\&d}$ = 20 V over a smaller region (8 µm x 8 µm, red-boxed); (b) the system was first poled at $V_{s\&d}$ = 20 V over a larger region (15 µm x 15 µm, green-boxed) and then poled at $V_{s\&d}$ = -20 V over a smaller region (8 µm x 8 µm, red-boxed.).

The lateral screening of the polarization charges should only be operative if charge carriers of proper polarity are available in the neighboring semiconducting nanowires. In the case of the hybrid layer discussed so far, it does not happen for negative poling voltages, since

it would then require the accumulation of electrons at the P(VDF-TrFE)/PTAA interface, which is not possible due to the p-type nature of PTAA. To test this hypothesis, PTAA was also replaced in the hybrid layer by either p-type 2,7-dioctyl[1]benzothieno[3,2-b][1] benzothiophene (C8-BTBT) or n-type poly(benzimidazobenzophenanthroline) (BBL) organic semiconductors. The results, shown in the Supporting Information (Figures 5.12-5.13), fully support this explanation, with the p-type C8-BTBT-based hybrid layer behaving exactly like the p-type PTAA-based hybrid layer, whereas the n-type BBL-based hybrid layer displays an opposite behavior, with depolarization of the ferroelectric nanowires occurring over insulating SiO_2 regions when $V_{s\&d}$ = +20 V, and conservation of the polarization state when $V_{s\&d}$ = -20 V. This fully confirms that the screening charges are provided by the semiconductor, and are thus acting (during and after poling) by lateral accumulation as displayed in Fig. 5.5 (b).

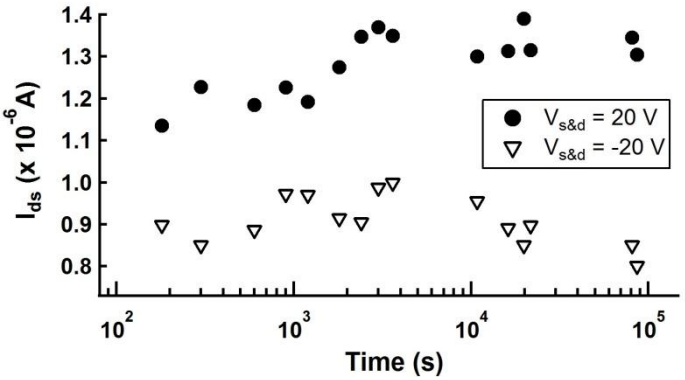

Figure 5.7: Source-drain current for the two polarization states of the hybrid layer, measured versus time after removal of the poling voltage.

To further prove this hypothesis, the source-drain current was measured at these two polarization states (poling area: 50 µm x 50 µm). As shown in Fig. 5.7, when the polarization state is screened by lateral free charges injected in the PTAA ($V_{s\&d}$ = 20 V), a higher

current value is obtained, proving that the lateral accumulation of charges results in the formation of a channel of higher conductance. In contrast, the depolarized state after poling by $V_{s\&d}$ = -20 V results in a lower current value, because no free charges accumulation occurs due to the randomly-oriented polarization of the P(VDF-TrFE) nanowires. In addition, these two current values keep almost unchanged over one day, demonstrating that the two corresponding polarization states are stable over a long time.

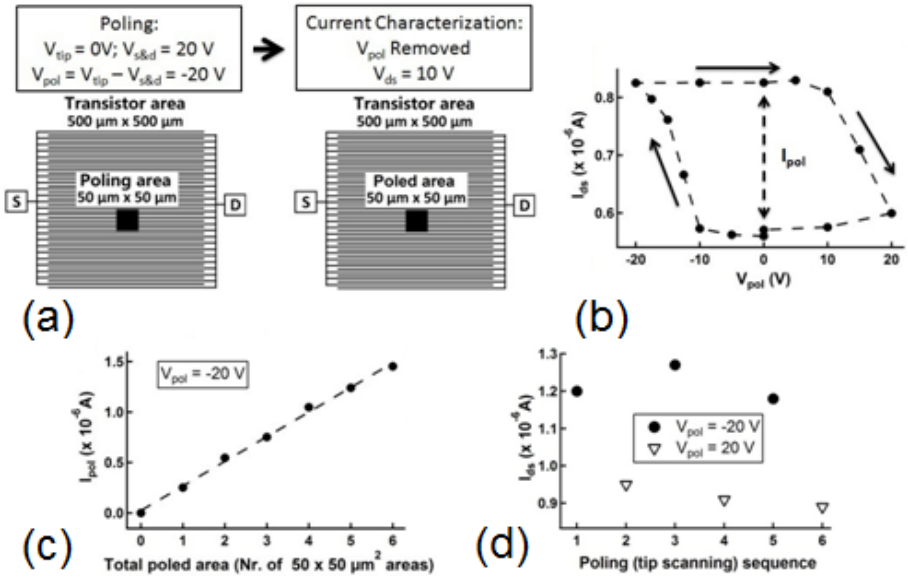

Figure 5.8: Current characterization of the hybrid transistor. (a) Scheme of the polarization and current measurement of the device. The scheme shows the size of one standard poling area (50 µm x 50 µm) and one poling scenario with V_{pol} = -20 V. (b) Source-drain current I_{ds} (measured after poling one standard area by the application of V_{ds} = 10 V) versus previously-applied poling voltage V_{pol}. Starting from 0 V, the arrows show the time sequence of V_{pol}. The polarization-induced current I_{pol} for one standard poled area is also defined in the graph. (c) Polarization-induced current I_{pol} versus the total poled area. The total poled area is expressed as the number of standard poling areas. Each standard area corresponding to a different poling scan in the AFM. (d) Source-drain current I_{ds} (measured after poling one standard area at V_{pol}, followed by removal of V_{pol} and application of V_{ds} = 10 V) for a sequence of poling voltages of opposite polarity (V_{pol} = -20 V and 20 V).

This lateral charge screening provides the possibility to design new configurations of functional devices, as we now demonstrate by fabricating an elementary organic non-volatile memory device. It is important to stress that this device was made to illustrate the possibilities afforded by lateral screening of polarization charges and to characterize further the hybrid layer, rather than to compete against state-of-the-art devices made of inorganic ferroelectric materials.

Here, we used the PFM tip as a mobile top electrode, thereby effectively forming a hybrid transistor, which was characterized electrically as described in Experimental section (Fig. 5.8 (a)). As before, the conductive cantilever was used as gate to pole the P(VDF-TrFE). The grounded tip was scanned over a defined area of 50 µm x 50 µm (which is 1/100th of the complete transistor area) while setting $V_{s\&d}$ to a given value, in order to pole the system at V_{pol} (defined as $V_{pol} = V_{tip} - V_{s\&d} = -V_{s\&d}$). Then, the poling tip was removed and the source-drain current I_{ds} was measured at a source-drain voltage V_{ds} of 10 V. The current measurement was performed over the complete transistor area of 500 µm x 500 µm, of which only one part of ca 1/100th had been previously polarized by the tip (due to limitations in our AFM setup). Fig. 5.8 (b) shows the source-drain current I_{ds} versus the value of the previously-applied poling voltage V_{pol}; a clear current hysteresis is observed. The arrows in the graph indicate the time sequence of V_{pol}, starting from 0 V. When the previously-applied poling voltage V_{pol} is larger than -10 V, I_{ds} is low and can be considered to be in the 'off' state. This is because the P(VDF-TrFE) is not polarized by a small poling field, with as a result no electrostatic coupling between P(VDF-TrFE) and PTAA. I_{ds} then increases for V_{pol} = -12.5 V and reaches a maximum I_{on} when V_{pol} = -20 V. This is due to the progressive polarization of P(VDF-TrFE) from -12.5 V on, with the maximum polarization being achieved at -20 V. At this stage, charge carriers have accumulated at the P(VDF-TrFE)/PTAA interface as shown in Fig. 5.5 (b), opening a channel for conduction resulting in a higher current. After reaching this maximum, I_{ds} keeps almost unchanged when the previously-applied poling voltage V_{pol} is progressively increased to 5

V. This is due to the stable polarization of the P(VDF-TrFE) nanowires, with the preservation of the channel of holes accumulated at the P(VDF-TrFE)/PTAA interface. From 10 V on, I_{ds} starts to decrease and comes back to the initial 'off' current state for V_{pol} = 20 V. This indicates that the polarization direction of P(VDF-TrFE) starts to be changed from 10 V on, with the polarization being switched into opposite or random directions depending on the P(VDF-TrFE) position (atop Au or SiO_2) for V_{pol} = 20 V. In this case, no mobile charges accumulate at the P(VDF-TrFE)/PTAA interface, resulting in smaller I_{ds} values. Therefore, two source-drain current states I_{on} and I_{off} can be obtained depending on the previous polarization direction of P(VDF-TrFE), which can be associated to bits 1 and 0 for memory applications.

The larger I_{on} compared to I_{off} is due to the accumulation of holes at the P(VDF-TrFE)/PTAA interface to compensate for the permanent polarization of P(VDF-TrFE), and we define this current increase as the polarization-induced current $I_{pol} = I_{on} - I_{off}$. As noted before, the source-drain current values in Fig. 5.8 (b) were obtained by measuring a hybrid transistor of 500 µm x 500 µm area, whereas the poling area is only 50 µm x 50 µm due to the restricted scanning area of the AFM conductive tip. Therefore, the active area is only 1/100th of the complete transistor area. This explains why the measured I_{pol} is limited (*ca.* 0.27 µA). Therefore, we have poled a larger area by repeating the scanning of the tip over a series of regions of 50 µm x 50 µm, in order to check the influence of the previously-poled area over the polarization-induced current. Fig. 5.8 (c) shows that I_{pol} increases linearly with the total poled area, proving that I_{pol}, and thus the 'on' current, can be increased by poling a larger area. This actually provides a methodology to store more than two values in the memory device, by poling the hybrid layer over an increasing number of standard areas. In Fig. 5.8 (c) for instance, seven different values could be stored in the device. In addition, Fig. 5.8 (c) also indicates that the ferroelectric/semiconducting nanowires can work independently, which provides the potential of strong size reduction of memory device, possibly down to one single

ferroelectric/semiconducting nanowire. The interest of devices including semiconductor nanowires has been shown before,[115, 144, 181-186] but not in conmbination with organic ferroelectric nanowires. Moreover, the on and off currents are stable within one day as shown in Fig. 5.7, which indicates a possible long data storage time. In addition, Fig. 5.8 (d) shows that repeated writing and erasing cycles are possible, promisingly suggesting that the hybrid transistor has a reasonable endurance, although a more extensive characterization would be required to conclude definitively on this point. A further advantage of the device is its non-destructive reading capability resulting from the low values of V_{ds} required for reading.

5.4 Conclusion

Summing up, we have designed a bifunctional nanostriped organic hybrid layer by shaping a ferroelectric polymer into nanowires, followed by filling the separating space by a semiconducting polymer. The proposed methodology leads to the easy creation of well-controlled hybrid nanostructures over intergiditated electrodes buried in silicon oxide. When the ferroelectric nanowires are poled with the proper polarity, the ferroelectric dipole moment can be stabilized by charges accumulating laterally in the semiconducting channels, thereby preventing depolarization even though the ferroelectric material rests over an insulating substrate. This lateral electrostatic coupling between the ferroelectric and the semiconducting material is made possible by the reduction in size of the ferroelectric material. The charge accumulation only occurs for one direction of polarization, due to the p-type nature of the semiconductor, and creates a channel for conduction from source to drain. Changing the type of the semiconductor from p-type to n-type reverses the polarities required for the effect to be obtained.

This new charge compensation mechanism then allowed us to fabricate a new memory device, based on the intrinsic storing/reading

capability of the hybrid nanowire layer. We characterized the source-drain current versus the previously-applied poling voltage, and obtained a current hysteresis with 'on' and 'off' limiting values of the current, of direct interest for memory applications. We also showed that the on/off current ratio scales with the size of the poled region, thereby providing access to a memory containing more than two stored states and possibility to scale down the memory size possibly to one single ferroelectric/semiconducting nanowire. Given the potential for size reduction intrinsic to the nanostriped nature of the hybrid layer, the new physical coupling effect reported here is expected to find applications in strongly miniaturized ferroelectric and piezoelectric devices.

5.5 Supporting Information

5.5.1 Influence of a PTAA layer above or below a P(VDF-TrFE) layer on the ferroelectric polarization and on the PFM signal acquisition

Two sample configurations, as shown in Fig. 5.9, were designed in order to check the influence of a PTAA layer on the ferroelectric polarization and on the PFM signal acquisition.

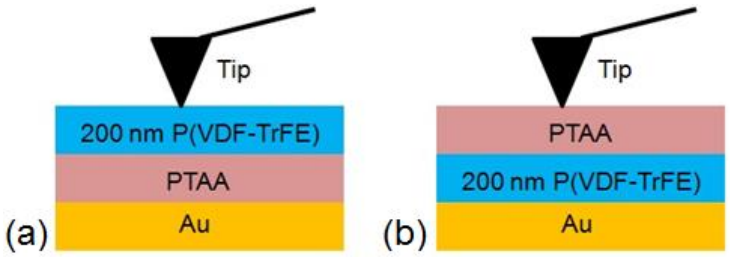

Figure 5.9: Two sample configurations used for PFM measurements. (a) The PTAA layer is below the P(VDF-TrFE) layer. (b) The PTAA layer is atop the P(VDF-TrFE) layer.

5.5.1.1 The PTAA layer is below the P(VDF-TrFE) layer

Fig. 5.10 shows PFM amplitude images corresponding to samples with PTAA layer thicknesses of 0, 5 and 15 nm below a 200 nm thick P(VDF-TrFE) layer. In all images, two small regions (2 x 2 μm^2) were first poled by applying 30 V (left-bottom) or -30 V (right-top) on the conductive tip, while keeping the bottom electrode grounded. The PFM amplitude images were then obtained by scanning the tip on a larger area (6 x 6 μm^2) while applying only an ac bias to the bottom electrode (1.5 V peak-to-peak amplitude) while keeping the tip grounded. The contrasts of PFM amplitude between the positively- or negatively-poled regions and the unpoled background are plotted in Fig. 5.2 (d) as a function of PTAA layer thickness. The PFM amplitude contrast between poled and unpoled regions indicates that P(VDF-TrFE) is well-polarized and that the poled states are stable since the images are taken at zero poling bias well after poling. In these PFM amplitude images, a larger contrast indicates that more dipoles are aligned, with as a consequence a larger remnant polarization.

When the bias applied to the tip (V_{tip}) is -30 V, the contrast keeps almost constant from 0 to 35 nm PTAA layer thickness, proving that the polarization behavior is hardly affected by the semiconducting layer (which is in accumulation state in this case); this is because the accumulation charges have been trapped at the interface and stabilize the ferroelectric polarization. However, the polarization behavior is different when V_{tip} is 30 V, in which case the PTAA layer is depleted. The contrast then decreases with increasing PTAA layer thickness and vanishes for 35 nm PTAA layer thickness. This is because no compensating charges are provided by the depleted PTAA layer; however, the free charges in the remote metal electrode can screen the polarization charges through the PTAA layer, albeit with increasing difficulty as the PTAA layer thickness increases. Nevertheless, considerably large PFM contrasts and polarization values can still be obtained when the PTAA layer thickness is thinner than 20 nm.

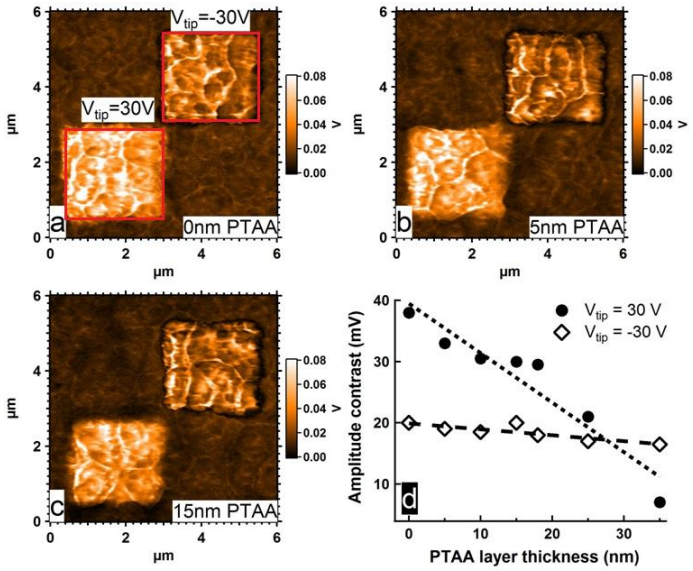

Figure 5.10: PFM amplitude images of the samples with a PTAA layer thickness of (a) 0 nm, (b) 5 nm, (c) 15 nm. On these samples, one small region (2 x 2 μm^2, left-bottom) was poled by applying a 30 V tip bias and the other one (2 x 2 μm^2, right top) a -30 V tip bias, while keeping the bottom electrode grounded. These two regions are boxed in red in (a). The PFM images were subsequently obtained at zero poling voltage over larger areas (6 x 6 μm^2). The PFM amplitude contrasts between these two small regions and the unpoled background are shown in (d). Dashed and dotted lines are guides to the eye.

5.5.1.2 The PTAA layer is above the P(VDF-TrFE) layer

Fig. 5.11 shows PFM amplitude images corresponding to samples with PTAA layer thicknesses of 0, 8 and 15 nm atop P(VDF-TrFE). The PFM poling and imaging conditions were the same as described above. In this case, irrespective of the polarity of the poling voltages, the PFM contrast decreases with increasing PTAA layer thickness and vanishes when the PTAA layer thickness is larger than *ca* 30 nm, even when the PTAA layer is in its accumulation state (V_{tip} = 30 V). By comparison with the results of the reverse configuration (Fig. 5.10), this proves that the PFM signal – not the polarization - is affected due to the presence of the PTAA layer atop the P(VDF-TrFE) layer:

thicker PTAA layers clearly considerably dampen the piezoelectric oscillation of the P(VDF-TrFE) layer.

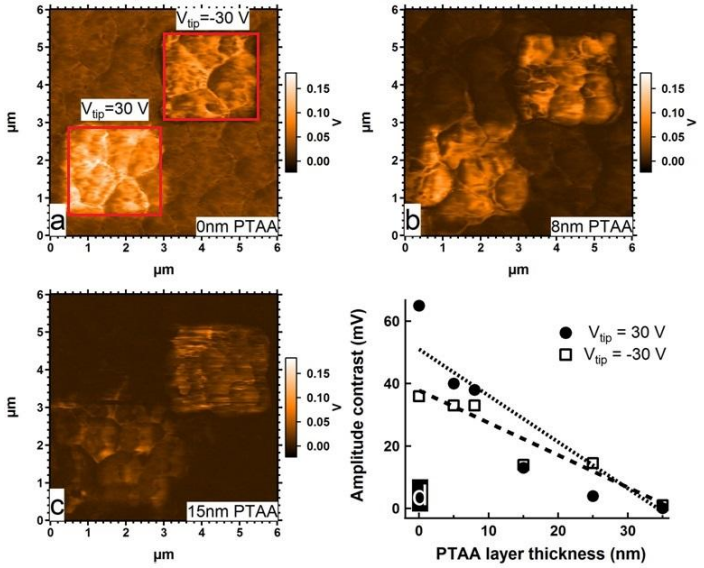

Figure 5.11: PFM amplitude images of the samples with a PTAA layer thickness of (a) 0 nm, (b) 8 nm, (c) 15 nm atop a P(VDF-TrFE) layer. On these samples, one small region (2 x 2 μm^2, left-bottom) was poled by applying a 30 V tip bias and the other one (2 x 2 μm^2, right top) a -30 V tip bias, while keeping the bottom electrode grounded. These two regions are boxed in red in (a). The PFM images were subsequently obtained at zero poling voltage over larger areas (6 x 6 μm^2). The PFM amplitude contrasts between these two small regions and the unpoled background are shown in (d). Dashed and dotted lines are guides to the eye.

5.5.2 PFM measurements performed on nanostriped ferroelectric/semiconducting layers with different types of semiconducting organic materials

5.5.2.1 C8-BTBT

Similarly to PTAA 2,7-dioctyl[1]benzothieno[1]benzothiophene (C8-BTBT, chemical structure shown in Fig. 5.12 (e)) is a p-type semiconductor.[187] Therefore, a hybrid P(VDF-TrFE)/C8-BTBT layer should display a similar behavior as a P(VDF-TrFE)/PTAA-based one,

which is indeed shown in Fig. 5.12. When $V_{s\&d}$ = -20 V, the polarization of P(VDF-TrFE) is preserved only atop Au electrodes, not atop SiO_2 regions due to a lack of compensating electrons in C8-BTBT. When $V_{s\&d}$ = 20 V, the polarization of P(VDF-TrFE) is preserved atop both Au electrodes and SiO_2 regions, because the holes provided by Au and C8-BTBT can stabilize the polarization.

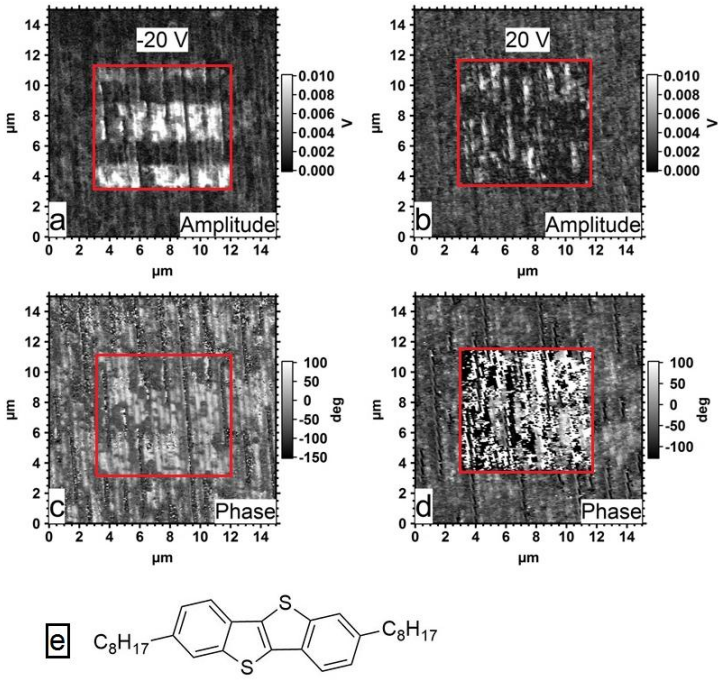

Figure 5.12: PFM piezoresponse ((a,b) amplitude images; (c,d) phase images) of the hybrid P(VDF-TrFE)/C8-BTBT layer. In all the images the background was polarized initially with a dc voltage of 0 V, and smaller square areas of 8 μm x 8 μm (red-boxed in the images) were polarized by scanning the grounded tip while applying a 20 V (b, d) or -20 V (a, c) dc voltage on source-drain electrodes ($V_{s\&d}$). PFM images were subsequently recorded with a 0 V applied dc voltage. The hybrid layer rests over either regions of SiO_2 or Au, as shown in Fig. 5.3 of the companion article. (e) Chemical structure of C8-BTBT. The deposition of the C8-BTBT layer was done by spin-coating a 10 g/L C8-BTBT solution in toluene onto the nanostriped P(VDF-TrFE) and buried S/D substrate at 1500 rpm for 30 s, followed by a subsequent annealing at 120 ℃ for 15 min.

5.5.2.2. BBL

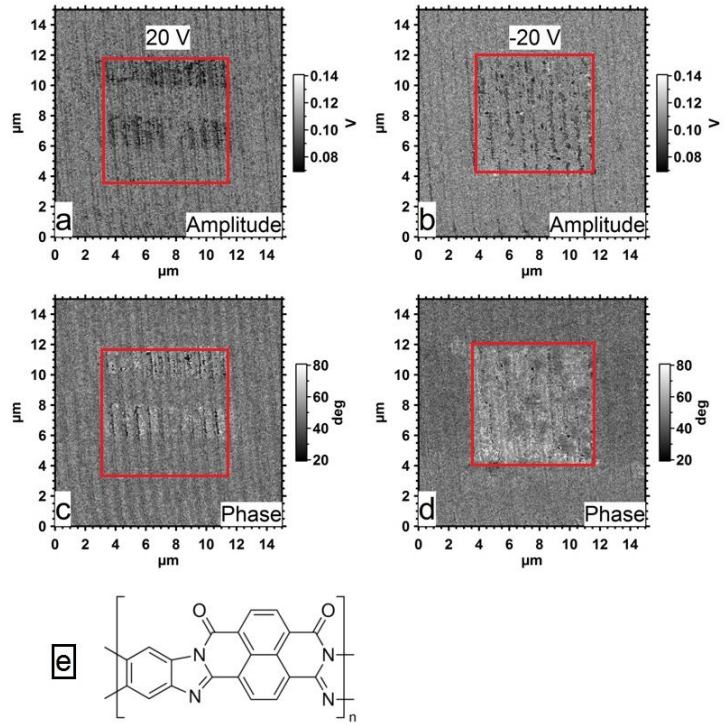

Figure 5.13: PFM piezoresponse ((a,b) amplitude images; (c,d) phase images) of a hybrid P(VDF-TrFE)/BBL layer. In all the images the background was polarized initially with a dc voltage of 0 V, and smaller square areas of 8 µm x 8 µm (red-boxed in the images) were polarized by scanning the grounded tip while applying a 20 V (b, d) or -20 V (a, c) dc voltage on source-drain electrodes ($V_{s\&d}$). PFM images were subsequently recorded with a 0 V applied dc voltage. The hybrid layer rests over either SiO_2 or Au, as shown in Fig. 5.3 of the companion article. (e) Chemical structure of BBL. The deposition of the BBL layer was done by spin-coating a 3 g/L BBL solution in methanesulfonic acid (MSA) onto the nanostriped P(VDF-TrFE) and buried S/D substrate at 1500 rpm for 30 s. Then the sample was put into methanol for 10 min to remove the remaining MSA, followed by a subsequent annealing at 110 ℃ for 10 min.

Poly(benzimidazobenzophenanthroline) (BBL) is a n-type semiconductor[188] which can only provide free electrons. Therefore, the hybrid P(VDF-TrFE)/BBL layer should have a behavior opposite

to the one of a P(VDF-TrFE)/PTAA layer, which is shown in Fig. 5.13. When $V_{s\&d}$ = 20 V, the polarization of P(VDF-TrFE) is preserved only atop Au electrodes, not atop SiO_2 regions due to the lack of compensating holes in BBL. When $V_{s\&d}$ = -20 V, the polarization of P(VDF-TrFE) is preserved atop both Au electrodes and insulating SiO_2 regions, because the electrons provided by Au and BBL can stabilize the polarization. The behavior is indeed reversed compared to the case of a p-type system.

5.5.3 Optimization of the PTAA layer thickness atop P(VDF-TrFE) nanowires

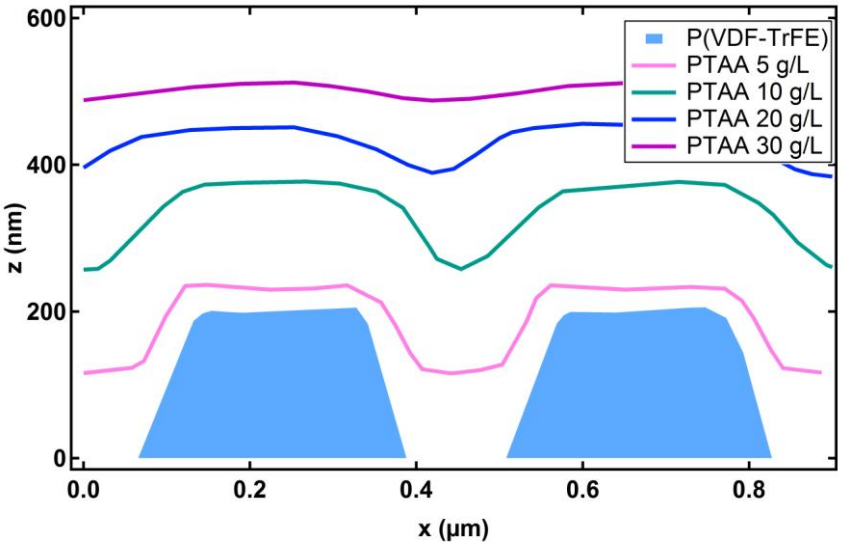

Figure 5.14: Reconstructed average height profile of the hybrid layer for different PTAA solutions spincoated at the same conditions, based on AFM measurements performed with the SiO_2 substrate taken as absolute height reference. The results shown here were obtained on the sample with nanoimprinted P(VDF-TrFE) nanowires of 200 nm width and 200 nm height.

Chapter 6

Nanopatterned Organic-Inorganic Multiferroic Layers

Abstract. Multiferroics exhibiting the magnetoelectric (ME) effect due to the coupling of magnetic and electric ferroic orders are of great importance for both fundamental research and technological applications. The manipulation by an electric field of the magnetism provides an additional degree of freedom to control the magnetic properties of a material, and vice versa. Investigations of ME coupling have been intensively performed on inorganic multiferroic materials. On the other hand, organic multiferroics have been rarely investigated, which is opposite to the increasing demand of organic material-based applications. In addition, most studies have concentrated on the electric control of the magnetism; in contrast, the magnetic control of the electric polarization is less reported, even for inorganic multiferroics. To make progress on the fabrication and ME coupling in organic multiferroics, in this chapter, we set up a methodology to fabricate nanopatterned multiferroic layers based on organic ferroelectric polymers and study the local ME coupling in these layers. We specially focus on the magnetic manipulation of the electric polarization of the polymer in the multiferroic layers, and show how it can be almost fully reversed with a magnetic field by using proper conditions. We also show the importance of relaxation effects in these complex systems.[*]

[*] Manuscript submitted

6.1 Introduction

Multiferroics are materials exhibiting the coexistence of different ferroic orders, such as ferroelasticity and ferroelectricity, ferromagnetism and ferroelectricity, or ferroelasticity and ferromagnetism.[37] Among these materials, magnetoelectric (ME) materials display a coupling between the magnetic and electric ferroic orders, which is of great interest for both fundamental research and technological applications.[116] Aside from intrinsic magnetoelectric materials such as perovskites containing magnetic atoms, extrinsic composite magnetoelectrics have also been proposed and intensively studied owing to their possible considerable practical importance; in these materials, the ferroic orders are located in different intimately mixed phases. Then, the coupling of the magnetic and electric ferroic orders is mediated by strains and stresses originating from piezoelectricity and magnetostriction.

The manipulation of magnetism by an electric field provides an additional degree of freedom to control the magnetic properties of a material, and vice versa. Experimental and theoretical research on this topic has been intensively performed on different device structures based on inorganic multiferroics.[120-127, 129-131, 133, 136, 189] Concerning organic material-based multiferroics, a nanocomposite consisting of ferromagnetic nanoparticles spread in a ferroelectric polymer matrix was reported in 2011, and the global ME coefficient was extracted from the experimental data.[134] Theoretically designed multiferroic metal-organic frameworks were also reported[190] and were most recently experimentally confirmed[191]. It was also shown that the spin state of some materials could be manipulated by the polarization of organic ferroelectrics.[135] However, a local characterization of magnetoelectricity in organic-based multiferroics was not reported so far. Yet, a local investigation of ME coupling in organic multiferroics is important for a detailed understanding of the ME coupling and for a fine control of multiferroic devices. In addition, organic multiferroics are highly desirable considering the increasing demand of flexible and low cost organic electronic applications.

Several concerns need to be addressed in order to make progress on organic multiferroic materials. First, proper organic materials need to be selected. Among all organic ferroelectric materials to date, poly(vinylidene fluoride-*ran*-trifluoroethylene) (P(VDF-TrFE)) is an excellent candidate to be used as the ferroelectric component in multiferroics, due to its high remnant polarization, short switching time, and low processing temperature (typically 120-140 ℃).[57, 61, 93, 105, 160, 163, 192-194] In contrast, organic magnetic materials are rare and need further development for large scale applications;[195] hence, selecting an inorganic magnetic material is more sensible at the current stage. Second, a proper multiferroic structure needs to be designed, which should be easily fabricated and allow sufficient strain/stress transfer between ferro/piezoelectric and magnetic components, since the ME effect is in most cases generated by electrostriction/magnetostriction coupling.[122, 128, 136] The structure should also be fabricated on a large scale for practical applications. There are currently three common structures used for ME multiferroics: magnetic particles randomly spread in a ferroelectric matrix (Fig. 6.1 (a)), stacked ferroelectric/magnetic layers (Fig. 6.1 (b)), and magnetic materials embedded in a nanostructured ferroelectric matrix (Fig. 6.1 (c)).[122, 132] The first structure might raise problems such as particle aggregation and poor control of particle distribution in the matrix; at any rate, the degree of control over the regularity of the dispersion is poor and not very attractive. The second structure might face the reduction of magnetostriction due to the mechanical clamping of the multilayer on the substrate. Therefore, among these three structures, the last one is most promising for organic multiferroics, potentially avoiding the above mentioned problems. In addition, the last structure could also maximize the contact area between the ferroelectric and the magnetic components, which is favourable for enhanced ME coupling.

Based on this analysis, we selected P(VDF-TrFE) as the ferroelectric component of the multiferroic layers. Then, we designed a structure in which ferromagnetic nickel (Ni) nanocylinders are embedded in a regularly nanostructured P(VDF-TrFE) matrix obtained by nanoimprint lithography (NIL) on centimeter scale

surfaces. Ni was selected as the ferromagnetic component for this first explorative research because it can conveniently be grown in the nanostructured polymer mask by electrodeposition. In addition, Ni has a sufficiently large magnetostrictive coefficient at saturation. The magnetostriction of bulk nickel specimens with randomly oriented grain structure is $\lambda = \Delta L/L = -3.5\ 10^{-5}$. The negative magnetostriction means that the samples contract in the direction of the external field and expand in the transverse direction since the volume of the sample remains nearly constant. Then, we use piezoresponse force microscopy (PFM), a technique widely used to characterize inorganic and organic ferroelectric materials,[58, 196-198] to collect the local ferroelectric hysteresis loops of P(VDF-TrFE) in the multiferroic layer upon application of a magnetic field acting on the Ni nanocylinders. This provides a proof-of-concept experiment of local ME coupling in hybrid regular multiferroics. Moreover, only a few reports discussed the magnetic control of the ferroelectric response of ferroelectric materials in multiferroic materials (intrinsic or extrinsic) and even less in extrinsic multiferroics,[120, 121, 123, 125, 199] which is the main focus in this work, which will demonstrate the possibility to control ferroelectric polarization by a magnetic field.

6.2 Experimental

Multiferroic layer preparation. Fig. 6.1 (d) shows the preparation process of the multiferroic layer. Starting from a Si/SiO_2 substrate, a 100 nm silver (Ag) layer with 5 nm adhesive titanium (Ti) layer was deposited by thermal evaporation, followed by spincoating a *ca.* 75 nm P(VDF-TrFE) layer from a P(VDF-TrFE)/acetylacetone solution (35 g/L, 6500 rpm for 1 min). P(VDF-TrFE) (65 wt% of VDF units and a weight-average molar mass of *ca.* 300 000 g/mol) was provided by Solvay Specialty Polymers. Then, nanoimprint was performed on the P(VDF-TrFE) layer with an Obducat nanoimprinter (at 135 °C, 60 bar, for 10 min) using a Si mold with pillars of 65 nm diameter arranged over a simple square 2D lattice of 190 nm unit cell dimension; the pillar height was 90 nm. After removing the mold, a *ca.*

80 nm thick P(VDF-TrFE) matrix (Fig. 6.2 (a)) with holes of 65 nm diameter fully opened down to the Ag electrode was obtained. Thereafter, Nickel (Ni) nanocylinders of *ca.* 65 nm height were grown using pulsed electrochemical deposition (-1.05 V for 10 ms and -0.7 V for 90 ms) in an electrolyte containing 0.5 M $NiSO_4$ $6H_2O$ and 0.4 M H_3BO_3 at room temperature. The potential was controlled by an Ag/AgCl reference electrode and a platinum (Pt) counter electrode. The packing factor of the Ni nano-arrays is about 9.5 % for the 65 nm diameter sample. Of note, chemical interaction might occur at the interface of P(VDF-TrFE) and Ni during the electrochemical deposition process, but it needs to be confirmed and does not prevent the strain/stress transfer in the multiferroic system. For control experiments, Ni was replaced in the P(VDF-TrFE) matrix by Pt nanocylinders of similar height (C1: P(VDF-TrFE)/Pt control sample). Pt was grown by electrochemical deposition at a constant potential of -0.3 V from a commercially available Pt-DNS electrolyte (METAKEM) at 50 ℃. Two other control samples were also prepared: one consisting of a spincoated *ca.* 80 nm thick P(VDF-TrFE) layer stacked over a continuous 25 nm thick Ni layer which was thermally evaporated on the Ag substrate (C2: bilayered P(VDF-TrFE)/Ni control sample); the other one having a spincoated *ca.* 80 nm thick P(VDF-TrFE) layer on the Ag substrate (C3: P(VDF-TrFE) control sample). These two samples were subsequently annealed at 135 ℃ for 10 min in air on a hot plate.

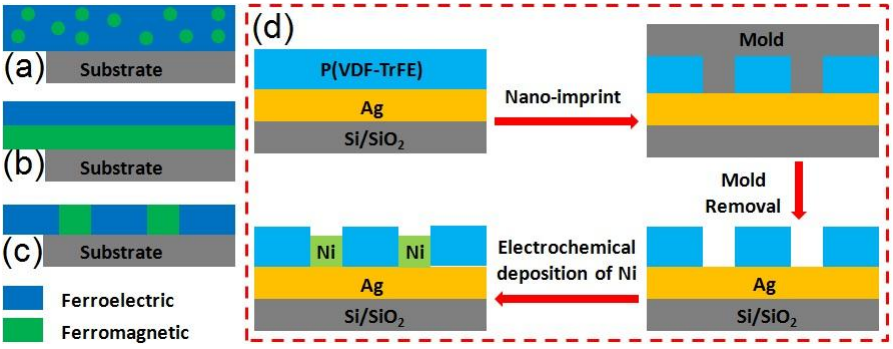

Figure 6.1: Different structures of multiferroic hybrid layer (a-c) and flow chart of the multiferroic layer preparation of this work (d).

Multiferroic layer characterization. The morphology of the sample was checked by atomic force microscopy (AFM) in tapping mode and by scanning electron microscopy (SEM) in imaging mode. The ferroelectric response of P(VDF-TrFE) was checked by PFM in contact mode (under a *ca.* 50 nN contact force). A conductive non-magnetic Pt/Ir coated probe was used (SCM-PIT from Bruker, nominal spring constant 2.8 N/m, nominal tip radius 20 nm). In order to pole the P(VDF-TrFE), a dc voltage was applied to the scanning tip while keeping the bottom electrode (and Ni nanocylinders) grounded. PFM images were then obtained by applying an ac voltage to the bottom electrode (at contact resonance, *ca.* 220 kHz) while keeping the scanning tip grounded. In the case of PFM spectroscopy mode under an applied magnetic field, a non-magnetic tip holder was used and working frequencies of 15 kHz or 300 kHz were selected, both far away from the contact resonance (*ca.* 220 kHz). When working at 15 kHz, all PFM spectroscopy curves were obtained by ramping the tip bias from 10 V to -10 V, then back to 10 V (15 V for the bilayered P(VDF-TrFE)/Ni control sample); the ramping direction was reversed when working at 300 kHz. Prior to attempting to switch the polarization of P(VDF-TrFE) by varying the magnetic field on the nanopatterned P(VDF-TrFE)/Ni sample, PFM hysteresis loops were taken at 0 and 5000 Oe magnetic field (working at 300 kHz and ramping the tip bias from -10 V to 10 V, then back to -10 V) in order to check the location of the switching voltage. The magnetic field in the vertical direction was generated by a home-made magnet equipped with a cooling system, which was adapted into the PFM equipment below the sample. In the case of applying magnetic fields of both polarities, a non-cooled magnet was used, because it allowed an easier switching of the current and magnetic field direction; in this case, the temperature increased moderately upon the application of the magnetic field. The magnetic hysteresis of Ni in the multiferroic layer was measured by an alternating gradient field magnetometer (AGFM).

6.3 Results and Discussion

6.3.1 Morphology and dimensional characterization

Fig. 6.2 (a) shows the AFM topography of the P(VDF-TrFE) template after nanoimprinting; the depth of the holes is *ca.* 80 nm (Fig. 6.2 (c)). The topography of the final multiferroic layer is shown in Fig. 6.2 (b) and the height difference between the top of the P(VDF-TrFE) matrix and the top of the Ni nanocylinders is *ca.* 15 nm (Fig. 6.2 (d)). Therefore, the height of the Ni nanocylinders is *ca.* 65 nm (80 nm - 15 nm). Fig. 6.2 (e-g) shows SEM images of the P(VDF-TrFE) template (e) and of the P(VDF-TrFE)/Ni multiferroic layer (f-g). It is obvious that Ni grew properly in the holes of the P(VDF-TrFE) template. In addition, Fig. 6.2 (f) also proves that nanoimprint lithography can produce regular nanopatterns on a large scale.

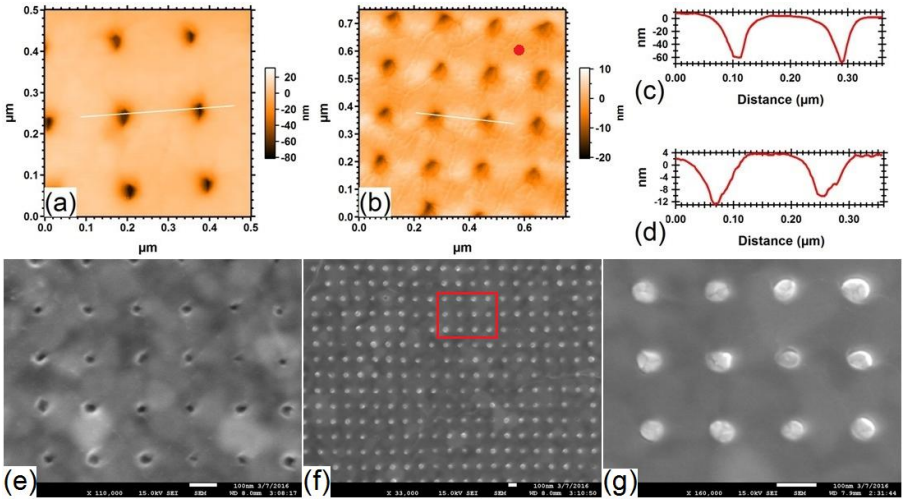

Figure 6.2: Morphology and height characterization of the multiferroic layer. (a) AFM topography image of the nanoimprinted P(VDF-TrFE) template. (b) AFM topography image of the multiferroic layer after Ni deposition in the P(VDF-TrFE) template. The red dot is the position where the PFM tip was placed to measure the ferroelectric hysteresis loop of P(VDF-TrFE). Panels (c) and (d) are height profiles corresponding to the lines in panels (a) and (b). Panels (e-g) are SEM images of (e) the P(VDF-TrFE) template and (f-g) the P(VDF-TrFE)/Ni multiferroic layer. (g) is the enlarged image of the red-boxed area in (f). The scale bar in panels (e-g) is 100 nm.

6.3.2 Ferroelectric/magnetic characterization of P(VDF-TrFE)/Ni in the multiferroic layer

Fig. 6.3 (a) shows a vertical PFM amplitude image of P(VDF-TrFE) in the multiferroic layer where two small regions (boxed in red) were previously poled by applying 12.5 V or -12.5 V on the scanning tip while keeping the sample bottom electrode grounded. Both poled regions show a strong contrast compared to the unpoled region, indicating that P(VDF-TrFE) can be poled by the application of a sufficiently strong electrical field. However, it is worth noting here that the roughness of the multiferroic layer, combined with its ferroelectric/conducting nature, results in values of PFM amplitude considerably deviating from ideality.

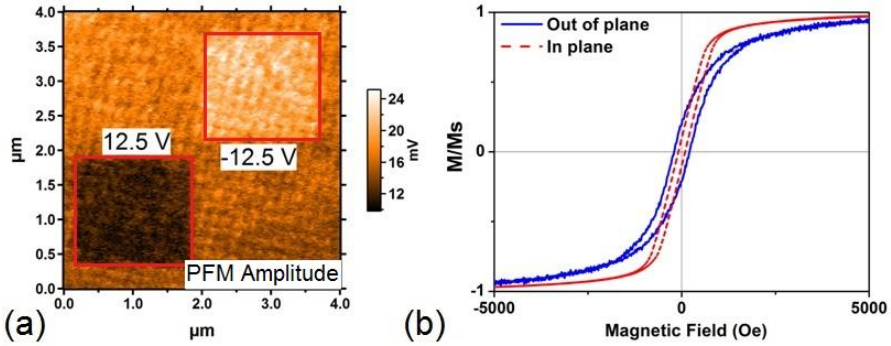

Figure 6.3: (a) PFM amplitude image of P(VDF-TrFE) in the multiferroic layer. Two small regions (1.5 μm x 1.5 μm, boxed in red) were previously-poled by applying dc voltages of 12.5 V and -12.5 V before taking the PFM image. (b) Magnetic hysteresis loops of Ni in the multiferroic layer measured by an AGFM at room temperature in the out-of-plane and in-plane directions.

Fig. 6.3 (b) shows macroscopic magnetic hysteresis loops of Ni in both out-of-plane and in-plane directions, confirming the ferromagnetic character of the Ni nanocylinders. There exists a considerable difference between the two loops, meaning that the Ni nanocylinders grown in the multiferroic layer are magnetically anisotropic with the in-plane direction being the easy axis. The

magnetization configuration of such low aspect ratio cylindrical Ni particles with diameter of 65 nm in the remanent state forms a closed vortex structure within the nanopillar.[200] The vortex structure consists of circumferential magnetization in the plane of the cylinder with an out-of-plane component near the central position.

6.3.3 Ferroelectric characterization of P(VDF-TrFE) in the multiferroic layer under application of a magnetic field

The PFM amplitude and phase signals were first checked on the P(VDF-TrFE) control sample (C3) with and without the application of a magnetic field in order to verify the lack of interaction between the PFM build-in electronics and the magnetic field. As shown in Fig. 6.10 of the supporting information, the PFM signals remain unchanged upon the application of the magnetic field, proving the absence of spurious coupling of the magnetic field with the PFM setup. Then, the ferroelectric response of P(VDF-TrFE) in the multiferroic layer under the application of a vertical magnetic field was checked by PFM at a position equivalent to the one marked by the red dot in Fig. 6.2 (b).

Vertical PFM phase hysteresis loops (obtained at both 15 kHz and 300 kHz) at two different magnetic fields are presented in Fig. 6.4 (a,b), clearly showing that the width of the hysteresis decreases with increasing magnetic field. We note that the centers of the hysteresis loops are shifted compared to the ideal situation, most probably due to the relatively large amplitude of the ac voltage (2-2.5 V) and/or the existence of other electrostatic couplings in the PFM equipment.[197, 201] Nevertheless, this shift does not change the qualitative evolution of the hysteresis nor influence the analysis of the width of the hysteresis loops. In addition, the hysteresis loops are reversed depending on whether they are measured above or below the resonance frequency, as expected (Fig. 6.4 a and b); furthermore, their width depends on the frequency of the measurement, as is also the case for a pure P(VDF-TrFE) layer (Fig. A2.5 of Appendix A2).

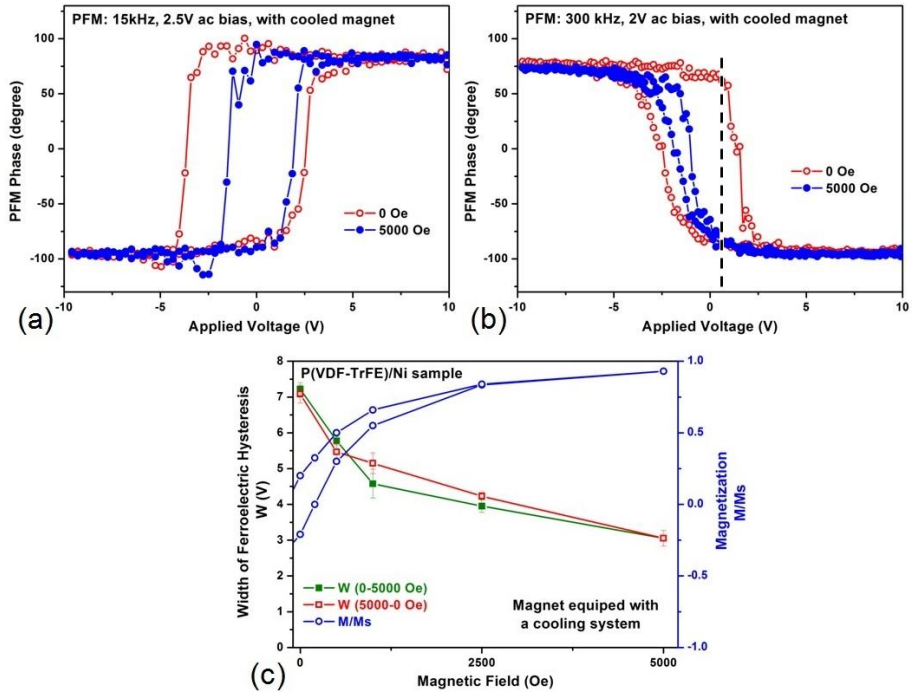

Figure 6.4: PFM characterization of P(VDF-TrFE) in the multiferroic layer under external out-of-plane magnetic fields. (a) and (b) PFM phase hysteresis loops of P(VDF-TrFE) obtained at 15 kHz and 300 kHz under two different magnetic fields. (c) Width of the ferroelectric hysteresis loop versus applied magnetic field (15 kHz PFM working frequency). The magnetic hysteresis loop of Ni (extracted from Fig. 6.3 (b)) is also shown here as a reference. The vertical dashed line in panel (b) indicates the approximate value of the voltage used for switching experiments by the magnetic field (see below).

The width of the hysteresis loop is displayed versus the applied positive magnetic field in Fig. 6.4 (c), which also presents the magnetic hysteresis of Ni as a comparative reference. We found that the width decreases significantly with increasing magnetic field in both polarities of positive and negative magnetic fields; the experiment was repeated at several other positions and provided identical behavior. A second, independently-prepared sample was also checked and exhibited the same behaviour. Hysteresis loops obtained

at more magnetic field values, and the width of the loops versus the complete (positive and negative) range of applied magnetic field, are shown in Fig. 6.9 of the supporting information; in this case, a non-cooled magnet was used for the switching of the magnetic field direction, resulting in a more noisy curve due to the variations of temperature. In addition, a sample prepared with a 2.5 times larger supracrystalline unit cell and a smaller Ni volume fraction (7% packing factor) exhibited a weaker effect, indicating the importance of dimensional parameters (Fig. 6.13 in the supporting information).

The same experiment was also performed on several control samples. In the P(VDF-TrFE)/Pt control sample (C1, shown in the inset of Fig. 6.5 (a)), ferromagnetic Ni was replaced by non-magnetic Pt. As shown in Fig. 6.5 (a), the width of the ferroelectric hysteresis, measured with the non-cooled magnet, decreases slightly with increasing magnetic field, most probably due to the temperature variation induced by the magnet. However, this slight decrease is negligible compared to the one of the P(VDF-TrFE)/Ni sample, suggesting that the significant change of ferroelectric response shown in Fig. 6.4 upon application of the magnetic field is indeed due to the ferromagnetic nature of Ni, and most probably results from its magnetostriction.

To further support the role of magnetostriction in the magnetic field dependence of ferroelectric loops, another control sample consisting of a continuous Ni layer and overcast P(VDF-TrFE) layer (C2, shown in the inset of Fig. 6.5 (c,d)) was tested by PFM under an applied magnetic field. In this case, the dimensional change of the Ni layer is prevented or at least strongly reduced due to its clamping to the substrate, and no or negligible strain should thus be transferred to the P(VDF-TrFE) layer. This is supported by previous observations made on inorganic muliferroics, in which it was theoretically predicted and experimentally confirmed that nanostructured multiferroics have larger ME coupling effect compared to stacked continuous layers.[122, 123] Therefore, the ferroelectric response under different magnetic fields should be unchanged, which is precisely

observed in Fig. 6.5 (c,d). The slight effect detected in Fig. 6.5 (c) is again most probably due to temperature variations associated to the heating of the magnet, as it is known that the coercive field of P(VDF-TrFE) decreases with temperature.[202] When eliminating the temperature variation by using a cooled magnet, as shown in Fig. 6.5 (d), the hysteresis width keeps unchanged for all applied magnetic fields, confirming that the slight change of width when using a non-cooled magnet is indeed due to temperature variations. In addition, the width variation is also smaller for the same magnetic field when using the cooled magnet compared to the non-cooled magnet, which is also most probably due to the better controlled temperature. The width of hysteresis loops obtained with the last control sample (C3, continuous P(VDF-TrFE) layer on Ag substrate, shown in the inset of Fig. 6.5 (b)) is also the same for different magnetic fields, as shown in Fig. 6.5 (b).

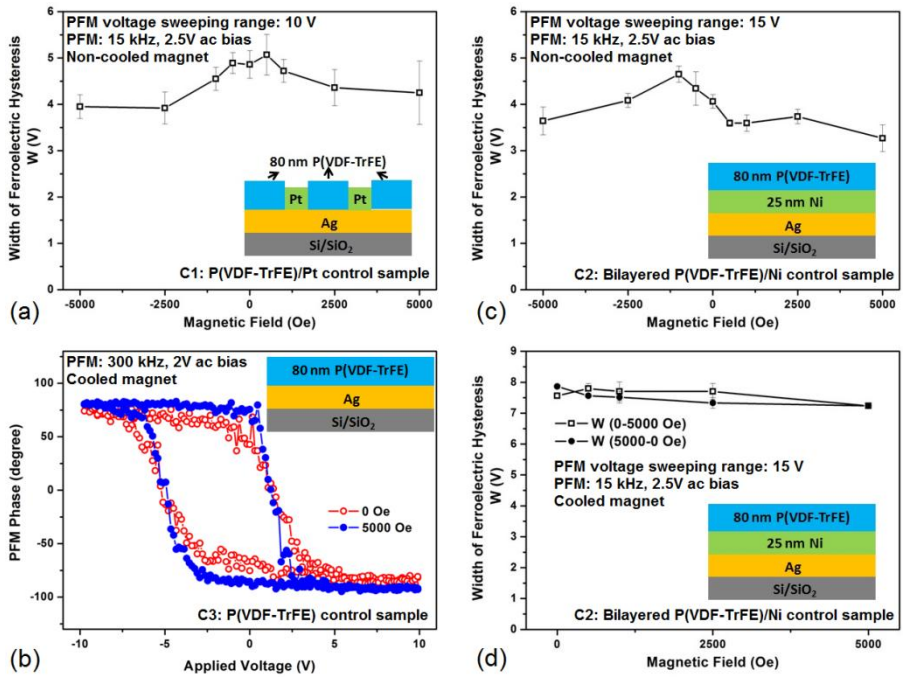

Figure 6.5: Width of the ferroelectric hysteresis versus applied magnetic field, or hysteresis loops at different magnetic fields, for (a) a P(VDF-TrFE)/Pt control sample, (b) a continuous P(VDF-TrFE) control sample, and (c) (d) a bilayered P(VDF-TrFE)/Ni control sample.

A potential issue of our local measurements is that the distribution of electric field lines in the metallic/insulating hybrid layer might unduly increase the PFM sensitivity to specific features of the layer. That this is not so is shown in Fig. 6.6, where the field existing in the sample below the PFM tip is displayed, based on finite element modeling (COMSOL) : the electric field concentrates below the PFM tip, not close to the Ni nanocylinders, except when the PFM tip is strongly off-centered compared to the unit cell. This indicates that PFM feels the response in a small volume of the polymer just below the tip, away from the Ni edges, indicating that the influence of the magnetic material propagates over distances as large as 100 nm.

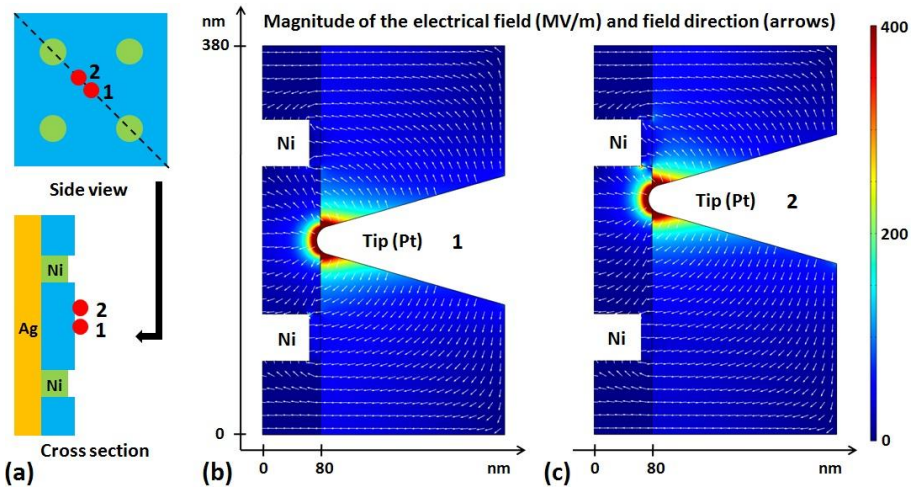

Figure 6.6: COMSOL simulation of the electric field distribution through the P(VDF-TrFE) layer. (a) Schematic view of the sample which is taken into account in the simulation. The cross section is taken along the dashed line. Panels (b-c) show the magnitude of the electrical field (color code) and its direction (white arrows) in the plane shown by the dashed line in (a) at position 1 (b, tip in center of unit cell) and 2 (c, tip off center). The simulation was done by keeping Ag and Ni grounded and applying 10 V on the tip.

The previous observations thus confirm that hybrid organic multiferroics can exhibit a very strong ME effect, presumably due to

magnetostrictive/piezoelectric coupling. This change of ferroelectric response should thus be directly linked to the magnetostriction of Ni.[203,81] The Ni nanocylinders contract in length in the presence of a magnetic field of either polarity, and swell slightly in diameter, resulting in a strain being transferred to the softer ferroelectric P(VDF-TrFE). Stronger effects are expected in the range where the magnetization of Ni varies strongly with the magnetic field, which is indeed the case (Fig. 6.4 (c)). Because magnetostriction is an even function of the magnetic field, positive and negative polarities of the magnetic field should lead to the same effect on the ferroelectric hysteresis loop, as indeed observed (Fig. 6.9 of the supporting information). It should be stressed that the magnitude of the magnetostriction coefficients in ferromagnetic nanoparticules can be quite different from those of bulk materials.[204, 205] In our case, application of the external magnetic field in the out-of-plane direction may produce quite large magnetostriction because of the in-plane vortex structure.

The strain is applied to a complex semicrystalline microstructure, consisting of crystalline lamellae separated by amorphous interlamellar regions made of chain folds, loose loops, dangling chain ends, and tie segments. Because the glass transition temperature of amorphous P(VDF-TrFE) is below room temperature,[206] strains will dominantly affect the softer amorphous interlamellar regions, resulting in a significant storage of mechanical energy in these regions. Relaxation of this energy can occur through localized segmental motion in the amorphous regions. Ferroelectric switching actually involves a combination of rapid flow motion of domain walls in crystals, and slower creeping in the intervening amorphous regions, as was recently demonstrated.[62] The mechanical energy stored in the amorphous regions might thus contribute to ease segmental relaxation and therefore creeping of domain walls through the amorphous regions, resulting in an easier polarization switching and therefore a lower coercive field.

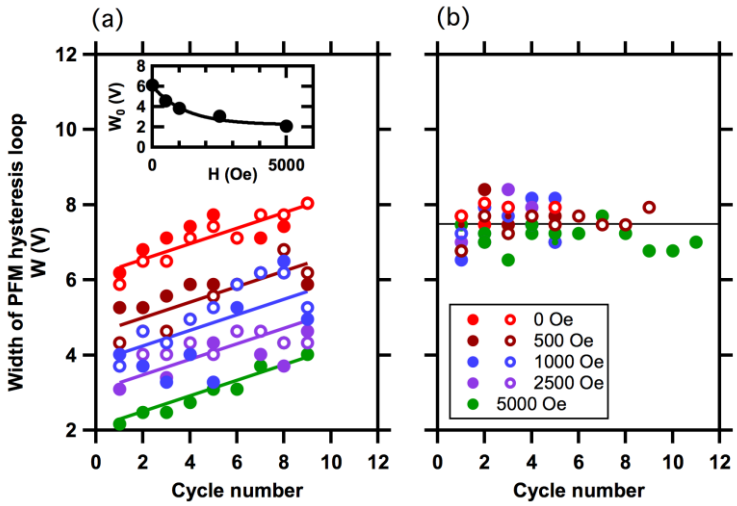

Figure 6.7: Variation of the width of ferroelectric hysteresis loops upon repeated probing at a given value of applied magnetic field. All data were acquired at the very same position and 15 kHz PFM working frequency. Closed symbols refer to experiments in which the magnetic field was ramped up, starting from 0 Oe; open symbols to experiments in which the field was ramped down from 5000 Oe; the color code for the magnetic field is given in the legend of panel (b). Panel (a) is for the patterned sample; the inset shows the variation of the width of the hysteresis loops extrapolated to zero probing cycle, versus applied magnetic field. Panel (b) is for the reference bilayer sample.

If this mechanism is true, repeated switching should progressively relax the strain in the amorphous region, with as a result a decreased effect of the magnetic field on the ferroelectric hysteresis. Experiments were thus performed, during which the ferroelectric hysteresis was repeatedly probed for a given magnetic field; the field was then increased or decreased, and the measurements performed again. A limited set of hysteresis loops is presented in Fig. 6.11 of the supporting information, from which the width of the loops was obtained. Fig. 6.7 (a) shows that the width of the ferroelectric hysteresis loop increases upon repeated probing at a given value of magnetic field, for the patterned sample. In contrast, the width of the

hysteresis loop is independent of cycle number and magnetic field for the bilayered reference sample (Fig. 6.7 (b)). This confirms that, for the patterned sample, the strain in the ferroelectric polymer is progressively relaxed by the segmental motions resulting from the ferroelectric switching; as a result, the switching becomes more difficult and the coercive electric field increases.

Experiments performed at the same location, upon ramping the magnetic field up or down, led to identical results (closed and open symbols in Fig. 6.7 (a)), indicating that each new application of the magnetic field resets the strain in the system. The complete set of relaxation data could be fit by lines of common slope (0.21 V/cycle) and varying ordinates at the origin, W_0. The inset of Fig. 6.7 (a) shows the variation of W_0 with the magnetic field: again, this variation parallels fairly well the variation of the magnetization of Ni with magnetic field, as shown in Figs 6.3 (b) and 6.4 (c).

The dependence of the width of the hysteresis loops on magnetic field is very strong in our patterned samples. Therefore, we attempted to reverse the polarization of the ferroelectric material by varying the magnetic field (using the cooled magnet), at a constant value of electric field defined by *ca.* 0.5 V set on the PFM tip, as indicated by the dashed line in Fig. 6.4 (b). With 5000 Oe of applied magnetic field, this electric field is higher than the coercive field; in the absence of applied magnetic field, this electric field is lower than the coercive field. This experiment was done with the PFM ac bias frequency set to 300 kHz,since this high frequency provides more stable PFM signals (Fig. 6.10 of the supporting information).

When the magnetic field was switched repeatedly between 0 and 5000 Oe, as shown in Fig. 6.8 (left), the PFM phase was found to change between two values of *ca.* -90 ° and *ca.* 50 °, corresponding to a whooping 140 ° phase change, close to a full reversal of the electric dipole moment direction (180 ° phase change, in theory). This indicates that the electric dipole moment is reoriented by the magnetic field. In addition, the phase difference was found to slightly decrease upon repeated application of the magnetic field, confirming that a

relaxation of the stored mechanical energy generated by the magnetostrictive/piezoelectric coupling happens. When the same reversal test was performed on the bilayered P(VDF-TrFE)/Ni control sample (Fig. 6.8, right), the PFM phase was found to be insensitive to the magnetic field. However, it is worth noting that the selection of the value of the static voltage used for the polarization reversal by the magnetic field is very critical, due to the narrow operation window shown in Fig. 6.4 (b) and/or the possible unstable PFM phase signal during the experiment. Fig. 6.12 of the supporting information shows the PFM phase for a static voltage of *ca.* 1 V, in which case, the phase change introduced by the magnetic field is less than 50 °.

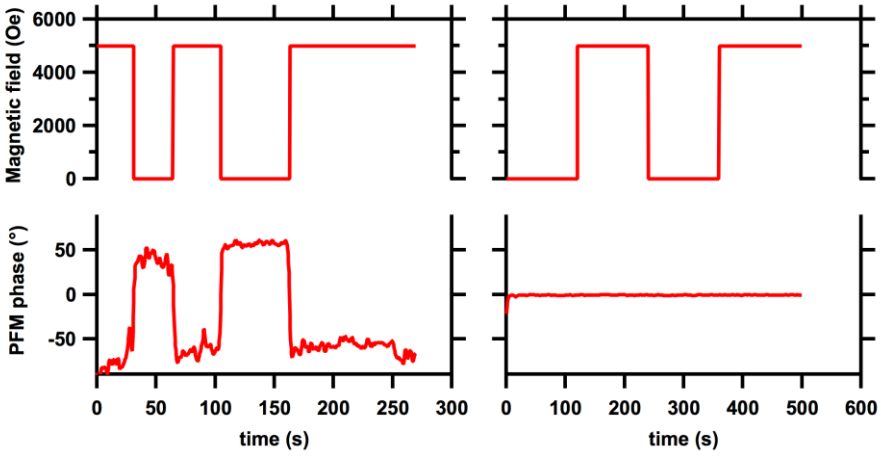

Figure 6.8: Ferroelectric polarization reversal by the application of a magnetic field. The dashed line in Fig. 6.4 (b) shows the value of applied voltage at which polarization reversal upon application of a magnetic field was performed. The graph shows the PFM phase (modulo 180 °) of the ferroelectric polymer measured by PFM upon on/off switching of the magnetic field for (left) the P(VDF-TrFE)/Ni patterned multiferroic sample and (right) the bilayered P(VDF-TrFE)/Ni control sample. The PFM phase was binomially-averaged with 20 passes.

These experiments fully confirm the possibility to act magnetically upon the electric dipole moment of the patterned

ferroelectric material, and to almost fully reverse its orientation. However, the magnetic switching of the electric dipole moment does not exhibit hysteresis, indicating that the magnetic field does not switch permanently the electric dipole moment in our sample. This might be due to the fact that the magnetic field acts reversibly on the electric dipole moment because of the reversibility of the magnetically-induced mechanical deformation; or the reversibility might arise from the incomplete reversal of the electrical polarization, due to the narrowness of the window for magnetic actuation (Fig. 6.4 (b)). Complementary experiments on samples of different pattern geometry are required to progress further in this issue.

6.4 Conclusion

Summing up, we have set up a methodology to fabricate regular nanopatterns of a magnetic material within a soft ferroelectric polymer. Experiments performed on these and control systems indicate a strong effect of the magnetic field on the ferroelectric hysteresis loop of the polymer, most probably provided by the coupling of the magnetostriction of Ni and the ferroelectricity of P(VDF-TrFE). Due to this effect, it becomes possible to almost reverse the polarization of the ferroelectric material by applying a magnetic field, while simultaneously applying an appropriate voltage on the sample. Experiments indicate the importance of relaxation in these complex materials, most probably due to segmental motion in the amorphous regions of the ferroelectric polymer. Our organic-based multiferroic material displays an unprecedented high sensitivity of the electric polarization on magnetic field, and offers a new direction for future possible applications in organic electronics (*e.g.*, organic memory devices). Future work should aim at amplifying the effect further, in order to reach complete electrical polarization switching by a magnetic field; this might possibly be attained by increasing the strain in the ferroelectric material, *e.g.*, by using a magnetic material with larger magnetostriction, or by decreasing further the size of the

ferroelectric material while increasing the one of the ferromagnetic regions.

6.5 Supporting Information

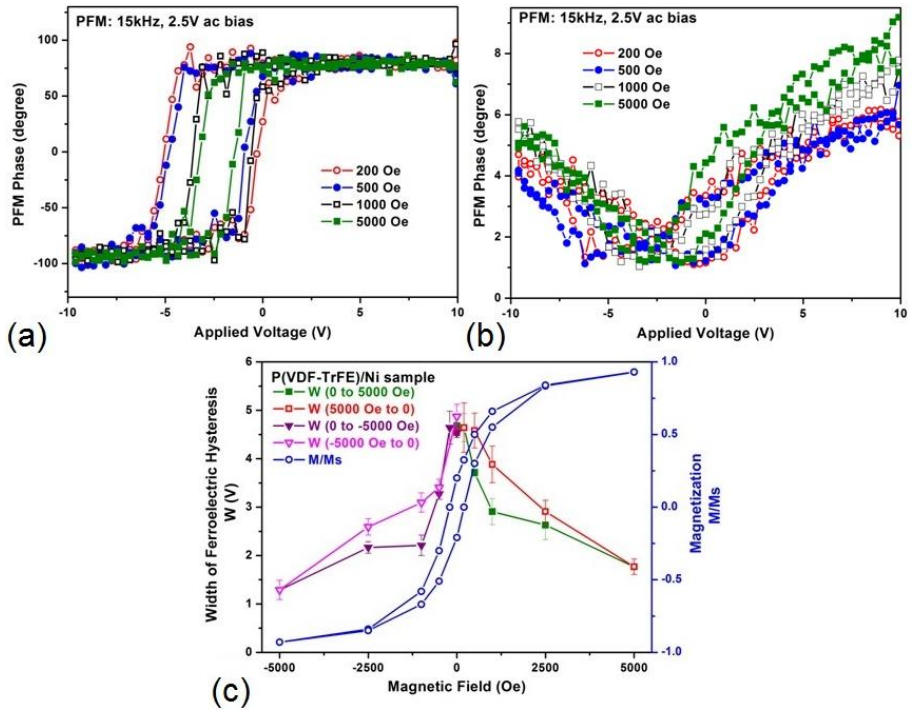

Figure 6.9: PFM characterization of P(VDF-TrFE) in the multiferroic layer under application of an external out-of-plane magnetic field of both polarities, using a non-cooled magnet. (a) PFM phase and (b) amplitude hysteresis loops of P(VDF-TrFE) under four different values of magnetic field. (c) Width of the ferroelectric hysteresis loop versus applied magnetic field. The magnetic hysteresis loop of Ni (extracted from Fig. 6.3 (b)) is also shown here as a reference.

The vertical PFM phase and amplitude hysteresis loops obtained at four different magnetic fields (non-cooled magnet) are presented in Fig. 6.9 (a,b), clearly showing that the width of the hysteresis decreases with increasing magnetic field. This width is displayed

versus the applied magnetic field in Fig. 6.9 (c), which also presents the magnetic hysteresis of Ni as reference. The width decreases significantly with increasing magnetic fields in both polarities of positive and negative magnetic fields (*ca.* 3 V at 5000 Oe).

It is worth noting that the width of ferroelectric hysteresis is in general smaller than that in the case of using a cooled magnet whose temperature was kept constant during the application of the magnetic field (*e.g.*, 7 V versus 5V at 0 Oe at 15 kHz PFM working frequency). This results most probably from the coercive field of P(VDF-TrFE) decreasing with increasing temperature.[202] In addition, the width variation is also larger, which is also most probably due to temperature effects.

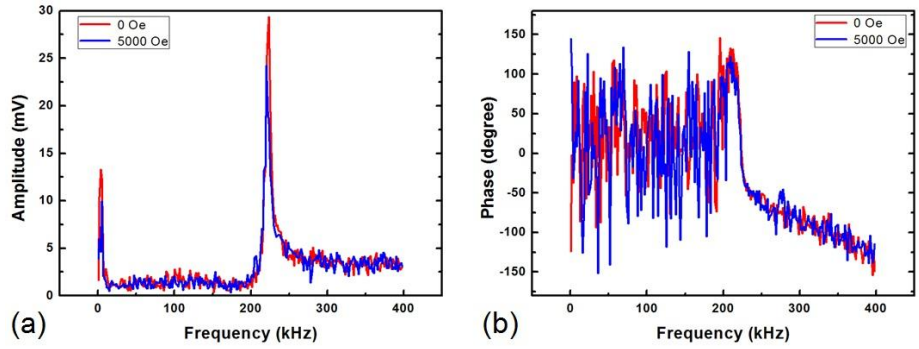

Figure 6.10: PFM (a) amplitude and (b) phase versus the frequency of the applied ac bias (2 V amplitude) obtained with the P(VDF-TrFE) control sample (C3, 80 nm thick P(VDF-TrFE) layer on Ag substrate) at different magnetic fields. Below the contact resonance frequency (*ca.* 220 kHz), the PFM phase signal was rather noisy; in contrast, the PFM signal was more stable above the contact resonance frequency. These results are consistent with the previous observations.[158]

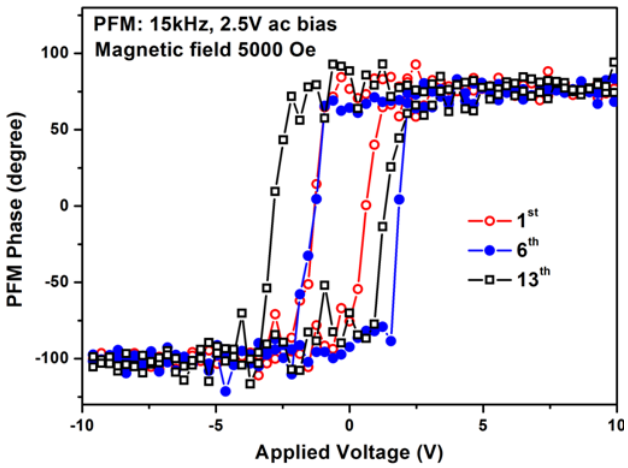

Figure 6.11: Evolution of ferroelectric hysteresis loops of the nanopatterned P(VDF-TrFE)/Ni sample upon repeated measurements (the index of the measurement is shown in the legend).

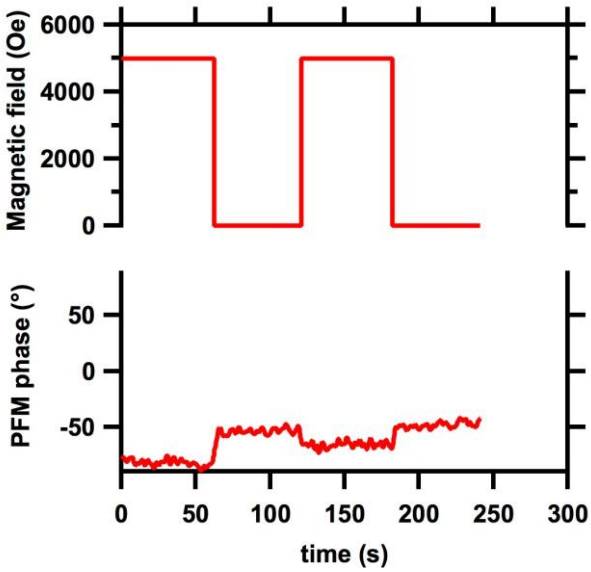

Figure 6.12: Ferroelectric polarization tuning by the application of a magnetic field at a static voltage of *ca.* 1 V performed on the nanopatterned multiferroic P(VDF-TrFE)/Ni sample. These conditions do not lead to the optimal coupling between polarization and magnetic field, in contrast with Fig. 6.8.

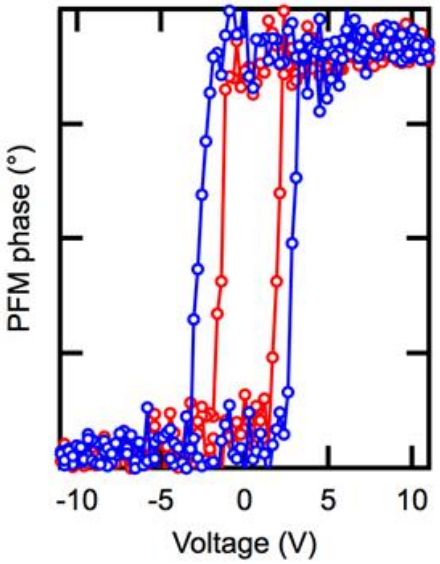

Figure 6.13: PFM hysteresis loops of a patterned sample of 500 nm unit cell size, 150 nm Ni diameter, 70 nm Ni height, and 90 nm PVDF-TrFE thickness (15 kHz PFM acquisition frequency), in the absence (blue) and in the presence (red) of a magnetic field (5000 Oe).

Chapter 7

Summary and Perspectives

The last decade has witnessed the increasing interest and demand for fundamental research and practical applications of organic electronics, including organic memory devices based on ferroelectric polymers. In addition, the fast development of nanotechnological tools and techniques such as nanoimprint lithography (NIL) and scanning probe microscopy (SPM, including piezoresponse force microscopy, PFM) has brought research and applications to a new level. Now it becomes possible and reliable at the nanometer scale to manipulate and characterize organic materials and functional devices, to improve material properties and device performance through the fine control of the material nano- or micro-structure, and to design new functional layers and device structures. In this context, this thesis contributes directly to all these aspects and provides information to promote organic ferroelectric memories and multiferroic materials a step further. The main achievements of this thesis and some perspectives are summarized here:

In Chapter 3, we have systematically studied by PFM the local ferroelectric polarization and/or depolarization of P(VDF-TrFE) in FeFET devices using p-type PTAA as organic semiconductor. PFM results show that a stable polarization state can be obtained irrespective of the location of P(VDF-TrFE) in FeFETs, in which the semiconducting layer is in the accumulation state and provides compensating charges at the PTAA/P(VDF-TrFE) interface after removal of the poling voltage. Surprisingly, another stable state of opposite direction is also achievable when the depleted PTAA layer is thin enough and/or the poling voltages are sufficiently large. In this state, the ferroelectric is depolarized over the main part of the channel regions, whereas it is polarized over the electrodes and neighboring channel regions. The size of the polarized regions depends on the thickness of the semiconducting layer, because PTAA acts as an

insulator dividing the applied voltage during poling; in addition, the degree of polarization after removal of the poling voltage also depends on the thickness of the PTAA layer, which screens the polarization-compensating charges accumulated in the source and drain electrodes. These polarized regions in the second stable state make the PTAA more depleted and modify the charge injection barrier between the electrodes and the PTAA layer. As a result, FeFET devices of thinner PTAA layer have less positive (and even negative) threshold voltages, leading to an increase of the on/off current ratio at zero gate bias and therefore to an improvement of the memory device performance. These unexpected results provide new clues for device design and performance optimization of memory FeFETs. Moreover, our results give a complete spatial view of ferroelectric polarization and depolarization in these complex devices, and on the working mechanism of memory FeFETs.

In Chapter 4, we have integrated NIL in the fabrication process of a top-gate bottom-contact organic FeFET. P(VDF-TrFE) imprinted in complete confinement on top of PTAA shows a decreased switching field compared to a continuous reference, and thereby, the electric field needed to maximize the remnant polarization is significantly decreased by a factor of *ca.* 1.5 compared to a continuous film. Current characterizations on FeFETs show that the nanoimprinted one needs a smaller poling voltage to reach the maximum polarization-induced current, compared to the continuous reference. This leads to a decreased operating voltage for the memory application. In addition, since our fabricated transistor consists of a large number of nanowire-gated transistors placed in parallel, it also offers potential possibilities for a strong size reduction of organic FeFETs.

In Chapter 5, we have designed a novel organic hybrid layer consisting of alternating ferroelectric/semiconducting polymer nanowires, fabricated by shaping P(VDF-TrFE) into nanowires by NIL, followed by filling the separating spaces by semiconducting PTAA polymer. This methodology leads to the easy creation of

well-controlled hybrid nanostructures over intergiditated electrodes. In this hybrid layer, when the ferroelectric nanowires are poled with the proper polarity, the ferroelectric dipole moment can be stabilized by charges accumulating laterally in the semiconducting channels, thereby preventing depolarization even though the ferroelectric material rests over an insulating substrate. This lateral electrostatic coupling between the ferroelectric and the semiconducting material is made possible by the reduction in size of the ferroelectric material. The charge accumulation only occurs for one direction of polarization, due to the p-type nature of the semiconductor, and creates a channel for conduction from source to drain due to this new charge compensation mechanism, which can be directly used for memory applications. The characterization of the source-drain current versus the previously-applied poling voltage shows clearly a current hysteresis as typically observed in traditional FeFET memory devices. In addition, the on/off current ratio scales with the size of the poled region, thereby providing access to a memory containing more than two stored states and possibility to scale down the memory size possibly to one single ferroelectric/semiconducting nanowire.

For the nanoimprinted memory devices presented in Chapters 4 and 5, the conductive PFM tip is used as the mobile top gate. A remaining technological problem for integrated memory circuits is addressing real electrodes on the nanoimprinted P(VDF-TrFE) nanowires. Therefore, properly filling the openings between P(VDF-TrFE) nanowires for insulation, before depositing the electrode, would be a must. To do so, we have developed a methodology to put the insulating polymer polycaprolactone into the trenches to form a hybrid layer consisting of alternating P(VDF-TrFE)/polycaprolactone nanowires. Then the local ferroelectric properties of P(VDF-TrFE) in this hybrid layer were characterized by PFM. These results are presented in Appendix A3. Although a hybrid layer consisting of P(VDF-TrFE) nanowires with proper filling of polycaprolactone is obtained, further work is still needed to optimize the filling conditions and to characterize the macroscopic ferroelectric properties of P(VDF-TrFE) nanowires in the

hybrid layer, as well as the performance of memory devices employing this hybrid layer.

In Chapter 6, we have developed a methodology to fabricate regular nanopatterns of a magnetic material within a soft ferroelectric polymer. Experimental results indicate a strong effect of the magnetic field on the ferroelectric hysteresis loop of the polymer, most probably due to the coupling of the magnetostriction of Ni and the ferroelectricity of P(VDF-TrFE). Due to this effect, it becomes possible to almost reverse the polarization of the ferroelectric material by applying a magnetic field with proper conditions Experiments also show the importance of relaxation in these complex materials, most probably due to segmental motion in the amorphous regions of the ferroelectric polymer. Our organic-based multiferroic layer offers a new direction for future possible applications in organic electronics (*e.g.*, organic memory devices). Future work should aim at amplifying the effect further, in order to reach complete electrical polarization switching by a magnetic field; this might possibly be attained by increasing the strain in the ferroelectric material, *e.g.*, by using a magnetic material with larger magnetostriction, and/or by decreasing further the size of the ferroelectric material while increasing the one of the ferromagnetic regions, and/or by designing new layer configurations (*e.g.* with alternating ferroelectric/ferromagnetic nanowires) having possibly optimized magnetostrictive/piezoelectric coupling. Our results also suggest that the pressure has significant influence on ferroelectric properties of P(VDF-TrFE); therefore, a detailed study of the effect of pressure on the ferroelectric properties of P(VDF-TrFE) should be done in the future. In addition, this chapter only focuses on the magnetic control of the electric response in the multiferroic layer; the reversed effect, i.e., the electric control of the magnetic response, should be future investigated. Moreover, for future macroscopic applications, it is also required to insolate the bottom and top electrodes by putting another insulating polymer on top of the ferromagnetic metal or by using non-conductive/insulating ferromagnetic materials instead of ferromagnetic metals.

In summary, nanoimprinted ferroelectric P(VDF-TrFE) with well controlled nanopatterns is of great interest for practical applications of organic electronics, *e.g.*, organic memories. As demonstrated in this thesis, the operating voltage of the nanoimprinted memory devices is significantly reduced; the well-controlled nanostructures allow us to control precisely the material properties and their couplings, and to design new memory device configurations in combination with other functional materials, *e.g.*, semiconducting polymers and ferromagnetic materials; in addition, nanoimprinted P(VDF-TrFE) nanostructures offer great potential to reduce the size of organic memory devices, possibly down to the tens of nanometers scale.

Going beyond this thesis, other functional materials could be conbined with nanoimprinted ferroelectric P(VDF-TrFE) to form new functional layers and devices. For example, light sensitive materials could be used to fabricate nanoimprinted solar photovoltaics with the possibility to have enhanced efficiency controlled by the ferroelectric polarization, light emitting materials could be combined to fabricate nanoimprinted light emitting devices with coexistent memory functionality, and the polarization of the light might be controlled in devices employing magnetic materials with nanoimprinted P(VDF-TrFE). In addition, bio-materials and bio-objects like bacteria could be grown in the openings or on the top of the nanoimprinted P(VDF-TrFE) and their properties and activities might be controlled by the polarization charges of the ferroelectric P(VDF-TrFE).

More broadly, NIL provides capabilities to shape any soft amorphous or (semi)crystalline material, to control the crystalline orientation and improve the functional properties of functional materials, and to produce well ordered nanostructures for patterning and designing new device configurations; it is thus expected to find more advanced applications in the future.

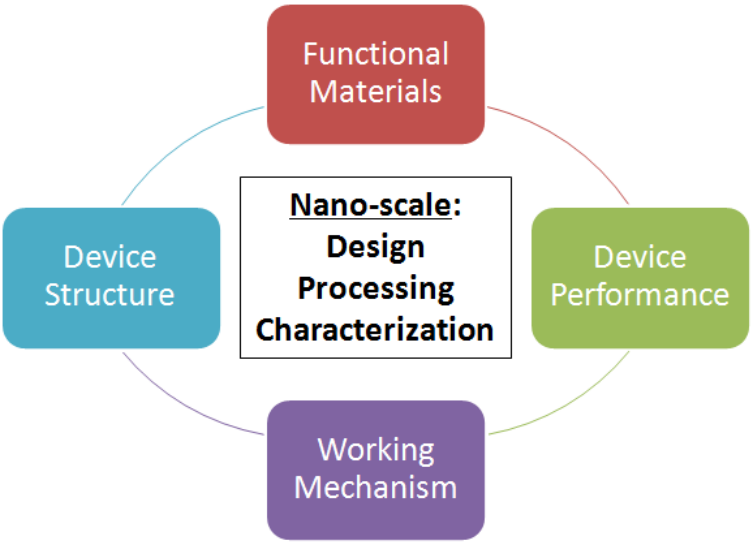

Figure 7.1: General scheme and strategy to fabricate and characterize a functional device.

As has been proven by the realization of the objectives of this thesis, nanoscale tools and equipments, like NIL and AFM-based techniques, allow us to obtain new advanced memory devices by incorporating proper functional materials and conceiving new device structures; it also provides a new view of these devices through a very local characterization of the working mechanism and device performance. It is expected that this strategy could be extended to fabricate and characterize any new functional devices in the future, as shown in Fig. 7.1.

References

1. Gelinck, G. H. *et al.* Flexible active-matrix displays and shift registers based on solution-processed organic transistors. *Nat. Mater.* **3,** 106-110 (2004).

2. Huitema, H. E. A. *et al.* Plastic transistors in active-matrix displays. *Nature* **414,** 599-599 (2001).

3. Chen, Y. *et al.* Electronic paper: Flexible active-matrix electronic ink display. *Nature* **423,** 136-136 (2003).

4. Myny, K. *et al.* Organic RFID transponder chip with data rate compatible with electronic product coding. *Org. Electron.* **11,** 1176-1179 (2010).

5. Forrest, S. R. The path to ubiquitous and low-cost organic electronic appliances on plastic. *Nature* **428,** 911-918 (2004).

6. Tee, B. C.-K. *et al.* A skin-inspired organic digital mechanoreceptor. *Science* **350,** 313-316 (2015).

7. Atzori, L., Iera, A. & Morabito, G. The Internet of Things: A survey. *Computer Networks* **54,** 2787-2805 (2010).

8. Finkenzeller, K. *RFID Handbook*. John Wiley & Sons, Ltd, 2010.

9. Naber, R. C. G., Blom, P. W. M., Marsman, A. W. & de Leeuw, D. M. Low voltage switching of a spin cast ferroelectric polymer. *Appl. Phys. Lett.* **85,** 2032-2034 (2004).

10. Naber, R. C. G. *et al.* High-performance solution-processed polymer ferroelectric field-effect transistors. *Nat. Mater.* **4,** 243-248 (2005).

11. Asadi, K., de Leeuw, D. M., de Boer, B. & Blom, P. W. M. Organic non-volatile memories from ferroelectric phase-separated blends. *Nat. Mater.* **7,** 547-550 (2008).

12. Gelinck, G. H. *et al.* All-polymer ferroelectric transistors. *Appl. Phys. Lett.* **87,** 092903 (2005).

13. Naber, R. C. G., de Boer, B., Blom, P. W. M. & de Leeuw, D. M. Low-voltage polymer field-effect transistors for nonvolatile memories. *Appl. Phys. Lett.* **87,** 203509 (2005).

14. Naber, R. C. G., Mulder, M., de Boer, B., Blom, P. W. M. & de Leeuw, D. M. High charge density and mobility in poly(3-hexylthiophene) using a polarizable gate dielectric. *Org. Electron.* **7,** 132-136 (2006).

15. Naber, R. C. G. *et al.* Origin of the drain current bistability in polymer ferroelectric field-effect transistors. *Appl. Phys. Lett.* **90,** 113509 (2007).

16. Nguyen, C. A., Mhaisalkar, S. G., Ma, J. & Lee, P. S. Enhanced organic ferroelectric field effect transistor characteristics with strained poly(vinylidene fluoride-trifluoroethylene) dielectric. *Org. Electron.* **9,** 1087-1092 (2008).

17. Brondijk, J. J., Asadi, K., Blom, P. W. M. & de Leeuw, D. M. Physics of organic ferroelectric field-effect transistors. *J. Polym. Sci., Part B: Polym. Phys.* **50,** 47-54 (2012).

18. Kam, B. *et al.* Origin of multiple memory states in organic ferroelectric field-effect transistors. *Appl. Phys. Lett.* **101,** 033304 (2012).

19. van Breemen, A. *et al.* Ferroelectric transistor memory arrays on flexible foils. *Org. Electron.* **14,** 1966-1971 (2013).

20. Gelinck, G. H., van Breemen, A. J. J. M. & Cobb, B. Ferroelectric switching of poly(vinylidene difluoride-trifluoroethylene) in metal-ferroelectric-semiconductor non-volatile memories with an amorphous oxide semiconductor. *Appl. Phys. Lett.* **106,** 093503 (2015).

21. Katsouras, I. *et al.* Controlling the on/off current ratio of ferroelectric field-effect transistors. *Sci. Rep.* **5,** 12094 (2015).

22. Valasek, J. Piezo-Electric and Allied Phenomena in Rochelle Salt. *Phys. Rev.* **17,** 475-481 (1921).

23. Haertling, G. H. Ferroelectric Ceramics: History and Technology. *J. Am. Ceram. Soc.* **82,** 797-818 (1999).

24. Scott, J. F. Applications of Modern Ferroelectrics. *Science* **315,** 954-959 (2007).

25. Hari Singh Nalwa. *Ferroelectric polymers: Chemistry, physics, and applications.* WILEY-VCH Verlag GmbH: New York, 1995.

26. Kepler, R. G. & Anderson, R. A. Ferroelectric polymers. *Adv. Phys.* **41,** 1-57 (1992).

27. Horiuchi, S. & Tokura, Y. Organic ferroelectrics. *Nat. Mater.* **7,** 357-366 (2008).

28. Lovinger, A. J. Ferroelectric Polymers. *Science* **220,** 1115-1121 (1983).

29. Newman, B. A., Scheinbeim, J. I., Lee, J. W. & Takase, Y. A new class of ferroelectric polymers, the odd-numbered nylons. *Ferroelectrics* **127,** 229-234 (1992).

30. Goldsmith, G. J. & White, J. G. Ferroelectric Behavior of Thiourea. *The Journal of Chemical Physics* **31,** 1175-1187 (1959).

31. Kapitza, H. *et al.* Ferroelectric liquid crystalline polysiloxanes with high spontaneous polarization and possible applications in nonlinear optics. *Adv. Mater.* **2,** 539-543 (1990).

32. Horiuchi, S. *et al.* Ferroelectricity near room temperature in co-crystals of nonpolar organic molecules. *Nat. Mater.* **4,** 163-166 (2005).

33. Shimada, T. & Kitamura, T. Multi-physics Properties in Ferroelectric Nanowires and Related Structures from First-principles. In: Prete P (ed). *Nanowires*. InTech, 2010.

34. Heiji, K. The Piezoelectricity of Poly (vinylidene Fluoride). *Jpn. J. Appl. Phys.* **8,** 975 (1969).

35. Kepler, R. G. & Anderson, R. A. Ferroelectricity in polyvinylidene fluoride. *J. Appl. Phys.* **49,** 1232-1235 (1978).

36. Katsouras, I. *et al.* The negative piezoelectric effect of the ferroelectric polymer poly(vinylidene fluoride). *Nat. Mater.* **15,** 78-84 (2016).

37. Tagantsev, A. K., Cross, L. E. & Fousek, J. *Domains in Ferroic Crystals and Thin Films*. Springer: New York, 2010.

38. Furukawa, T. Ferroelectric properties of vinylidene fluoride copolymers. *Phase Transitions* **18,** 143-211 (1989).

39. Chinaglia, D. L. *et al.* Influence of the solvent evaporation rate on the crystalline phases of solution-cast poly(vinylidene fluoride) films. *Journal of Applied Polymer Science* **116,** 785-791 (2010).

40. Prest, W. M. & Luca, D. J. The formation of the γ phase from the α and β polymorphs of polyvinylidene fluoride. *J. Appl. Phys.* **49,** 5042-5047 (1978).

41. Kang, S. J. *et al.* Fabrication of micropatterned ferroelectric gamma poly(vinylidene fluoride) film for non-volatile polymer memory. *Journal of Materials Chemistry* **21,** 3619-3624 (2011).

42. Li, M. *et al.* Revisiting the δ-phase of poly(vinylidene fluoride) for solution-processed ferroelectric thin films. *Nat. Mater.* **12,** 433-438 (2013).

43. Martins, P., Lopes, A. C. & Lanceros-Mendez, S. Electroactive phases of poly(vinylidene fluoride): Determination, processing

and applications. *Progress in Polymer Science* **39,** 683-706 (2014).

44. Wang, F. *et al.* Ionic-liquid-induced ferroelectric polarization in poly(vinylidene fluoride) thin films. *Appl. Phys. Lett.* **100,** 062903 (2012).

45. Kang, S. J. *et al.* Printable Ferroelectric PVDF/PMMA Blend Films with Ultralow Roughness for Low Voltage Non-Volatile Polymer Memory. *Adv. Funct. Mater.* **19,** 2812-2818 (2009).

46. Li, M. *et al.* Ferroelectric Phase Diagram of PVDF:PMMA. *Macromolecules* **45,** 7477-7485 (2012).

47. Takeo, F., Munehiro, D., Eiichi, F., Yoshiro, T. & Akio, C. Ferroelectric Behavior in the Copolymer of Vinylidenefluoride and Trifluoroethylene. *Jpn. J. Appl. Phys.* **19,** L109 (1980).

48. Poulsen, M. & Ducharme, S. Why ferroelectric polyvinylidene fluoride is special. *IEEE Trans. Dielectr. Electr. Insul.* **17,** 1028-1035 (2010).

49. Lee, J. S., Prabu, A. A. & Kim, K. J. Annealing effect upon chain orientation, crystalline morphology, and polarizability of ultra-thin P(VDF-TrFE) film for nonvolatile polymer memory device. *Polymer* **51,** 6319-6333 (2010).

50. Murata, Y. & Koizumi, N. Curie Transition in Copolymers of Vinylidene Fluoride and Tetrafluoroethylene. *Polym. J.* **17,** 1071-1074 (1985).

51. Yagi, T., Tatemoto, M. & Sako, J.-i. Transition Behavior and Dielectric Properties in Trifluoroethylene and Vinylidene Fluoride Copolymers. *Polym. J.* **12,** 209-223 (1980).

52. Lovinger, A. J., Furukawa, T., Davis, G. T. & Broadhurst, M. G. Curie transitions in copolymers of vinylidene fluoride. *Ferroelectrics* **50,** 227-236 (1983).

53. Lovinger, A. J., Furukawa, T., Davis, G. T. & Broadhurst, M. G. Crystallographic changes characterizing the Curie transition

in three ferroelectric copolymers of vinylidene fluoride and trifluoroethylene: 1. As-crystallized samples. *Polymer* **24,** 1225-1232 (1983).

54. Lovinger, A. J., Furukawa, T., Davis, G. T. & Broadhurst, M. G. Crystallographic changes characterizing the Curie transition in three ferroelectric copolymers of vinylidene fluoride and trifluoroethylene: 2. Oriented or poled samples. *Polymer* **24,** 1233-1239 (1983).

55. Tashiro, K., Takano, K., Kobayashi, M., Chatani, Y. & Tadokoro, H. Structure and ferroelectric phase transition of vinylidene fluoride-trifluoroethylene copolymers: 2. VDF 55% copolymer. *Polymer* **25,** 195-208 (1984).

56. Faria, L. O. & Moreira, R. L. Infrared spectroscopic investigation of chain conformations and interactions in P(VDF-TrFE)/PMMA blends. *J. Polym. Sci., Part B: Polym. Phys.* **38,** 34-40 (2000).

57. Kassa, H. G. *et al.* Structure and Ferroelectric Properties of Nanoimprinted Poly(vinylidene fluoride-ran-trifluoroethylene). *Macromolecules* **46,** 8569-8579 (2013).

58. Hu, Z., Tian, M., Nysten, B. & Jonas, A. M. Regular arrays of highly ordered ferroelectric polymer nanostructures for non-volatile low-voltage memories. *Nat. Mater.* **8,** 62-67 (2009).

59. Mao, D., Gnade, B. E. & Quevedo-Lopez, M. A. Ferroelectric Properties and Polarization Switching Kinetic of Poly (vinylidene fluoride-trifluoroethylene) Copolymer. In: Lallart M (ed). *Ferroelectrics - Physical Effects*. InTech, 2011.

60. Wu, Y. *et al.* Confinement Induced Preferential Orientation of Crystals and Enhancement of Properties in Ferroelectric Polymer Nanowires. *ACS Macro Lett.* **2,** 535-538 (2013).

61. Kassa, H. G. *et al.* The Ferro- to Paraelectric Curie Transition of a Strongly Confined Ferroelectric Polymer. *Macromolecules* **47,** 4711-4717 (2014).

62. Wu, Y., Li, X., Jonas, A. M. & Hu, Z. Two-Step Polarization Switching in Ferroelectric Polymers. *Phys. Rev. Lett.* **115,** 267601 (2015).

63. Hu, W. J. *et al.* Universal Ferroelectric Switching Dynamics of Vinylidene Fluoride-trifluoroethylene Copolymer Films. *Sci. Rep.* **4,** 4772 (2014).

64. Gruverman, A., Wu, D. & Scott, J. F. Piezoresponse Force Microscopy Studies of Switching Behavior of Ferroelectric Capacitors on a 100-ns Time Scale. *Phys. Rev. Lett.* **100,** 097601 (2008).

65. Zhao, D., Katsouras, I., Asadi, K., Blom, P. W. M. & de Leeuw, D. M. Switching dynamics in ferroelectric P(VDF-TrFE) thin films. *Phys. Rev. B* **92,** 214115 (2015).

66. Tagantsev, A. K., Stolichnov, I., Setter, N., Cross, J. S. & Tsukada, M. Non-Kolmogorov-Avrami switching kinetics in ferroelectric thin films. *Phys. Rev. B* **66,** 214109 (2002).

67. Mao, D., Mejia, I., Stiegler, H., Gnade, B. E. & Quevedo-Lopez, M. A. Polarization behavior of poly(vinylidene fluoride-trifluoroethylene) copolymer ferroelectric thin film capacitors for nonvolatile memory application in flexible electronics. *J. Appl. Phys.* **108,** 094102 (2010).

68. Sharma, P., Reece, T. J., Ducharme, S. & Gruverman, A. High-Resolution Studies of Domain Switching Behavior in Nanostructured Ferroelectric Polymers. *Nano Lett.* **11,** 1970-1975 (2011).

69. Xiao, Z., Poddar, S., Ducharme, S. & Hong, X. Domain wall roughness and creep in nanoscale crystalline ferroelectric polymers. *Appl. Phys. Lett.* **103,** 112903 (2013).

70. Chen, X.-Z. *et al.* Nano-Imprinted Ferroelectric Polymer Nanodot Arrays for High Density Data Storage. *Adv. Funct. Mater.* **23,** 3124-3129 (2013).

71. Global Semidonductor Sales Report 2015. [cited 2016 April 4]Available from: http://www.semiconductors.org/news/global_sales_report_2015/

72. Chiang, C. K. *et al.* Electrical Conductivity in Doped Polyacetylene. *Phys. Rev. Lett.* **39,** 1098-1101 (1977).

73. Shirakawa, H., Louis, E. J., MacDiarmid, A. G., Chiang, C. K. & Heeger, A. J. Synthesis of electrically conducting organic polymers: halogen derivatives of polyacetylene, (CH). *Journal of the Chemical Society, Chemical Communications* 578-580 (1977).

74. The Nobel Prize in Chemistry 2000. [cited 2016 April 2]Available from: http://www.nobelprize.org/nobel_prizes/chemistry/laureates/2000/

75. Facchetti, A. Semiconductors for organic transistors. *Mater. Today* **10,** 28-37 (2007).

76. Veres, J., Ogier, S. D., Leeming, S. W., Cupertino, D. C. & Mohialdin Khaffaf, S. Low-k Insulators as the Choice of Dielectrics in Organic Field-Effect Transistors. *Adv. Funct. Mater.* **13,** 199-204 (2003).

77. Zhang, W. *et al.* Systematic Improvement in Charge Carrier Mobility of Air Stable Triarylamine Copolymers. *J. Am. Chem. Soc.* **131,** 10814-10815 (2009).

78. Kittel, C. *Introduction to Solid State Physics*, 8th edn, 2004.

79. Jiles, D. C. *Introduction to Magnetism and Magnetic Materials*. CRC Press, 1998.

80. Engdahl, G. *Handbook of Giant Magnetostrictive Materials*, 1st edn. Academic Press, 1999.

81. Bozorth, R. M. *Ferromagnetism,* 8th edn. Van Nostrand: Princeton, 1964.

82. Ferromagnetic Materials. [cited 2016 April 5]Available from: http://www.doitpoms.ac.uk/tlplib/ferromagnetic/index.php

83. Olabi, A. G. & Grunwald, A. Design and application of magnetostrictive materials. *Materials & Design* **29,** 469-483 (2008).

84. Xu, H., Zhong, J., Liu, X., Chen, J. & Shen, D. Ferroelectric and switching behavior of poly(vinylidene fluoride-trifluoroethylene) copolymer ultrathin films with polypyrrole interface. *Appl. Phys. Lett.* **90,** 092903 (2007).

85. Takeo, F., Hisashi, M., Masahiro, S. & Yoshiro, T. Nanosecond Switching in Thin Fims of Vinylidene Fluoride/Trilluoroethylene Copolymers. *Jpn. J. Appl. Phys.* **24,** L661 (1985).

86. Yoshiro, T. Effects of Thickness on Ferroelectricity in Vinylidene Fluoride and Trifluoroethylene Copolymers. *Jpn. J. Appl. Phys.* **34,** 5418 (1995).

87. Bune, A. V. *et al.* Two-dimensional ferroelectric films. *Nature* **391,** 874-877 (1998).

88. Vizdrik, G., Ducharme, S., Fridkin, V. M. & Yudin, S. G. Kinetics of ferroelectric switching in ultrathin films. *Phys. Rev. B* **68,** 094113 (2003).

89. Ducharme, S., Reece, T. J., Othon, C. M. & Rannow, R. K. Ferroelectric polymer Langmuir-Blodgett films for nonvolatile memory applications. *IEEE Trans. Device Mater. Rel.* **5,** 720-735 (2005).

90. Zhang, Q. M. *et al.* Critical thickness of crystallization and discontinuous change in ferroelectric behavior with thickness in ferroelectric polymer thin films. *J. Appl. Phys.* **89,** 2613-2616 (2001).

91. Xia, F., Razavi, B., Xu, H., Cheng, Z.-Y. & Zhang, Q. M. Dependence of threshold thickness of crystallization and film morphology on film processing conditions in poly(vinylidene fluoride–trifluoroethylene) copolymer thin films. *J. Appl. Phys.* **92,** 3111-3115 (2002).

92. Müller, K. *et al.* Microscopic and spectroscopic characterization of interfaces and dielectric layers for OFET devices. *Phys. Status Solidi A* **205,** 600-611 (2008).

93. Furukawa, T., Nakajima, T. & Takahashi, Y. Factors governing ferroelectric switching characteristics of thin VDF/TrFE copolymer films. *IEEE Trans. Dielectr. Electr. Insul.* **13,** 1120-1131 (2006).

94. Naber, R. C. G., Blom, P. W. M. & Leeuw, D. M. d. Comment on 'Extrinsic versus intrinsic ferroelectric switching: experimental investigations using ultra-thin PVDF Langmuir–Blodgett films'. *J. Phys. D: Appl. Phys.* **39,** 1984 (2006).

95. Li, M. *et al.* Controlling the microstructure of poly(vinylidene-fluoride) (PVDF) thin films for microelectronics. *J. Mater. Chem. C* **1,** 2050-7526 (2013).

96. Liu, Y., Weiss, D. N. & Li, J. Rapid Nanoimprinting and Excellent Piezoresponse of Polymeric Ferroelectric Nanostructures. *ACS Nano* **4,** 83-90 (2010).

97. Fang, J.-R. *et al.* Influence of nano-embossing on properties of poly(VDF-TrFE). *Microelectron. Eng.* **87,** 890-892 (2010).

98. Martínez-Tong, D. E. *et al.* Improving information density in ferroelectric polymer films by using nanoimprinted gratings. *Appl. Phys. Lett.* **102,** 191601 (2013).

99. Lenz, T. *et al.* Microstructured organic ferroelectric thin film capacitors by solution micromolding. *Phys. Status Solidi A* **212,** 2124-2132 (2015).

100. Zhao, D. *et al.* Polarization fatigue of organic ferroelectric capacitors. *Sci. Rep.* **4,** 5075 (2014).

101. Asadi, K., de Boer, T. G., Blom, P. W. M. & de Leeuw, D. M. Tunable Injection Barrier in Organic Resistive Switches Based on Phase-Separated Ferroelectric–Semiconductor Blends. *Adv. Funct. Mater.* **19,** 3173-3178 (2009).

102. Kemerink, M., Asadi, K., Blom, P. W. M. & de Leeuw, D. M. The operational mechanism of ferroelectric-driven organic resistive switches. *Org. Electron.* **13,** 147-152 (2012).

103. Li, M. *et al.* Processing and Low Voltage Switching of Organic Ferroelectric Phase-Separated Bistable Diodes. *Adv. Funct. Mater.* **22,** 2750-2757 (2012).

104. van Breemen, A. *et al.* Surface Directed Phase Separation of Semiconductor Ferroelectric Polymer Blends and their Use in Non-Volatile Memories. *Adv. Funct. Mater.* **25,** 278-286 (2015).

105. Nougaret, L. *et al.* Nanoscale Design of Multifunctional Organic Layers for Low-Power High-Density Memory Devices. *ACS Nano* **8,** 3498-3505 (2014).

106. Scott, J. C. Is There an Immortal Memory? *Science* **304,** 62-63 (2004).

107. Yang, Y., Ouyang, J., Ma, L., Tseng, R. J. H. & Chu, C. W. Electrical Switching and Bistability in Organic/Polymeric Thin Films and Memory Devices. *Adv. Funct. Mater.* **16,** 1001-1014 (2006).

108. Asadi, K., Li, M., Stingelin, N., Blom, P. W. M. & de Leeuw, D. M. Crossbar memory array of organic bistable rectifying diodes for nonvolatile data storage. *Appl. Phys. Lett.* **97,** 193308 (2010).

109. Braun, D. Crosstalk in passive matrix polymer LED displays. *Synthetic Metals* **92,** 107-113 (1998).

110. Sempel, A. & Büchel, M. Design aspects of low power polymer/OLED passive-matrix displays. *Org. Electron.* **3,** 89-92 (2002).

111. Asadi, K., Blom, P. W. M. & de Leeuw, D. M. The MEMOLED: Active Addressing with Passive Driving. *Adv. Mater.* **23,** 865-868 (2011).

112. Lazareva, I. *et al.* Interface screening and imprint in poly(vinylidene fluoride/trifluoroethylene) ferroelectric field effect transistors. *J. Appl. Phys.* **105,** 054110 (2009).

113. Lee, K. H., Lee, G., Lee, K., Oh, M. S. & Im, S. Flexible low voltage nonvolatile memory transistors with pentacene channel and ferroelectric polymer. *Appl. Phys. Lett.* **94,** 093304 (2009).

114. Das, S. & Appenzeller, J. FETRAM. An Organic Ferroelectric Material Based Novel Random Access Memory Cell. *Nano Lett.* **11,** 4003-4007 (2011).

115. Huynh Van, N., Lee, J.-H., Whang, D. & Kang, D. J. Ultralow-power non-volatile memory cells based on P(VDF-TrFE) ferroelectric-gate CMOS silicon nanowire channel field-effect transistors. *Nanoscale* **7,** 11660-11666 (2015).

116. Hill, N. A. Density Functional Studies of Multiferroic Magnetoelectrics. *Annual Review of Materials Research* **32,** 1-37 (2002).

117. Gajek, M. *et al.* Tunnel junctions with multiferroic barriers. *Nat. Mater.* **6,** 296-302 (2007).

118. Scott, J. F. Data storage: Multiferroic memories. *Nat. Mater.* **6,** 256-257 (2007).

119. Martin, L. W. *et al.* Multiferroics and magnetoelectrics: thin films and nanostructures. *Journal of Physics: Condensed Matter* **20,** 434220 (2008).

120. Kimura, T. *et al.* Magnetic control of ferroelectric polarization. *Nature* **426,** 55-58 (2003).

121. Hur, N. *et al.* Electric polarization reversal and memory in a multiferroic material induced by magnetic fields. *Nature* **429,** 392-395 (2004).

122. Zheng, H. *et al.* Multiferroic BaTiO3-CoFe2O4 Nanostructures. *Science* **303,** 661-663 (2004).

123. Nan, C.-W., Liu, G., Lin, Y. & Chen, H. Magnetic-Field-Induced Electric Polarization in Multiferroic Nanostructures. *Phys. Rev. Lett.* **94,** 197203 (2005).

124. Eerenstein, W., Mathur, N. D. & Scott, J. F. Multiferroic and magnetoelectric materials. *Nature* **442,** 759-765 (2006).

125. Yamasaki, Y. *et al.* Magnetic Reversal of the Ferroelectric Polarization in a Multiferroic Spinel Oxide. *Phys. Rev. Lett.* **96,** 207204 (2006).

126. Zhao, T. *et al.* Electrical control of antiferromagnetic domains in multiferroic BiFeO3 films at room temperature. *Nat. Mater.* **5,** 823-829 (2006).

127. Cheong, S.-W. & Mostovoy, M. Multiferroics: a magnetic twist for ferroelectricity. *Nat. Mater.* **6,** 13-20 (2007).

128. Zavaliche, F. *et al.* Electrically Assisted Magnetic Recording in Multiferroic Nanostructures. *Nano Lett.* **7,** 1586-1590 (2007).

129. Chu, Y.-H. *et al.* Electric-field control of local ferromagnetism using a magnetoelectric multiferroic. *Nat. Mater.* **7,** 478-482 (2008).

130. Garcia, V. *et al.* Ferroelectric Control of Spin Polarization. *Science* **327,** 1106-1110 (2010).

131. Vaz, C. A. F., Hoffman, J., Ahn, C. H. & Ramesh, R. Magnetoelectric Coupling Effects in Multiferroic Complex

Oxide Composite Structures. *Adv. Mater.* **22,** 2900-2918 (2010).

132. Wang, Y., Hu, J., Lin, Y. & Nan, C.-W. Multiferroic magnetoelectric composite nanostructures. *NPG Asia Mater* **2,** 61-68 (2010).

133. Wu, S. M. *et al.* Reversible electric control of exchange bias in a multiferroic field-effect device. *Nat. Mater.* **9,** 756-761 (2010).

134. Martins, P. *et al.* Optimizing piezoelectric and magnetoelectric responses on CoFe 2 O 4 /P(VDF-TrFE) nanocomposites. *J. Phys. D: Appl. Phys.* **44,** 495303 (2011).

135. Zhang, X. *et al.* The spin state of a molecular adsorbate driven by the ferroelectric substrate polarization. *Chemical Communications* **50,** 2255-2257 (2014).

136. Aimon, N. M., Kim, D. H., Sun, X. & Ross, C. A. Multiferroic Behavior of Templated BiFeO3–CoFe2O4 Self-Assembled Nanocomposites. *ACS Appl. Mater. Inter.* **7,** 2263-2268 (2015).

137. Chou, S. Y., Krauss, P. R. & Renstrom, P. J. Imprint of sub‐25 nm vias and trenches in polymers. *Appl. Phys. Lett.* **67,** 3114-3116 (1995).

138. Heyderman, L. J., Schift, H., David, C., Gobrecht, J. & Schweizer, T. Flow behaviour of thin polymer films used for hot embossing lithography. *Microelectron. Eng.* **54,** 229-245 (2000).

139. Studer, V., Pépin, A. & Chen, Y. Nanoembossing of thermoplastic polymers for microfluidic applications. *Appl. Phys. Lett.* **80,** 3614-3616 (2002).

140. Chou, S. Y., Krauss, P. R. & Renstrom, P. J. Imprint Lithography with 25-Nanometer Resolution. *Science* **272,** 85-87 (1996).

141. Chou, S. Y., Krauss, P. R. & Renstrom, P. J. Nanoimprint lithography. *Journal of Vacuum Science & Technology B* **14,** 4129-4133 (1996).

142. Chou, S. Y., Krauss, P. R., Zhang, W., Guo, L. & Zhuang, L. Sub-10 nm imprint lithography and applications. *Journal of Vacuum Science & Technology B* **15,** 2897-2904 (1997).

143. Austin, M. D. *et al.* Fabrication of 5nm linewidth and 14nm pitch features by nanoimprint lithography. *Appl. Phys. Lett.* **84,** 5299-5301 (2004).

144. Hu, Z. *et al.* High-Throughput Fabrication of Organic Nanowire Devices with Preferential Internal Alignment and Improved Performance. *Nano Lett.* **7,** 3639-3644 (2007).

145. Binnig, G., Rohrer, H., Gerber, C. & Weibel, E. Surface Studies by Scanning Tunneling Microscopy. *Phys. Rev. Lett.* **49,** 57-61 (1982).

146. Binnig, G., Rohrer, H., Gerber, C. & Weibel, E. Tunneling through a controllable vacuum gap. *Appl. Phys. Lett.* **40,** 178-180 (1982).

147. The Nobel Prize in Physics 1986. [cited 2016 March 25]Available from: http://www.nobelprize.org/nobel_prizes/physics/laureates/1986/index.html

148. Binnig, G., Quate, C. F. & Gerber, C. Atomic Force Microscope. *Phys. Rev. Lett.* **56,** 930-933 (1986).

149. Scanning Probe Microscopy. [cited 2013 April 5]Available from: http://www.eng.utah.edu/~lzang/images/Lecture_4_SPM.pdf

150. Atomic Force Microscopy. [cited 2016 April 5]Available from: http://www.doitpoms.ac.uk/tlplib/afm/index.php

151. Sergei, V. K., Anna, N. M., Long Qing, C. & Brian, J. R. Local polarization dynamics in ferroelectric materials. *Rep. Prog. Phys.* **73,** 056502 (2010).

152. Elisabeth, S. Piezoresponse force microscopy (PFM). *J. Phys. D: Appl. Phys.* **44,** 464003 (2011).

153. Sader, J. E. Frequency response of cantilever beams immersed in viscous fluids with applications to the atomic force microscope. *J. Appl. Phys.* **84,** 64-76 (1998).

154. Proksch, R. & Kalinin, S. V. Piezoresponse Force Microscopy with Asylum Research AFMs, PFM Application Note. (2008).

155. Vasudevan, R. K., Jesse, S., Kim, Y., Kumar, A. & Kalinin, S. V. Spectroscopic imaging in piezoresponse force microscopy: New opportunities for studying polarization dynamics in ferroelectrics and multiferroics. *MRS Communications* **2,** 61-73 (2012).

156. Jesse, S., Mirman, B. & Kalinin, S. V. Resonance enhancement in piezoresponse force microscopy: Mapping electromechanical activity, contact stiffness, and Q factor. *Appl. Phys. Lett.* **89,** 022906 (2006).

157. Stephen, J., Sergei, V. K., Roger, P., Baddorf, A. P. & Rodriguez, B. J. The band excitation method in scanning probe microscopy for rapid mapping of energy dissipation on the nanoscale. *Nanotechnology* **18,** 435503 (2007).

158. Brian, J. R., Clint, C., Sergei, V. K. & Roger, P. Dual-frequency resonance-tracking atomic force microscopy. *Nanotechnology* **18,** 475504 (2007).

159. Kassa, H. G. Electrical and structural properties of nano-imprinted ferroelectric polymers. *PhD thesis* (2014).

160. Furukawa, T., Kanai, S., Okada, A., Takahashi, Y. & Yamamoto, R. Ferroelectric switching dynamics in VDF-TrFE copolymer thin films spin coated on Si substrate. *J. Appl. Phys.* **105,** 061636 (2009).

161. Heremans, P. *et al.* Polymer and Organic Nonvolatile Memory Devices. *Chem. Mater.* **23,** 341-358 (2011).

162. Chandra, P. & Littlewood, P. B. A Landau Primer for Ferroelectrics. *Physics of Ferroelectrics: A modern Perspective*, *Topics Applied Physics* **105,** 69-116 (2007).

163. Cai, R. *et al.* An organic ferroelectric field effect transistor with poly(vinylidene fluoride-co-trifluoroethylene) nanostripes as gate dielectric. *Appl. Phys. Lett.* **105,** 113113 (2014).

164. Ruiz, R., Papadimitratos, A., Mayer, A. C. & Malliaras, G. G. Thickness Dependence of Mobility in Pentacene Thin-Film Transistors. *Adv. Mater.* **17,** 1795-1798 (2005).

165. Shi, J., Jiang, D.-T., Dutcher, J. R. & Qin, X.-R. Thickness-dependent mobility in tetracene thin-film field-effect-transistors. *J. Vac. Sci. Technol. B* **33,** 050604 (2015).

166. Logan, S., Donaghey, J. E., Zhang, W., McCulloch, I. & Campbell, A. J. Compatibility of amorphous triarylamine copolymers with solution-processed hole injecting metal oxide bottom contacts. *J. Mater. Chem. C* **3,** 4530-4536 (2015).

167. Reece, T. J., Ducharme, S., Sorokin, A. V. & Poulsen, M. Nonvolatile memory element based on a ferroelectric polymer Langmuir–Blodgett film. *Appl. Phys. Lett.* **82,** 142-144 (2003).

168. Narayanan Unni, K. N., de Bettignies, R., Dabos-Seignon, S. & Nunzi, J.-M. A nonvolatile memory element based on an organic field-effect transistor. *Appl. Phys. Lett.* **85,** 1823-1825 (2004).

169. Lim, S. H., Rastogi, A. C. & Desu, S. B. Electrical properties of metal-ferroelectric-insulator-semiconductor structures based on ferroelectric polyvinylidene fluoride copolymer film gate for nonvolatile random access memory application. *J. Appl. Phys.* **96,** 5673-5682 (2004).

170. Naber, R. C. G. *et al.* High-performance solution-processed polymer ferroelectric field-effect transistors. *Nat Mater* **4,** 243-248 (2005).

171. Knotts, G., Bhaumik, A., Ghosh, K. & Guha, S. Enhanced performance of ferroelectric-based all organic capacitors and transistors through choice of solvent. *Applied Physics Letters* **104,** 233301 (2014).

172. Kang, S. J. *et al.* Non-volatile Ferroelectric Poly(vinylidene fluoride-co-trifluoroethylene) Memory Based on a Single-Crystalline Tri-isopropylsilylethynyl Pentacene Field-Effect Transistor. *Advanced Functional Materials* **19,** 1609-1616 (2009).

173. Lee, H. J., Kim, Y.-J., Lee, E., Yao, K. & Jo, J. Y. Topography engineering of ferroelectric crystalline copolymer film. *Organic Electronics* **15,** 751-757 (2014).

174. Lutkenhaus, J. L., McEnnis, K., Serghei, A. & Russell, T. P. Confinement Effects on Crystallization and Curie Transitions of Poly(vinylidene fluoride-co-trifluoroethylene). *Macromolecules* **43,** 3844-3850 (2010).

175. Asadi, K., Li, M., Blom, P. W. M., Kemerink, M. & de Leeuw, D. M. Organic ferroelectric opto-electronic memories. *Mater. Today* **14,** 592-599 (2011).

176. Yuan, Y. *et al.* Understanding the effect of ferroelectric polarization on power conversion efficiency of organic photovoltaic devices. *Energy & Environmental Science* **5,** 8558-8563 (2012).

177. Yang, B. *et al.* Tuning the Energy Level Offset between Donor and Acceptor with Ferroelectric Dipole Layers for Increased Efficiency in Bilayer Organic Photovoltaic Cells. *Adv. Mater.* **24,** 1455-1460 (2012).

178. Yuan, Y. *et al.* Efficiency enhancement in organic solar cells with ferroelectric polymers. *Nat. Mater.* **10,** 296-302 (2011).

179. Yang, S. Y. *et al.* Above-bandgap voltages from ferroelectric photovoltaic devices. *Nat. Nano.* **5,** 143-147 (2010).

180. Cai, R. & Jonas, A. M. Local Maps of the Polarization and Depolarization in Organic Ferroelectric Field-Effect Transistors. *Sci. Rep.* (2016).

181. Min, S.-Y. *et al.* Large-scale organic nanowire lithography and electronics. *Nat Commun* **4,** 1773 (2013).

182. Xu, W. *et al.* N-Doped Graphene Field-Effect Transistors with Enhanced Electron Mobility and Air-Stability. *Small* **10,** 1999-2005 (2014).

183. Xu, W. *et al.* Rapid Fabrication of Designable Large-Scale Aligned Graphene Nanoribbons by Electro-hydrodynamic Nanowire Lithography. *Adv. Mater.* **26,** 3459-3464 (2014).

184. Xu, W. *et al.* Controllable n-Type Doping on CVD-Grown Single- and Double-Layer Graphene Mixture. *Adv. Mater.* **27,** 1619-1623 (2015).

185. Xu, W., Lee, Y., Min, S.-Y., Park, C. & Lee, T.-W. Simple, Inexpensive, and Rapid Approach to Fabricate Cross-Shaped Memristors Using an Inorganic-Nanowire-Digital-Alignment Technique and a One-Step Reduction Process. *Adv. Mater.* **28,** 527-532 (2016).

186. Liao, L. *et al.* Ferroelectric Transistors with Nanowire Channel: Toward Nonvolatile Memory Applications. *ACS Nano* **3,** 700-706 (2009).

187. Ebata, H. *et al.* Highly Soluble [1]Benzothieno[3,2-b]benzothiophene (BTBT) Derivatives for High-Performance, Solution-Processed Organic Field-Effect Transistors. *J. Am. Chem. Soc.* **129,** 15732-15733 (2007).

188. Babel, A. & Jenekhe, S. A. High Electron Mobility in Ladder Polymer Field-Effect Transistors. *J. Am. Chem. Soc.* **125,** 13656-13657 (2003).

189. Ramesh, R. & Spaldin, N. A. Multiferroics: progress and prospects in thin films. *Nat. Mater.* **6,** 21-29 (2007).

190. Stroppa, A., Barone, P., Jain, P., Perez-Mato, J. M. & Picozzi, S. Hybrid Improper Ferroelectricity in a Multiferroic and Magnetoelectric Metal-Organic Framework. *Adv. Mater.* **25,** 2284-2290 (2013).

191. Gómez-Aguirre, L. C. *et al.* Magnetic Ordering-Induced Multiferroic Behavior in [CH3NH3][Co(HCOO)3] Metal–Organic Framework. *J. Am. Chem. Soc.* **138,** 1122-1125 (2016).

192. van Breemen, A. J. J. M. *et al.* Photocrosslinking of ferroelectric polymers and its application in three-dimensional memory arrays. *Appl. Phys. Lett.* **98,** 183302 (2011).

193. Cai, R. & Jonas, A. M. Local Maps of the Polarization and Depolarization in Organic Ferroelectric Field-Effect Transistors. *Sci. Rep.* **6,** 22116 (2016).

194. Cai, R. *et al.* Organic Ferroelectric/Semiconducting Nanowire Hybrid Layer for Memory Storage. *Nanoscale* (2016).

195. Miller, J. S. & Epstein, A. J. Organic and Organometallic Molecular Magnetic Materials—Designer Magnets. *Angewandte Chemie International Edition in English* **33,** 385-415 (1994).

196. Choi, Y.-Y. *et al.* Enhancement of Local Piezoresponse in Polymer Ferroelectrics via Nanoscale Control of Microstructure. *ACS Nano* (2015).

197. Kalinin, S. V., Karapetian, E. & Kachanov, M. Nanoelectromechanics of piezoresponse force microscopy. *Phys. Rev. B* **70,** 184101 (2004).

198. Wen, Z., Li, C., Wu, D., Li, A. & Ming, N. Ferroelectric-field-effect-enhanced electroresistance in metal/ferroelectric/semiconductor tunnel junctions. *Nat. Mater.* **12,** 617-621 (2013).

199. Schmitz-Antoniak, C. *et al.* Electric in-plane polarization in multiferroic CoFe2O4/BaTiO3 nanocomposite tuned by magnetic fields. *Nat Commun* **4,** (2013).

200. Metlov, K. L. & Guslienko, K. Y. Stability of magnetic vortex in soft magnetic nano-sized circular cylinder. *Journal of Magnetism and Magnetic Materials* **242–245, Part 2,** 1015-1017 (2002).

201. Lepadatu, S., Stewart, M. & Cain, M. G. Quantification of electromechanical coupling measured with piezoresponse force microscopy. *J. Appl. Phys.* **116,** 066806 (2014).

202. Mai, M., Leschhorn, A. & Kliem, H. The field and temperature dependence of hysteresis loops in P(VDF–TrFE) copolymer films. *Physica B: Condensed Matter* **456,** 306-311 (2015).

203. Schmiedeshoff, G. M. *et al.* Versatile and compact capacitive dilatometer. *Rev. Sci. Instrum.* **77,** 123907 (2006).

204. Bozorth, R. M., Tilden, E. F. & Williams, A. J. Anisotropy and Magnetostriction of Some Ferrites. *Phys. Rev.* **99,** 1788-1798 (1955).

205. Oh, Y. S. *et al.* Quantitative determination of anisotropic magnetoelectric coupling in BiFeO3–CoFe2O4 nanostructures. *Appl. Phys. Lett.* **97,** 052902 (2010).

206. Teyssèdre, G. & Lacabanne, C. Study of the thermal and dielectric behavior of P(VDF-TrFE) copolymers in relation with their electroactive properties. *Ferroelectrics* **171,** 125-144 (1995).

Appendix

A1: Nanoimprint of P(VDF-TrFE) on Different Surfaces

Since we aim to fabricate nanoimprinted devices, imprinting P(VDF-TrFE) of good quality on a large scale is needed. In general, the nanoimprint quality mainly depends on the following issues: the confinement of the imprint; the configuration and the geometry of the mold; the adhesion between P(VDF-TrFE) and the mold; the adhesion between P(VDF-TrFE) and the underlying substrate surface. Here, we discuss all these issues and try to figure out the best imprinting conditions which we can use in the device fabrication process.

A1.1 The confinement of the imprint

The imprint confinement is categorized in three types as specified in Figure A1.1: the complete confinement, the limiting state, and the partial confinement. When the to-be-imprinted film is thick enough, the mold cannot penetrate through the entire film and reach the substrate surface; in this case, there is a continuous residual layer remaining on the substrate, leading to partial confinement. When the film thickness decreases to a critical value t_c, the mold can make direct contact with the substrate through the film and there is no residual layer left, while the soft material can still fully fill the mold cavities; this situation leads to the limiting state of the imprinting. Further decreasing the film thickness results in the partial filling of the mold cavities, leading to the complete confinement of the imprint.

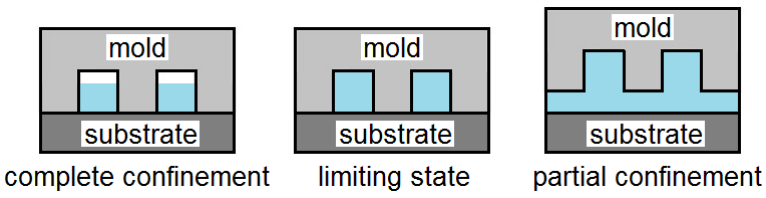

Figure A1.1: Scheme of different cases of imprinting confinement

It can be seen that, in the case of the limiting state, we obtain a relatively large contact area between the mold and the imprinted film ($\boldsymbol{A_{mold}}$) but the smallest contact area between the substrate and the imprinted film ($\boldsymbol{A_{sub}}$) among all three imprinting cases. Clearly, the complete confinement or the limiting state of Figure A1.1 are more demanding with respect to the adhesion of P(VDF-TrFE) onto the substrate than the case of partial confinement, due to the differences of surface of contact between polymer and substrate. In practice, device fabrication requires the limiting state or the complete confinement. Therefore, we need to make sure that the adhesion of the mold/P(VDF-TrFE) interface should be much smaller than that of the substrate/film interface.

A1.2 The configuration and the geometry of the mold

In this thesis, three mold configurations are employed as drawn in Figure A1.2: a mold with square holes (H), a mold with lines (L), and a mold with pillars (P). Five molds with these three configurations are used. The designed geometrical parameters of these five molds including the width $\boldsymbol{w}$ or the diameter $\boldsymbol{d}$, the pitch $\boldsymbol{p}$, and the height $\boldsymbol{h}$ of the nano-features are listed in Table A1.1. The molds are named as follows: taking H280 as an example, 'H' stands for the configuration of the mold (square holes) and '280' stands for the pitch of the nano-features.

The configuration and the geometry of the mold determine the contact areas of two interfaces, the mold/P(VDF-TrFE) interface and the substrate/P(VDF-TrFE) interface. This information together with the ratio of two contact areas are calculated and summarized in Table A1.2. As we can see, the mold H280 and the mold L180 have the smallest and similar $\boldsymbol{A_{sub}/A_{mold}}$ ratios compared to other molds in the case of the limiting imprint state. This means that imprinting with these two molds is more difficult compared to the others. Therefore, we choose these two molds for the imprinting tests in this chapter and we assume that, when the imprinting quality is acceptable with these two molds, the other molds can work well to obtain good imprinting nano-structures of P(VDF-TrFE).

In addition, the theoretical values of the critical film thickness t_c of P(VDF-TrFE) for different molds can also be calculated according to the configuration and the geometry of the mold. Taking mold H280 as an example, the volume of the material before the imprinting should be equivalent to that after the imprinting within in a unit cell of the mold, giving the equation $t_c \times p \times p = w \times w \times h$, resulting in t_c = (200 x 200 x 200)/(280 x 280) nm= 102 nm. The critical values for different molds are listed in Table A1.1 and provide a reference in order to make imprinting in the limiting state or in the complete confinement in the previous chapters.

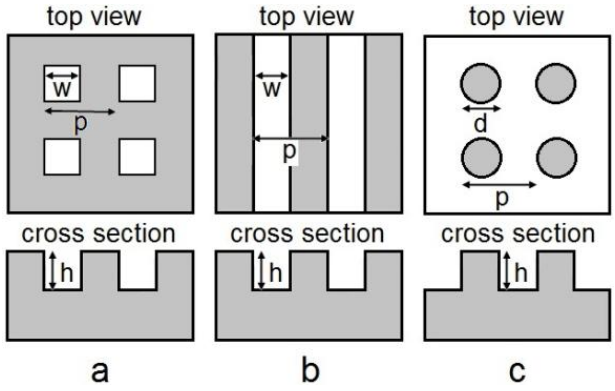

Figure A1.2: Geometrical scheme of different mold configurations

Table A1.1: Summary of geometrical parameters for different molds and the critical film thickness (t_c) in the case of the limiting imprint state.

	w or d (nm)	p (nm)	h (nm)	t_c (nm)
H280 (holes)	200	280	200	102
L180 (lines)	115	180	200	128
L400 (lines)	200	280	200	100
P190 (pillars)	65	190	100	91
P500 (pillars)	150	500	100	93

Table A1.2: Summary of the contact area between imprinted P(VDF-TrFE) and the bottom substrate (A_{sub}), the contact area between imprinted P(VDF-TrFE) and the top mold (A_{mold}), and the A_{sub}/A_{mold} ratio for different mold configurations, all in the limiting imprinting state.

	A_{sub} (nm^2)	A_{mold} (nm^2)	A_{sub}/A_{mold}
H280	200^2	$5x200^2$	0.20
L180	115 x Length	(200+200+115) x Length	0.22
L400	200 x Length	(200+200+200) x Length	0.33
P190	190^2-Π x 32.5^2	190^2 - Π x 32.5^2 +Π x 65 x 100	0.62
P500	500^2- Π x 75^2	500^2 - Π x 75^2 + Π x 150 x 100	0.83

A1.3 The adhesion between P(VDF-TrFE) and the mold

In order to remove the mold after the imprinting without P(VDF-TrFE) sticking on it, the adhesion between P(VDF-TrFE) and the mold should be minimized. Therefore, the mold was immersed into a (Heptadecafluoro-1,1,2,2-tetrahydrodecyl)dimethylchlorosilane toluene solution (in a glove box) in order to form an anti-adhesion mono-layer and to reduce its surface energy and the adhesion between P(VDF-TrFE) and the mold.

A1.4 The adhesion between P(VDF-TrFE) and the underlying substrate surface

The adhesion between P(VDF-TrFE) and the underlying substrate surface should be large enough in order to make sure that nanoimprinted P(VDF-TrFE) is not torn off upon demolding. In this thesis, four substrates (PTAA, gold (Au), SiO_2, and silver (Ag)) on which P(VDF-TrFE) is imprinted are used: (1) imprinting P(VDF-TrFE) on a PTAA layer to fabricate nanoimprinted traditional FeFETs; (2) imprinting P(VDF-TrFE) on a Au/SiO_2 substrate to fabricate nanoimprinted hybrid FeFETs; and (3) imprinting P(VDF-TrFE) on a Ag substrate to fabricate multiferroic systems. As mentioned above, the imprinting quality of P(VDF-TrFE) on these substrates is tested with either mold H280 or L180 to make sure that we can obtain good imprinted nano-structures even with the hard molds. In practice, the critical thickness $\boldsymbol{t_c}$, with which the limiting imprinting state is reached, is 95-100 nm for mold H280 and 125-130 nm for mold L180. The imprinting quality was checked by AFM in tapping mode.

A1.4.1 Imprinting on a PTAA layer

Figure A1.3 shows AFM topographic images of imprinted P(VDF-TrFE) on a continuous PTAA layer in the case of the complete

confinement, the limiting state, and the partial confinement. Good nano-structures with minor defects were obtained for all cases, indicating sufficient adhesion between P(VDF-TrFE) and PTAA. This is most probably because a very thin inter-mixed layer of P(VDF-TrFE) and PTAA was formed when spin-coating the P(VDF-TrFE) solution on the PTAA layer, which enhances the adhesion.

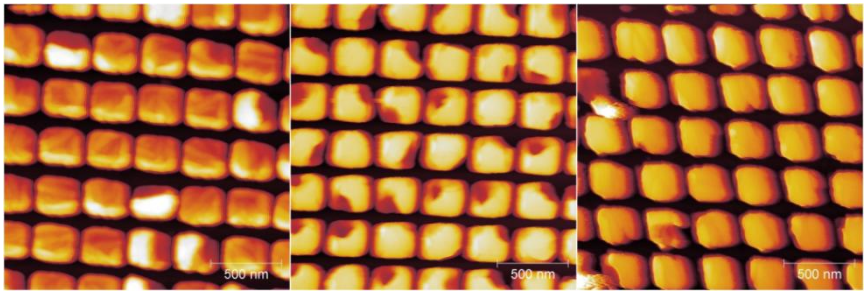

Figure A1.3: AFM topographic images (tapping mode) of, Left image: a P(VDF-TrFE) layer of 85 nm initial thickness imprinted in complete confinement over a 45 nm PTAA layer; Middle image: a P(VDF-TrFE) layer of 95 nm initial thickness imprinted in the limiting state over a 45 nm PTAA layer; Right image: a P(VDF-TrFE) layer of 105 nm initial thickness imprinted in partial confinement over a 45 nm PTAA layer. A standard grade of P(VDF-TrFE) was used in this case.

A1.4.2 Imprinting on gold

Gold is a noble and inert metal and no polar bond could be easily formed at the surface in ambient conditions, resulting in poor adhesion between Au and P(VDF-TrFE). Therefore, we directly used a special grade of P(VDF-TrFE) modified by carboxylic acid moieties along the polymer backbone. This grade is in general expected to have improved adhesion on wide range of substrates.

The imprinting result of this modified P(VDF-TrFE) on gold is shown in Figure A1.4. In general, lots of defects were obtain in both complete confinement and partial confinement. We can count that there are 35 defects out of 225 nano dots (15.6% defects) in the case

of partial confinement, and 103 defects out of 225 nano dots (45% defects) in the case of complete confinement. This reflects the weak adhesion of the polymer onto the gold surface. Similar results were actually obtained with a standard grade of P(VDF-TrFE), illustrating that no improvement of adhesion results from the introduction of carboxylic acid groups in the polymer. This is logical, since the surface of a noble, inert metal such as gold is not expected to engage into specific interactions with carboxylic acids.

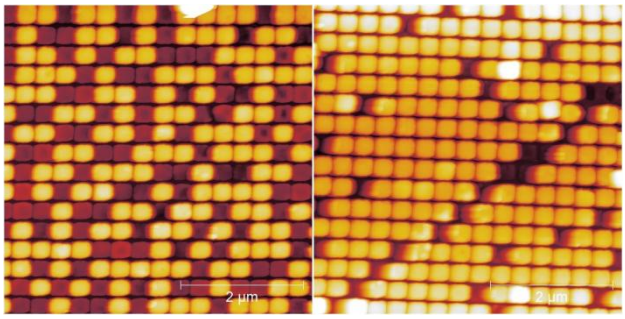

Figure A1.4: AFM topographic images (tapping mode) of, Left image: a P(VDF-TrFE) layer of 85 nm initial thickness imprinted in complete confinement over Au; Right image: a P(VDF-TrFE) layer of 110 nm initial thickness imprinted in partial confinement over Au. A modified grade of P(VDF-TrFE) was used in this case.

To improve the adhesion of modified P(VDF-TrFE) on gold, we modified the gold surface by 11-mercaptoundecanoic acid. Indeed, H-bonding between the carboxylic acid groups of P(VDF-TrFE) and the carboxylic acid-ended thiol should increase adhesion. The imprinting result is shown in Figure A1.5. There are 72 defects out of 225 nano dots (32% defects) in the case of partial confinement, and 78 defects out of 225 nano dots (35% defects) in the case of complete confinement. The percentage of the defects is similar in the case of partial confinement or of complete confinement; in addition, the proportion of defects is slightly decreased compared to the previous case. Therefore, the adhesion can be slightly improved by modifying

the gold surface with 11-mercaptoundecanoic acid, although significant defects were still obtained.

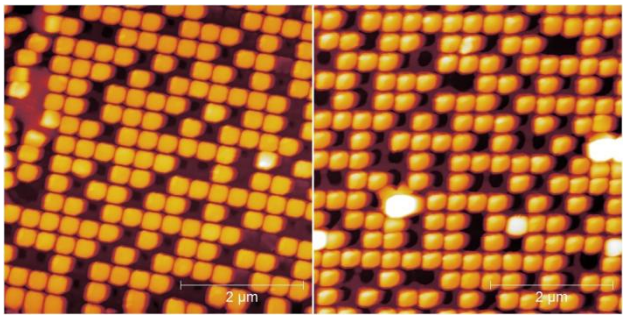

Figure A1.5: AFM topographic images (tapping mode) of, Left image: a P(VDF-TrFE) layer of 95 nm initial thickness imprinted in the limiting state over Au modified by 11-mercaptoundecanoic acid; Right image: a P(VDF-TrFE) layer of 120 nm initial thickness imprinted in partial confinement over Au modified by 11-mercaptoundecanoic acid. A modified grade of P(VDF-TrFE) was used in this case.

A1.4.3 Imprinting on SiO_2

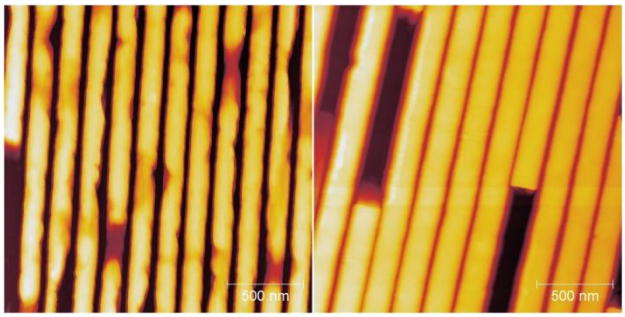

Figure A1.6: AFM topographic images (tapping mode) of, Left image: a P(VDF-TrFE) layer of 105 nm initial thickness imprinted in the complete confinement over SiO_2; Right image: a P(VDF-TrFE) layer of 105 nm initial thickness imprinted in complete confinement on SiO_2 modified by 3-aminopropyldimethylethoxysilane. A standard grade of P(VDF-TrFE) was used in this case.

Mold L180 was used in this case and imprinting was performed in the case of complete confinement. As shown in the left image of Figure 3-6, well-defined line patterns with only approximately 1 line defect were obtained. Then we checked the imprinted quality on SiO_2 modified by amino-groups with similar results obtained compared to the case of the unmodified SiO_2 surface, as shown in the right image of Figure A1.6. This indicates that the adhesion is sufficient between P(VDF-TrFE) and SiO_2 due to the presence of the hydroxyl groups on the surface. Amino-groups play similar roles when the modified SiO_2 substrate was used.

A1.4.3 Imprinting on silver

Because the surface of silver is oxidized, a stronger adhesion with P(VDF-TrFE) is to be expected. The imprinting result of P(VDF-TrFE) on silver is shown in Figure A1.7. There is only 1 defect out of 225 nano dots (0.4% defects) in the case of partial confinement, but 41 defects (18% defects) in the case of complete confinement. Although the proportion of defects in complete confinement is still larger than in partial confinement, the overall adhesion of P(VDF-TrFE) on silver is clearly much better than on gold, modified or not with 11-mercaptoundecanoic acid.

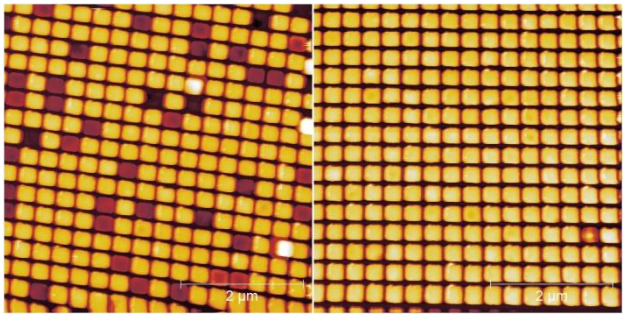

Figure A1.7: AFM topographic images (tapping mode) of, Left image: a P(VDF-TrFE) layer of 95 nm initial thickness imprinted in the limiting state over Ag; Right image: a P(VDF-TrFE) layer of 120 nm initial thickness imprinted in partial confinement over Ag. A standard grade of P(VDF-TrFE) was used in this case.

To check whether we can future improve the adhesion, the P(VDF-TrFE) grade containing by carboxylic acid moieties along the polymer backbone was tested. As shown in Figure A1.8, there is only 1 defect out of 225 nano dots (0.4% defects) in the case of partial confinement, and 11 defects (5% defects) in the case of complete confinement. Therefore, in the case of complete confinement, the chemically-modified P(VDF-TrFE) has a better adhesion on silver (5% defects) than the standard grade of P(VDF-TrFE) (18% defects), confirming the interest of the chemical modification.

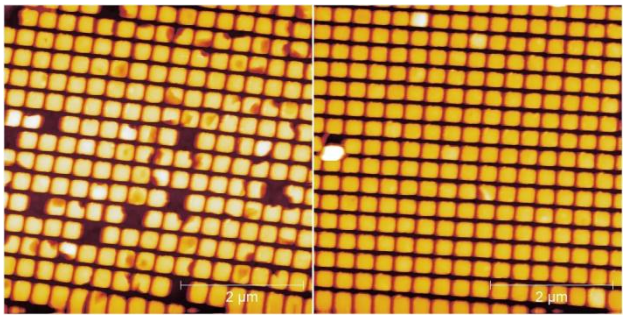

Figure A1.8: AFM topographic images (tapping mode) of, Left image: a P(VDF-TrFE) layer of 95 nm initial thickness imprinted in the limiting state over Ag; Right image: a P(VDF-TrFE) layer of 120 nm initial thickness imprinted in partial confinement over Ag. A modified grade of P(VDF-TrFE) was used in this case.

A1.5 Summary

In summary, an adhesion problem remains between P(VDF-TrFE) and gold in the case of complete confinement, independent of whether or not the gold surface is treated with 11-mercaptoundecanoic acid (even though the thiol treatment decreases slightly the issue). This hints to the fact that the adhesion between P(VDF-TrFE) and gold is not much larger than that between P(VDF-TrFE) and the fluorinated mold; this conclusion holds true for the modified P(VDF-TrFE) grade. Therefore, the silanization of the mold is extremely critical when using gold as substrate, and we have to make sure that no defect in the

perfluorosilane coating of the mold remains, to be able to imprint the P(VDF-TrFE) in the complete confinement. However, this adhesion issue is somehow helpful in some cases, since we need large openings on the part of Au electrodes for conduction in nanoimprinted hybrid FeFETs, which was discussed in Chapter 5, and this adhesion issue ensures that Au electrodes have a direct contact with the semiconducting PTAA.

In the case of using a PTAA polymer layer as substrate, the adhesion is sufficient with minor defects, most probably due to the formation of an inter-mixied layer of P(VDF-TrFE) and PTAA.

In the case of using SiO_2 as a substrate, the adhesion is also sufficient with acceptable defects, because the hydroxyl groups on the unmodified surface and the amino-groups on the modified surface increase the interaction between the substrate and P(VDF-TrFE).

In the case of using silver as substrate, due to the presence of a native oxide layer, the adhesion between the silver and P(VDF-TrFE) is also improved, with as a result a smaller amount of defects. Moreover, the carboxylic acid-modified P(VDF-TrFE) further improves the adhesion with a very small content in defects obtained, even in the case of complete confinement. Therefore, metals that bear a native layer of oxide like silver are of great interest for direct imprinting on their surfaces due to the strong bonding between the oxide and P(VDF-TrFE).

Appendix

A2: Piezoresponse Force Microscopy Investigation on Polymer Ferroelectrics: Choice of Probes and Experimental Conditions

As presented in Chapter 2 (Section 2.4), PFM has been proven to be a powerful equipment to study the local ferroelectric properties of ferroelectric polymers like P(VDF-TrFE). However, PFM is an extremely sensitive equipment, the output of which can be altered by many parameters. In this appendix, except for the parameters described in Chapter 2, we try to explore the influence of some other parameters such as the nature of the tip, the selection of the PFM operation mode, and the use of different bottom electrodes. Then we try to find optimized PFM conditions for characterizing the ferroelectric properties of P(VDF-TrFE).

A2.1 Experimental

Sample preparation. Interdigitated electrodes (2 μm width, separated by 2 μm spacing) were defined by standard photolithography on a Si/SiO_2(200nm) substrate, followed by the deposition of 5/25 nm Cr/Au and metal lift-off (Figure A2.1 (a)). On this substrate, *ca.* 340 nm of P(VDF-TrFE) was spin-coated (2000 rpm, 500 rpm/s, 1 min) from a 65 g/L P(VDF-TrFE)/acetylacetone solution. The resulting samples were annealed at 135 ℃ for 10 min in air. A cross section of the final sample is shown in Figure A2.1 (b). In the following, all the experiments are performed on this sample, except mentioned otherwise.

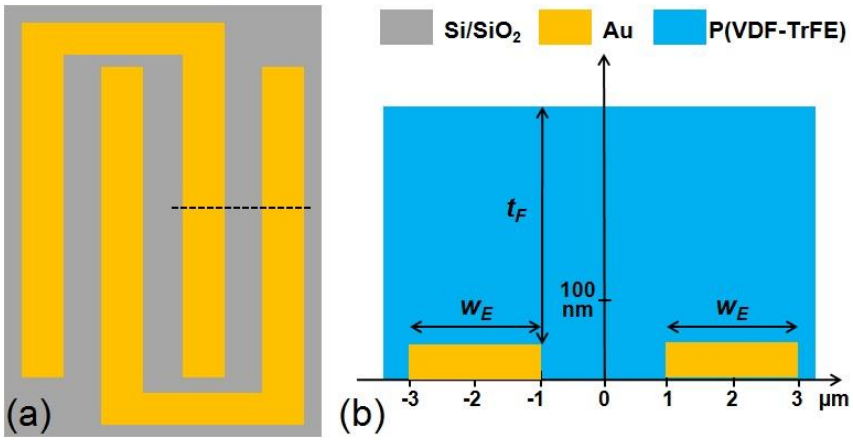

Figure A2.1: Schematic drawing of the sample structure. (a) Top view of the electrode substrate. (b) Cross section of the final sample along the dashed line in panel (a).

Sample characterization. A PFM equipment (Bruker Icon Dimension) was used to characterize the ferroelectric behavior of P(VDF-TrFE) in contact mode. Both PFM imaging mode and spectroscopy mode were employed for the characterization. Five types of conductive probes were used to investigate the influence of the probe parameters on the PFM results. The characteristic parameters of these tips are listed in Table A2.1. The spring constant *k* was calibrated using the thermal noise method (The photodectetor sensitivity was calibrated on a rigid Si substrate) and the contact resonance frequency was calibrated on the above mentioned P(VDF-TrFE) sample, both with the PFM equipment. All the other parameters were provided by the probe providers. During the PFM experiment, the contact force between the probe and the sample was controlled to be small (*ca.* 50 nN), in order to avoid the P(VDF-TrFE) layer being mechanically damaged by the probe. The PFM worked at (close to) the contact resonance frequency for all the probes, unless stated otherwise.

Table A2.1: Characteristic parameters of different probes.

	Spring constant k (N/m)	Tip radius r (nm)	Conductive coating	Contact resonance frequency (kHz)
SCM-PIC (Bruker)	0.22	20	PtIr	11-14
SCM-PIT (Bruker)	3.22	20	PtIr	310-330
MESP-LM (Bruker)	2.81	25	CoCr	370-400
MESP-HM (Bruker)	3.07	80	CoCr	300-320
CDT-CONTR (Nanosensors)	0.31	150	Conductive diamond	80-100

A2.2 Results and discussion

The PFM imaging mode was firstly used to check the ferroelectric response of P(VDF-TrFE) using different probes. As typically shown in Fig. A2.2 (a, b), when working at contact resonance frequencies, a clear contrast is observed in all PFM amplitude images on the regions above Au electrodes within the poled regions (red-boxed), irrespective of the type of the used probe. However, when working at low

frequencies (*e.g.*, 15 kHz), PFM images with acceptable contrast can only be obtained by using SCM-PIT probes. This indicates that working at the contact resonance enhances the piezoresponse signal (as described in Section 2.4.2 of Chapter 2) which can be well detected using all the tested conductive probes, irrespective of their different characteristics detailed in Table A2.1. However, the piezoreponse signal is very weak when working at low frequencies, which requires using a high quality probe to detect this signal. Apparently, the SCM-PIT probe is a good choice for working at low frequencies, since it leads to a clear contrast in PFM amplitude images as shown in Fig. A2.2 (c).

As also described in Chapter 3, with these PFM amplitude images, the coercive field E_c of P(VDF-TrFE) can be calculated according to the geometrical parameters shown in Fig. A2.2 (d) together with the poling conditions:

$$E_c = \frac{V}{t_{F'}} = \frac{V}{\sqrt{w^2 + t_F^2}} \ , \qquad \text{(Equation A2.1)}$$

$$w = (w_P - w_E)/2 \ , \qquad \text{(Equation A2.2)}$$

where V is the poling voltage (30 V), t_F is the P(VDF-TrFE) layer thickness (340 nm), w_E is the width of the electrode (2 μm), and w_P is the width of the poled region (shown as AB in Fig. A2.2 (a)) which can be measured from the images. The calculated E_c in the case of using different probes is shown in Fig. A2.2 (e), the value of which has very small variations. The average value is *ca.* 67 MV/m, which is typical for P(VDF-TrFE) thin films and comparable to the results reported in the literature as indicated in Chapter 3.

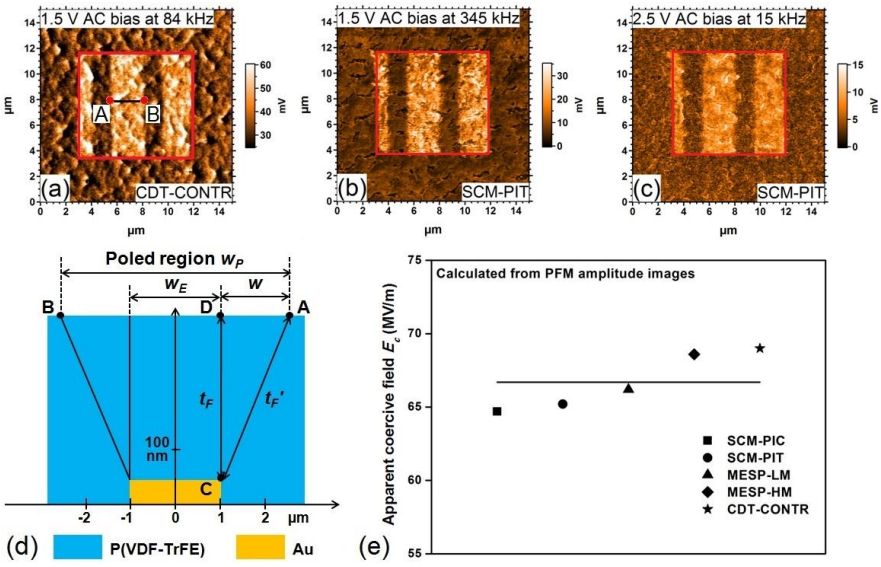

Figure A2.2: PFM amplitude images obtained with different probes (a) CDT-CONTR probe at contact resonance frequency; (b) SCM-PIT probe at contact resonance frequency; (c) SCM-PIT probe at low frequency; (d) Cross section of the sample along the solid line AB in panel (a). (e) Calculated coercive field E_c using Equations A2.1 and A2.2 for different probes according to the PFM amplitude images and the geometrical configuration of the sample. The solid line in panel (e) presents the averaged E_c.

Then the PFM spectroscopy mode was used to obtain the ferroelectric hysteresis loops of P(VDF-TrFE) in the same sample using different probes, which gave more surprising results. As shown in Fig. A2.3 (a, b), the PFM hysteresis loops have completely different widths with different probes, indicating that the measured apparent coercive field E_c (the half width of the loop divided by the film thickness) of P(VDF-TrFE) appears to be different, which is not true since the same P(VDF-TrFE) film is used in all cases. Therefore, this difference in the measured apparent E_c's must result from the fact that different probes have different characteristics as, *e.g.*, their conductive coating, their spring constant k and their tip radius r, as summarized in Table A2.1. The apparent E_c versus k and E_c versus r graphs are shown in Fig. A2.3 (b) and (c), respectively, where the averaged E_c value

calculated from the PFM amplitude images is also added (red dashed lines) as reference. These two graphs show that using probes with moderate spring constants and small tip radiuses, *e.g.* SCM-PIT with k = 3.22 N/m and r = 20 nm, results in larger apparent coercive field values of *ca.* 25 MV/m. However, these larger values are still far away from the reference 67 MV/m which is closer to the true E_c of P(VDF-TrFE) as mentioned above.

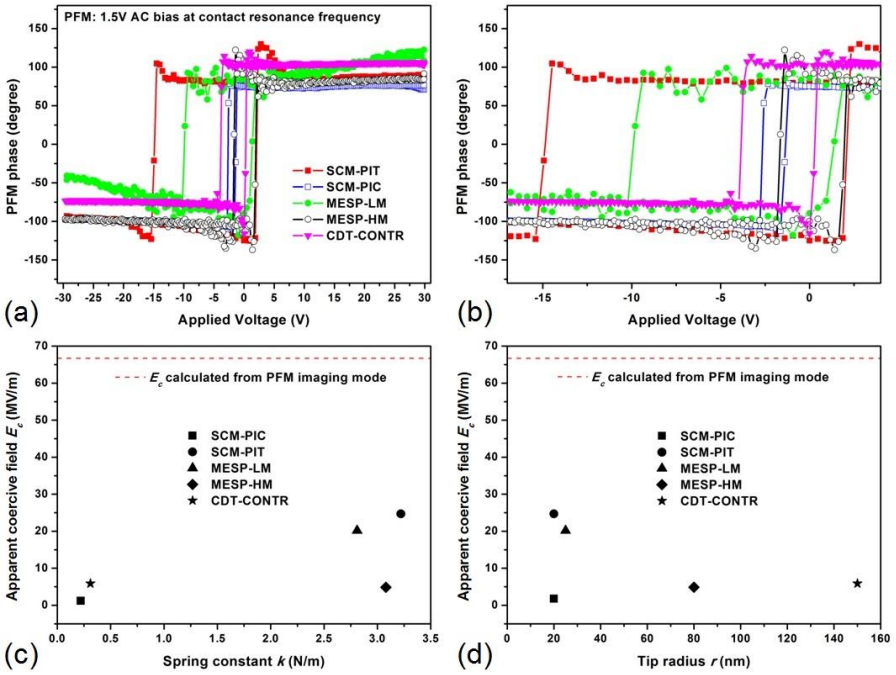

Figure A2.3: PFM phase graphs (a) (b) and calculated coercive field E_c for different probes (c) (d) according to the width of the phase hysteresis loops. Panel (b) is the enlarged graph of panel (a) (-17 V to 4 V applied voltage range). Panel (c) and (d) illustrate E_c versus the spring constant k and E_c versus the tip radius r of the probes, where the averaged E_c value obtained from the PFM imaging mode is also added (red dashed lines) as reference.

The reasons why the apparent E_c extracted from the hysteresis loops differs dramatically from the one extracted from the PFM image might due to the electrostatic coupling present during the experiment, because the piezoresponse signal was recorded with the poling field

on in the spectroscopy mode, but off in the imaging mode. To check this point, the so-called switching field spectroscopy was performed on a sample of *ca.* 100 nm P(VDF-TrFE) spin-coated over an Ag substrate. With the switching field spectroscopy, the piezoresponse signal, *i.e.*, phase, is recorded when the dc field is switched off, resulting in a minimized electrostatic coupling. The PFM amplitude and phase curves obtained by this method are presented in Fig. A2.4, in which clear butterfly-shaped amplitude curves and phase hysteresis loops are observed. Due to the minimization of the electrostatic coupling, the maximum amplitude value is smaller and the width of the hysteresis loop is wider compared to ones obtained with the poling field on. This proves that the poling field does result in considerably large electrostatic coupling and has a significant influence on the acquisition of the piezoresponse signal. In addition, the apparent coercive field obtained on this sample according to the phase hysteresis loops ranges from *ca.* 40 to 60 MV/m, which is larger than the ones on the sample using Au as electrode. This is probably due to the presence of a thin oxidation layer on Ag, which shares the poling voltage with the P(VDF-TrFE) layer. However, the exact reason why PFM imaging mode and spectroscopy mode give different results remains unclear.

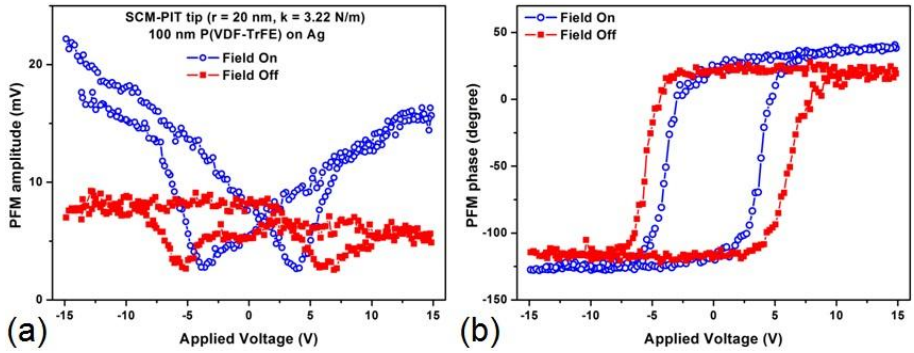

Figure A2.4: PFM amplitude (a) and phase (b) graphs obtained with the electrical field on or off at the contact resonance frequency and 2.5 V ac bias using a SCM-PIT probe. In this case, a *ca.* 100 nm P(VDF-TrFE) layer deposited over an Ag substrate was used.

Another parameter that might have influence on the PFM spectroscopy mode is the PFM working frequency, which is shown in Fig. A2.5. The width of the hysteresis loop obtained at a low frequency is wider than that at the contact resonance frequency. This indicates that working at contact resonance probably adds another source to the electrostatic coupling which can influence the piezoresponse signal acquisition; alternatively, this might be due to the effect of frequency on ferroelectric hysteresis.

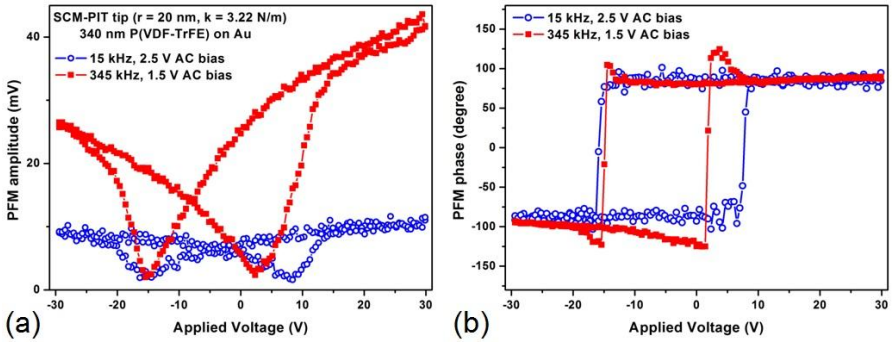

Figure A2.5: PFM amplitude (a) and phase (b) graphs obtained at the contact resonance frequency and at a low frequency using a SCM-PIT probe.

Finally, one should also be aware that the static electric field in the film is not homogeneous, and varies abruptly when going away from the tip. This effect was simulated in Fig. 6.6 of Chapter 6, where it can be seen that the field is much stronger close to the tip; hence, the average coercive field computed by dividing the switching voltage by the film thickness provides a very rough image of the real coercive field. In contrast, when the tip is scanned over a region to pole the film, a given point of the film experiences a wide range of poling fields depending on the moving tip position, which leads to a proper averaging of the field as judged by the much more accurate of coercive field obtained subsequently.

A2.3 Summary

Summing up, we tested several parameters which can influence the practical PFM operation and data acquisition. It seems that the PFM imaging mode is a more stable and compatible operation mode compared to the spectroscopy mode. Therefore, this mode is employed in most parts of the work (Chapters 3-5) in this thesis to study the ferroelectric properties of P(VDF-TrFE). In the case of using the spectroscopy mode, SCM-PIT probes with Pt/Ir conductive coating, a moderate spring constant (3.22 N/m), and a small tip radius (20 nm) seem the best choice among all the tested probes. Therefore, this type of probes is used to take PFM phase hysteresis loops and amplitude curves in Chapter 6. In addition, the spectroscopy mode with the poling field on is used due to the fast data acquisition and the easy-to-see experiment results which are preferred considering the characterization conditions of multiferroic samples. The problem of the electrostatic coupling induced by the poling field in this case could be neglected since all the experiments are performed and all the results are analyzed based on the same PFM conditions; one should however be aware that the values of field obtained are relative, and can only be compared provided the same conditions of acquisition are used (which is indeed the case in Chapter 6).

Appendix

A3: Filling the Openings Between Nanoimprinted P(VDF-TrFE) Nanowires

As has been shown in this thesis, nanoimprinted P(VDF-TrFE) has a great potential for organic memory and multiferroism applications. However, insulating the openings between nanoimprinted P(VDF-TrFE), *i.e.*, the trenches between nanowires, is still a remaining technological issue and is essential for obtaining fully functional electronic devices. Therefore, in this appendix, we try to explore a way to fill the openings between P(VDF-TrFE) nanowires by another insulating polymer. The strategy used for this purpose is schematically described in Fig. A3.1.

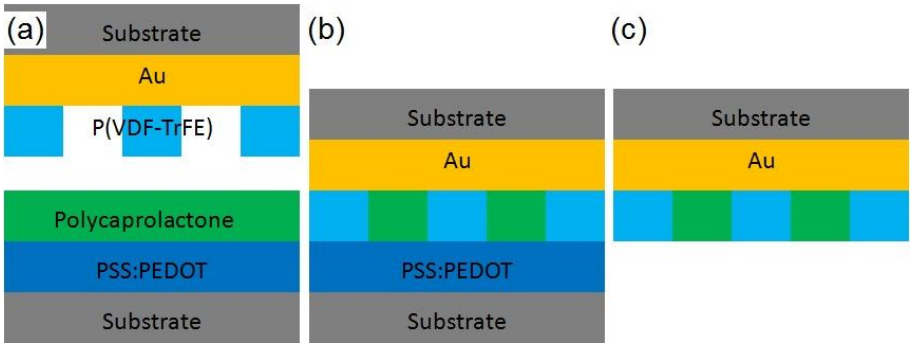

Figure A3.1: Schematic description of the strategy of filling the openings between nanoimprinted P(VDF-TrFE) nanowires by polycaprolactone.

First, the P(VDF-TrFE) nanowires were produced by NIL from a *ca.* 95 nm thick film over a Au substrate, using mold L400 (135 ℃, 60 bar, 10 min). The resulting P(VDF-TrFE) nanowires are of *ca.* 200 nm width and height, and *ca.* 200 nm spacing. An AFM height image and a height profile of this imprinted sample are shown in Fig. A3.2 (a, c) indicating that well defined P(VDF-TrFE) nanowires are obtained. Of course, imprinting defects can be seen (not shown here) at larger

scales due to the adhesion problem between Au and P(VDF-TrFE) which has been discussed in Appendix A1. However, these defects do not influence significantly the filling of the openings.

Then this imprinted sample with P(VDF-TrFE) nanowires was used as a second mold to perform NIL (75 ℃, 60 bar, 5 min) on a polycaprolactone (*ca.* 100 nm thick) layer deposited on a *ca.* 80 nm thick PSS:PEDOT layer (Fig. A3.1 (b)). This step was performed to push the insulating polycaprolactone polymer into the trenches between P(VDF-TrFE) nanowires. At this stage, polycaprolactone (PCL) was used because it has a low melting point (*ca.* 65 ℃) which is well below the Curie temperature of P(VDF-TrFE) (*ca.* 94.5 ℃). In this case, NIL could be done at a properly low temperature (75 ℃) between the melting point of polycaprolactone and the Curie point of P(VDF-TrFE), while P(VDF-TrFE) is still in its ferroelectric phase and keeps rigid, and polycaprolactone is softened for mold penetration. The thickness of polycaprolactone was selected as *ca.* 100 nm to make sure NIL is performed in complete confinement, in which case there is no residual layer of polycaprolactone left on top of P(VDF-TrFE) nanowires, at least ideally.

After that, the sample was kept in water for one night in order to dissolve the PSS:PEDOT sacrificial layer and release the sample with alternating P(VDF-TrFE)/polycaprolactone nanowires on the Au electrode. This final sample was annealed at 75 ℃ on a hot plate in order to have a better organization of polycaprolactone in the trenches (Fig. A3.1 (c)). An AFM height image and a height profile of this final sample are shown in Fig. A3.2 (b, d). It is clear that the trenches were properly filled by polycaprolactone and that the polycaprolactone is on average 10-20 nm lower than the P(VDF-TrFE). The sample was also tested by ToF-SIMS and the signal of F element only present in P(VDF-TrFE) appeared clearly, indicating that the remaining polycaprolactone layer over P(VDF-TrFE) is very thin, if there is any.

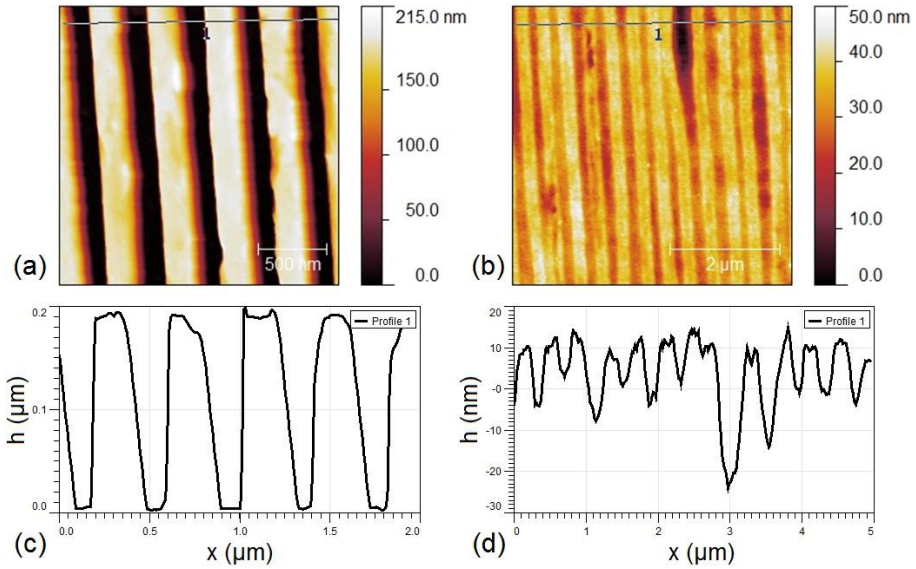

Figure A3.2: AFM height images of (a) nanoimprinted P(VDF-TrFE) sample and (b) same sample in (a) filled by polycaprolactone. (c) and (d) are height profiles of samples in (a) and (b) along the lines presented in the height images.

Then, the local ferroelectric property of P(VDF-TrFE) nanowires in this hybrid sample consisting of alternating P(VDF-TrFE)/polycaprolactone nanowires was checked by PFM using a diamond coated conductive probe (CDT-CONTR from Nanosensors). As shown in Fig. A3.3, clear PFM phase hysteresis loops and butterfly-shaped amplitude curves are observed, indicating that P(VDF-TrFE) still remains ferroelectric. This also confirms again that there is minor polycaprolactone remaining atop the P(VDF-TrFE) nanowires; otherwise, it would prevent the ferroelectric switching of P(VDF-TrFE).

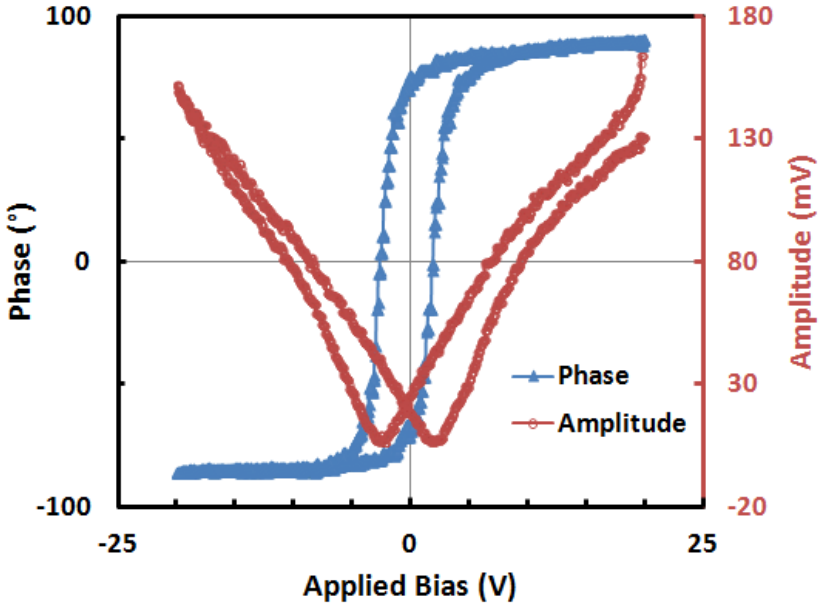

Figure A3.3: PFM phase and amplitude as a function of the applied bias on a nanoimprinted P(VDF-TrFE) nanowire in the hybrid PCL-filled sample. A clear PFM phase hysteresis loop and a butterfly-shaped amplitude curve are obtained.

Recently, another similar strategy, called solution micromolding, was reported (Phys. Status Solidi A 212, 2124-2132 (2015)), where an imprinted sample consisting of P(VDF-TrFE) stripes was used as the mold and the imprinting was performed on an insulating polymer solution. With this strategy, the imprint could be done at room temperature and there were no limitations related to the melting point of the polymer. Therefore, it could also be a possible route to fill the openings of nanoimprinted P(VDF-TrFE). However, this strategy was demonstrated at the micrometer scale, and further investigations are needed to do it at the nanometer scale.

Nevertheless, we have demonstrated a strategy to insulate nanoimprinted P(VDF-TrFE) openings. This was done by NIL, in which another insulating polymer (polycaprolactone) was pushed to fill these openings. This finally resulted in a nice sample consisting of

alternating P(VDF-TrFE)/polycaprolactone nanowires. The next step would be to evaporate a top electrode on this sample and characterize the macroscopic ferroelectric properties of P(VDF-TrFE) nanowires in this hybrid sample.